

Universidade de São Paulo
Instituto de Física

Estudos Sobre Transições de Fase e Condensação de Bose-Einstein de Magnons em Compostos Orgânicos de Ni, Mn e Fe

Henrique Fabrelli Ferreira

Orientador: Prof. Dr. Rafael Sá de Freitas

Co-orientador: Prof. Dr. Armando Paduan Filho

Tese de doutorado apresentada ao Instituto de Física
como requisito parcial para a obtenção do título de
Doutor em Ciências.

Banca examinadora:

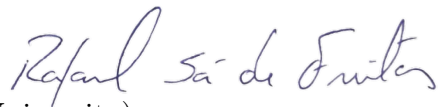
Prof. Dr. Rafael Sá de Freitas - Orientador (IFUSP)

Prof^a. Dr^a. Raquel de Almeida Ribeiro (Iowa State University)

Prof. Dr. Mucio Amado Continentino (CBPF)

Prof. Dr. José Abel Hoyos Neto (IFSC-USP)

Prof. Dr. Gabriel Teixeira Landi (IFUSP)



São Paulo
2020

FICHA CATALOGRÁFICA
Preparada pelo Serviço de Biblioteca e Informação
do Instituto de Física da Universidade de São Paulo

Ferreira, Henrique Fabrelli

Estudos sobre transições de fase e condensação de Bose-Einstein de magnons em compostos orgânicos de Ni, Mn e Fe. São Paulo, 2021.

Tese (Doutorado) – Universidade de São Paulo, Instituto de Física, Depto. de Física dos Materiais e Mecânica.

Orientador: Prof. Dr. Rafael Sá de Freitas

Área de Concentração: Física

Unitermos: 1. Condensado de Bose-Einstein; 2. Magnetismo; 3. Calor específico.

USP/IF/SBI-012/2021

University of São Paulo
Physics Institute

Studies on Phase Transitions and Bose-Einstein Condensation of Magnons in Ni, Mn and Fe-Based Organic Compounds

Henrique Fabrelli Ferreira

Supervisor: Prof. Dr. Rafael Sá de Freitas
Co-supervisor: Prof. Dr. Armando Paduan Filho

Thesis submitted to the Physics Institute of the
University of São Paulo in partial fulfillment of the
requirements for the degree of Doctor of Science.

Examining Committee:

Prof. Dr. Rafael Sá de Freitas - Supervisor (IFUSP)
Prof. Dr. Raquel de Almeida Ribeiro (Iowa State University)
Prof. Dr. Mucio Amado Continentino (CBPF)
Prof. Dr. José Abel Hoyos Neto (IFSC-USP)
Prof. Dr. Gabriel Teixeira Landi (IFUSP)

São Paulo
2020

To mom (in memoriam)

Acknowledgements

The right thing to do here would be to thank to all people and events which directly or indirectly contributed to make this work possible. However, since I should be brief I will be pragmatic (and perhaps a bit unjust). So I will limit these acknowledgements to people who directly contributed to this work. To all other I would like to express my deepest gratitude.

First of all, I thank to my supervisor, Professor Rafael Sá de Freitas, and to my co-supervisor, Professor Armando Paduan Filho for risky endeavour of accepting to supervise me after I spent almost one year and a half in a different doctoral project from a different area. I am also grateful for all the support during this work and for the patience and resilience during the process of this doctorate, helping me to solve with enthusiasm the (many) problems that arose in this work. Against all odds, we did it! And I am proud of it. Thank you very much!

To my mother Leda S. Fabrelli (*in memoriam*) for all her love, comprehension and support during all my life and specially in the first years of my doctorate. I know that all her efforts was focused in realizing my wishes and dreams and I will be eternally grateful. My life now is also an extension of her life and I live for we both. Also, I thank to my relatives for all the love and support, in the good and in the hard times.

To my friends Rafael M. Ferro, André A. Burger, Elion D. Hack and Thiago L. C. Melo for shearing all the good and bad experiences from the academy, supporting each other. And also for the many funny lunch times we spent together.

For the collaboration and help with the theoretical part of this work I thank to Professor André P. Vieira for his valuable support.

This work would not be possible without the help of the X-ray techniques employed in the characterization of the samples. I thank to Professor Marcia C. A. Fantini, Tarsis M. Germano, Antônio Carlos F. Silveira for sharing and for helping with the facilities of the Laboratory of Crystallography. To Professor Marcia A. Rizzutto for the help with the X-ray fluorescence measurements.

To my colleagues Jonathan G. A. Ramón and Fabio S. A. Abud for all help and patience when I was learning to use our equipments and also for the valuable discussions.

For all operation and help with our cryostats and magnetic measurements and also for the friendship and teachings I thank to Luciano M. B. Santos.

To Alan A. Amorim, Paulo S. M. Silva and Marco A. Meira from the mechanical workshop for being available to make any kind of mechanical parts needed in this work.

To our secretary Rosana O. S. Silva for helping with all the bureaucracy and administrative stuffs.

Last but not least, I would like to acknowledge the Conselho Nacional de Desenvolvimento Científico e Tecnológico (CNPq) for the financial support to this work. Good citizens, pay your taxes!

“A smooth sea never made a skilled sailor”.

Swahili proverb

“As for me, I am tormented with an everlasting itch for things remote. I love to sail
forbidden seas, and land on barbarous coasts”.

Herman Melville, *Moby-Dick; or, the Whale*

Resumo

Neste trabalho nós exploramos o comportamento à baixas temperaturas dos compostos metalorgânicos $\text{NiCl}_2\text{-4SC(NH}_2)_2$ (DTN), $\text{MnCl}_2\text{-4SC(NH}_2)_2$ (DTM), $\text{FeCl}_2\text{-4SC(NH}_2)_2$ (DTF) e da versão dopada com Br do DTN, $\text{Ni(Cl}_{1-x}\text{Br}_x)_2\text{-4SC(NH}_2)_2$, através de medidas de magnetização, suscetibilidade magnética e calor específico. Para o DTN, nós estudamos a existência de um comportamento quase-1D subsequente a uma fase 3D ordenada e comparamos nossos resultados com simulações através do método de Monte-Carlo Quântico (QMC). Nós delimitamos a região correspondente ao comportamento quase-1D logo acima da porção do diagrama de fase correspondente à condensação de Bose-Einstein (CBE) de mágnons, detectando assim a reminiscência de um regime de líquido de Tomonaga-Luttinger, relacionado a cadeias magnéticas de DTN fracamente interagentes. Além disso nós extendemos nossos estudos para temperaturas mais altas, onde as correlações entre os spins se tornam desprezíveis. Isso nos permitiu verificar algumas discrepâncias no valor do parâmetro D da anisotropia de íon único. Em relação ao composto DTM, nossas medidas de calor específico mostraram a existência de duas transições de fase antiferromagnéticas para temperaturas tão baixas quanto 60 mK e campos magnéticos de até 1.4 T e nós discutimos hipóteses para tal fenômeno. Para o DTF, nossos resultados não mostram a existência de um ordenamento magnético para temperaturas tão baixas quanto 100 mK, o que faz desse composto um candidato para frustração magnética. Nós também sintetizamos amostras de DTN dopadas com Br com diferentes concentrações de dopante e realizamos medidas de suscetibilidade magnética, construindo o diagrama de fase em função da temperatura e campos magnéticos críticos com a porcentagem do dopante Br nas amostras. A partir desses resultados nós estudamos a influência da concentração de Br nas amostras. Finalmente nós apresentamos resultados preliminares acerca da influência da pressão em medidas magnéticas no DTN. A partir dos nossos resultados experimentais, combinados com teoria de campo médio, nós estimamos a pressão crítica p_c necessária para fechar o gap de energia e, conseqüentemente, promover uma transição de fase induzida por pressão.

Palavras-Chave: Condensação de Bose-Einstein, DTN, antiferromagnetismo.

Abstract

In this work we explored the low temperature physics of the metal-organic compounds $\text{NiCl}_2\text{-4SC(NH}_2)_2$ (DTN), $\text{MnCl}_2\text{-4SC(NH}_2)_2$ (DTM), $\text{FeCl}_2\text{-4SC(NH}_2)_2$ (DTF) and the Br-doped version of DTN, $\text{Ni(Cl}_{1-x}\text{Br}_x)_2\text{-4SC(NH}_2)_2$, through magnetization, magnetic susceptibility and specific heat measurements. For DTN we studied the crossover from the quasi-1D behaviour to the 3D ordered phase and compared our experimental results with Quantum Monte-Carlo (QMC) calculations. We delimited the region correspondent to the quasi-1D behaviour right above the portion of the phase diagram correspondent to the Bose-Einstein condensation (BEC) of magnons, detecting the reminiscence of a Tomonaga-Luttinger-liquid (TLL) regime related to the weakly coupled 1D magnetic chains in DTN. Also, we extended our studies to higher temperatures, where the spin correlations become negligible. This allowed us to verify some discrepancies in the value of the single-ion anisotropy parameter D . Regarding the DTM compound, our specific heat measurements showed the existence of two antiferromagnetic transitions for temperatures down to 60 mK and fields up to 1.4 T and we discuss some hypothesis for such phenomena. For DTF, our results show no magnetic ordering down to 100 mK, making this compound a candidate for frustrated magnetism. We also synthesized Br-doped DTN samples with different concentrations of bromine ion dopant and performed magnetic susceptibility measurements, constructing the phase diagram as a function of the critical temperature, critical magnetic field and the Br content in the samples. From these results we studied the influence of the amount of Br doping in the system. Finally, we present our preliminary results regarding the influence of pressure in magnetic measurements of DTN. From our experimental results combined with mean-field theory we estimate the critical pressure p_c to close the energy gap and so promote a pressure-induced transition.

Keywords: Bose-Einstein Condensation, DTN, antiferromagnetism.

List of abbreviations

AC: Alternating current

ADR: Adiabatic Demagnetization Refrigerator

AFM: Antiferromagnet / Antiferromagnetic

BEC: Bose-Einstein Condensate / Bose-Einstein Condensation

CW : Curie-Weiss

DR: Dilution Refrigerator

DTC: $\text{CdCl}_2\text{-4SC(NH}_2)_2$

DTF: $\text{FeCl}_2\text{-4SC(NH}_2)_2$

DTM: $\text{MnCl}_2\text{-4SC(NH}_2)_2$

DTN: $\text{NiCl}_2\text{-4SC(NH}_2)_2$

SSE: Stochastic Series Expansion method

QMC: Quantum Monte-Carlo

SQUID: Superconducting Quantum Interference Device

TLL: Tomonaga-Luttinger Liquid

VSM: Vibrating Sample Magnetometer

XRD: X-ray diffraction

XRF: X-ray fluorescence

ZFS: Zero-field splitting

χ_{DC} : Magnetization divided by the DC external magnetic field H .

Summary

1	Introduction	1
1.1	About this thesis	4
2	Theoretical background	5
2.1	Exchange interactions	5
2.1.1	Superexchange interactions	7
2.2	The Zeeman term	8
2.3	Zero-field splitting	8
2.4	Magnetic properties of DTN	9
2.5	XXZ model and BEC of magnons	13
2.5.1	XXZ model in one dimension	13
2.5.2	XXZ model in three dimensions	14
2.5.3	BEC of magnons	16
2.6	Heat capacity	18
2.6.1	Lattice contribution to the heat capacity	19
2.6.2	Magnetic contribution to the heat capacity	21
2.6.3	Schottky anomaly	23
2.6.4	Entropy	24
2.7	Quantum Monte-Carlo and the Stochastic Series Expansion method	25
3	Samples: Crystal structure, preparation and characterization	27
3.1	Crystal structure of the compounds	27
3.2	Method of supersaturated solution	29
3.3	Synthesis of the samples	29
3.3.1	DTN	29
3.3.2	DTM and DTC	30
3.3.3	DTF	30
3.3.4	DTN-Br	31
3.4	XRD characterization and Rietveld refinement	31
3.5	X-ray Fluorescence	33
3.5.1	Analysis	33

4	Experimental techniques	37
4.1	MPMS SQUID magnetometer	37
4.2	PPMS	40
4.2.1	Specific heat measurements	40
4.2.2	Slope analysis	42
4.2.3	Vibrating Sample Magnetometer (VSM) option	42
4.2.4	Dilution Refrigerator (DR) option	43
4.3	AC susceptibility and VSM measurements setups	45
4.4	Adiabatic Demagnetization Refrigeration (ADR)	47
5	Quasi-1D regime in DTN	51
5.1	Quasi-1D systems in condensed matter	51
5.2	Results for the quasi-1D regime	54
5.3	Higher temperatures ($T > J_c/k_B$) results	58
5.4	Conclusions	60
6	Magnetic and Specific heat investigations on DTM and DTF compounds	63
6.1	DTM and DTF compounds	63
6.2	Results from magnetic measurements	65
6.3	Results from specific heat measurements for DTM	73
6.4	Results from specific heat measurements for DTF	78
6.5	Considerations about the exchange interactions in DTM and DTF	82
6.6	Conclusions	84
7	Magnetic susceptibility studies on Br-doped DTN	85
7.1	Disorder in quantum magnets and Br-doped DTN	85
7.2	Results	86
7.3	Conclusions	90
8	Preliminary studies on pressure in DTN	93
8.1	Effect of pressure in field-induced antiferromagnets	93
8.2	Hydrostatic pressure cell	96
8.2.1	Hardening of CuBe	96
8.2.2	Designs for the pressure cell	97
8.3	Effects of pressure in DTN	100
8.4	Conclusions	104
9	Conclusions and perspectives	105
A	System with two particles with spin-1/2	109
B	Spin matrices	111

C Magnetization and magnetic susceptibility of ideal paramagnets	113
C.1 Evaluation of magnetization and magnetic susceptibility	113
C.2 Expressions for H applied parallel to c -axis	113
C.3 Expressions for H applied perpendicular to c -axis	115
Bibliography	117

Chapter 1

Introduction

The existence of magnetic properties in matter is known, at least, since the origin of the first civilizations and the invention of writing. Chinese, Greek and Indian ancient civilizations knew and used the properties of loadstone for many purposes, from the invention of compass in China to the removal of pieces of spears from injured soldiers as mentioned in ancient treaties of medicine in India [1]. Studies of magnetism and the magnetic properties of matter has been carried on across the centuries and more intensively since the 19th century, when the foundations of the electromagnetism were established. Later, in 20th century, from the advent of the statistical mechanics and the newborn quantum mechanics, microscopic theories were formulated and since then substantial efforts on theoretical and experimental investigations has been made to unveil the many properties of matter, specially the magnetism.

Currently we have the knowledge of several types of magnetic ordering. Since there are many, describing each one of them can be a difficult task. Here we are interested in discuss a specific type of magnetic ordering known as *antiferromagnetism*.

The idea of antiferromagnets was first proposed by L. M. Néel in 1948 [2], where he idealized that such behaviour consists in a collection of magnetic dipoles, each one located in a site of a crystal lattice, being the orientation of such dipoles opposite regarding their first neighbours. In absence of an external magnetic field, the total magnetization of this system is zero. Such ordering exists below a certain temperature, known as *Néel temperature*. Above such temperature the system is a paramagnet.

The first experimental evidence of antiferromagnetic ordering came few years later, in 1951, by C. G. Shull, W. A. Strauser, and E. O. Wollan in neutron scattering and neutron diffraction measurements on different substances [3]. In fact these techniques are the "smoking gun" to determine the magnetic ordering in materials. They also serve to study the different types of collective excitations present in solids. Sound examples of such excitations are the quantized lattice vibrations, known as *phonons* and the quantized spin waves in magnets, the so-called *magnons*.

Magnons were first idealized by F. Bloch in 1930 in order to explain the spontaneous magnetization in ferromagnets [4]. Later, in 1957, B. N. Brockhouse achieved the first

experimental evidences of magnons from inelastic neutron scattering [5].

It is a known fact that magnons are collective excitations with a integer spin, which means that they are bosons and consequently obey the Bose-Einstein statistics. In 1956 T. Matsubara and H. Matsuda were interested in studying the properties of liquid helium at zero temperature. Describing it by a lattice model, the authors introduced a transformation in which they mapped a weakly interacting Bose gas into spins in a lattice. In this sense, they showed the correspondence between a weakly interacting Bose gas with some magnets, where the bosons in this case are nothing but magnons [6].

Since then, this correspondence started to be explored and the possibility for the occurrence of the so-called Bose-Einstein condensation of magnons was predicted in later studies [7–10].

Bose-Einstein condensation (BEC) occurs when a system of bosons is sufficiently cooled down to promote a macroscopic occupation of a single quantum state. The first hint related to the occurrence of a BEC came from studies of the helium superfluid phase. In fact the Bose-Einstein statistics makes quantitative predictions of the superfluid helium, such as the lambda shape of specific heat curve and the existence of quantized vortices. However, theoretical predictions state that at zero temperature the condensed fraction in helium is not larger than 10%. Also, neutron scattering experiments are elusive to determine such macroscopic occupation of helium atoms in the lowest energy state [11]. The strong interactions among atoms in helium prevent the macroscopic occupation of a single quantum state. Thus, such occupation can be achieved in a diluted system at low temperatures, as performed by the groups of E. Cornell and C. Weiman in JILA using a dilute gas of ^{87}Rb and W. Ketterle in MIT from a ^{23}Na dilute gas, both in 1995 [12, 13].

The occurrence of BEC has been also studied in other diluted gases [11, 14] as well as in other contexts, including the condensation of excitons-polaritons in semiconductor cavities [15] and BEC of magnons in ferromagnetic [16] and field-induced antiferromagnetic materials [17].

The first interpretation of an experimental data as being a BEC of magnons is dated to 1999 [18, 33], when the authors studied the spin-gapped magnetic compound TlCuCl_3 and related the observation of field-induced Néel ordering as a BEC of magnons. After this, BEC of magnons were observed in other quantum magnets, like $\text{BaCuSi}_2\text{O}_6$, KCuCl_3 , $(\text{C}_4\text{H}_{12}\text{N}_2)\text{Cu}_2\text{Cl}_6$ (PHCC), $(\text{C}_7\text{H}_{10}\text{N})_2\text{CuBr}_4$ (DIMPY), $\text{Ni}(\text{C}_9\text{H}_{24}\text{N}_4)(\text{NO}_2)\text{ClO}_4$ (NTENP), $\text{NiCl}_2\text{-4SC}(\text{NH}_2)_2$ (DTN) and many others [17].

Not only BEC, but also other leading edge topics on the so-called *emergent phenomena* has been studied in some of these compounds, which may bring some enlightenment on the understanding of current open problems in condensed matter physics.

A first example of such problems are systems of interacting fermions that cannot be described by the Fermi liquid theory and are often called *strange metals* [19]. One example of Fermi system that is not described by the Fermi liquid theory are interacting fermions in 1D. In this system, the so-called *Tomonaga-Luttinger Liquid* (TLL) regime has been studied in different contexts, including field-induced antiferromagnets such as NTENP [20]

and DIMPY [21], where the TLL regime is observed for temperatures right above those for the BEC of magnons in these compounds.

Another example is the geometrical frustration in magnetic systems, where competing interactions among atoms lead to non-trivial spins orientations. This may leads not only to exotic regimes like spin glasses, spin ices and spin liquids but also to exotic topological phases such as *skyrmions* and analogues to magnetic monopoles [22,23].

We can also mention the effects of disorder in quantum magnets that exhibit BEC of magnons. Such systems provide an alternative route to explore disorder in bosonic systems and quantum phase transitions like the BEC-to-Bose Glass (BG) transition where, driven by an external parameter such the external magnetic field, the bosons in the BEC phase became confined in localized regions, forming superfluid clusters of different sizes, which characterizes the BG phase. This transition is analogous to the Anderson localization in fermionic systems [17]. In quantum magnets, the BEC-to-BG transiton has been studied in some compounds by bromine doping, as in the case of DTN [24,25] and in the IPA-CuCl₃, where some Cl atoms are replaced by Br atoms [26–28,38], and in the case of TlCuCl₃ where some Tl atoms are replaced by K atoms [29–32].

Finally some studies have been focused in exploring the effects of pressure in the phase diagram of field-induced antiferromagnets. In this case, instead of a phase transition driven by the application of external magnetic fields, phase transitions are achieved by applying pressure in these compounds. Some examples of systems in which pressure-induced phase transitions are achieved are the TlCuCl₃ [33–37], IPA-CuCl₃ [38], PHCC [39] and CsFeCl₃ [40]. The possibility of studying the effects of pressure in strongly correlated systems have been unveiling new horizons on the understanding of such systems, which calls attention of scientific community and stimulates new efforts for studying pressure in condensed matter systems.

In our group, studies are focused on the properties of the DTN compound. From all known quantum magnets which exhibit BEC of magnons, DTN manifest its phase in relatively low magnetic fields ($H_{c1}=2.1$ T and $H_{c2}=12.6$ T) and high temperatures (up to $T_c=1.2$ K) comparing to other materials [17]. Also, one of the advantages of the DTN is the easy preparation of the samples, as described in the next chapters.

In this thesis we present our results regarding the studies of the DTN and related compounds on some of these aforementioned emergent phenomena. We identified the existence of a quasi-1D TLL-like regime in DTN, the existence of two phase transitions in the related compounds MnCl₂-4SC(NH₂)₂ (DTM) and the possibility of magnetic frustration in the compound FeCl₂-4SC(NH₂)₂ (DTF), the influence of disorder in the DTN phase diagram, where the disorder is induced by chemical dopping of Br ions in the DTN and also we made some attempting studying the influence of pressure on the magnetic measurements of DTN.

1.1 About this thesis

This thesis is divided as follow. In Chapter 2 we give an overview of the physics involved in the compounds studied. We start presenting some considerations about magnetic ordering and exchange interactions, Zeeman effect and zero-field splitting, which are the ingredients to describe our magnetic systems. Then, we discuss the magnetic behaviour of DTN compound and the mapping from a spin hamiltonian to the weakly interacting Bose gas hamiltonian, which motivates the studies of Bose-Einstein condensation of magnons in quantum magnets. Later, some considerations about the specific heat are presented. Finally we outline the Quantum Monte-Carlo (QMC) method of Stochastic Series Expansion, used to compare the theoretical description of the compounds with our experimental results.

The Chapter 3 is devoted to describe the preparation and X-ray characterization of the samples used in this work by diffractometry and fluorescence techniques.

Following, in the chapter 4 we give a description of the measurements instruments for magnetization, magnetic susceptibility and specific heat used in this work.

The first results of this work are presented in Chapter 5 where, from magnetic and specific heat measurements and QMC calculations, we investigate the existence of a quasi-1D regime in DTN and we point out the difference of values for the single-ion anisotropy parameter D reported in the literature and our findings, which have a good agreement with some of the reported values.

In Chapter 6 we report our results, also from magnetic and specific heat measurements, of the DTM and DTF compounds, where we found the existence of antiferromagnetic orderings in the DTM compound, highlighted by the existence of a double peak in the specific heat curve. For the DTF compound we discuss the possible influence of magnetic frustration.

The final results of this work, concerning the magnetic susceptibility measurements of Br-doped DTN samples with different concentrations of bromine dopant are presented in Chapter 7.

In Chapter 8 we discuss our efforts in studying the effects of pressure in DTN magnetic properties and present an estimate value for the critical pressure p_c necessary to close the energy gap and promote a pressure-induced transition.

The conclusions of this work and the perspectives of future works involving the compounds studied in this thesis are given in Chapter 9.

Chapter 2

Theoretical background

In this chapter we introduce the theoretical background necessary to understand the systems studied in this work. First we discuss the exchange interactions, Zeeman splitting and zero-field splitting, which are necessary in the description of our systems. Then, we present some general remarks on the magnetic properties of DTN, the XXZ model, the correspondence of the XXZ model with a diluted bose gas and then the Bose-Einstein condensation of magnons in some magnetic system, specially in DTN. Finally we discuss the contributions to the specific heat in our systems and give a brief overview regarding the Quantum Monte-Carlo method of Stochastic Series Expansion used to corroborate some of our experimental results.

2.1 Exchange interactions

It is known that a single atom displays magnetic behaviour. Every atom presents a weak diamagnetic response and, if such atom has unpaired electrons, a paramagnetic behaviour is also present.

Nevertheless, in general, we study systems with large number of atoms (10^{23} , as a typical example). These atoms interact each other in many ways and in what concerns the magnetic behaviour of the whole system, these interactions can lead to a vast number of different types of magnetic behaviours beyond the diamagnetism and paramagnetism of a single atom.

Classifying and describe every single type of magnetic behaviour is very difficult since the source of such behaviour are distinct and depends on many conditions such as the constitution of the material, its purity, the temperature, external pressure and magnetic field and so on.

For our purposes we will restrict ourselves to a simple example from which we can take, in part, the necessary understanding of the magnetic behavior in our systems as well as in many others. Like other examples in physics we start studying a two-body problem due to its simplicity and theoretical treatability but that can be, at least, qualitatively generalized. The following discussion can be found in many textbooks. Our discussion is

based on reference [41].

So let us consider a hydrogen molecule described by the following hamiltonian:

$$\hat{\mathcal{H}} = \hat{h}_1 + \hat{h}_2 + \hat{V}_{1,2}, \quad (2.1)$$

where

$$\hat{h}_i = -\frac{\hbar^2}{2m} \nabla_i^2 - \frac{Ze^2}{4\pi\epsilon_0 r_i}, \quad (2.2)$$

is the hamiltonian for a single hydrogen atom and

$$\hat{V}_{1,2} = \frac{e^2}{4\pi\epsilon_0 |\vec{r}_1 - \vec{r}_2|}, \quad (2.3)$$

is the two-body Coulomb repulsion term.

Now we write the basis states of this system in terms of the one-body states. Since the electrons are fermions we need to obey the Pauli exclusion principle and write the basis states as antisymmetric combinations of the one-body states. This can be represented by the so-called Slater determinant

$$|\Psi_{\sigma\sigma'}(1, 2)\rangle = \frac{1}{\sqrt{2}} \begin{vmatrix} |\psi_{a\sigma}(1)\rangle & |\psi_{a\sigma'}(2)\rangle \\ |\psi_{b\sigma}(1)\rangle & |\psi_{b\sigma'}(2)\rangle \end{vmatrix}, \quad (2.4)$$

where $|\psi_{p\sigma}(n)\rangle$ is the one-body state for a particle p in a state n and spin $\sigma = \uparrow$ or \downarrow .

So, we have the basis states for this system given by

$$|\Psi_{\uparrow\uparrow}(1, 2)\rangle = \frac{1}{\sqrt{2}} [|\psi_{a\uparrow}(1)\rangle|\psi_{b\uparrow}(2)\rangle - |\psi_{a\uparrow}(2)\rangle|\psi_{b\uparrow}(1)\rangle] \quad (2.5a)$$

$$|\Psi_{\uparrow\downarrow}(1, 2)\rangle = \frac{1}{\sqrt{2}} [|\psi_{a\uparrow}(1)\rangle|\psi_{b\downarrow}(2)\rangle - |\psi_{a\uparrow}(2)\rangle|\psi_{b\downarrow}(1)\rangle] \quad (2.5b)$$

$$|\Psi_{\downarrow\uparrow}(1, 2)\rangle = \frac{1}{\sqrt{2}} [|\psi_{a\downarrow}(1)\rangle|\psi_{b\uparrow}(2)\rangle - |\psi_{a\downarrow}(2)\rangle|\psi_{b\uparrow}(1)\rangle] \quad (2.5c)$$

$$|\Psi_{\downarrow\downarrow}(1, 2)\rangle = \frac{1}{\sqrt{2}} [|\psi_{a\downarrow}(1)\rangle|\psi_{b\downarrow}(2)\rangle - |\psi_{a\downarrow}(2)\rangle|\psi_{b\downarrow}(1)\rangle]. \quad (2.5d)$$

When we evaluate the elements of the hamiltonian (2.1), if $\sigma = \sigma'$, we have

$$\langle \Psi_{\sigma\sigma'}(1, 2) | \hat{h}_i | \Psi_{\sigma\sigma'}(1, 2) \rangle = E_i, \quad (2.6)$$

where E_i are the eigenenergies for the hydrogen atom. We also have two different terms when we evaluate $\langle \Psi_{\sigma\sigma'}(1, 2) | \hat{V}_{1,2} | \Psi_{\sigma\sigma'}(1, 2) \rangle$. The first term, is the Coulomb term

$$C = \frac{e^2}{4\pi\epsilon_0} \int \int \frac{|\psi_a(\mathbf{r}_1)|^2 |\psi_b(\mathbf{r}_2)|^2}{|\mathbf{r}_1 - \mathbf{r}_2|} d\mathbf{r}_1 d\mathbf{r}_2, \quad (2.7)$$

and the second is the so called *exchange integral*

$$J = -\frac{e^2}{4\pi\epsilon_0} \int \int \frac{\psi_a^*(\mathbf{r}_1)\psi_b(\mathbf{r}_1)\psi_a(\mathbf{r}_2)\psi_b^*(\mathbf{r}_2)}{|\mathbf{r}_1 - \mathbf{r}_2|} d\mathbf{r}_1 d\mathbf{r}_2, \quad (2.8)$$

which we can interpret as how much the two wavefunctions overlap.

We can write the hamiltonian (2.1) in a matrix form as

$$\hat{\mathcal{H}} = (E_a + E_b) \begin{pmatrix} 1 & 0 & 0 & 0 \\ 0 & 1 & 0 & 0 \\ 0 & 0 & 1 & 0 \\ 0 & 0 & 0 & 1 \end{pmatrix} + \begin{pmatrix} C + J & 0 & 0 & 0 \\ 0 & C & J & 0 \\ 0 & J & C & 0 \\ 0 & 0 & 0 & C + J \end{pmatrix}. \quad (2.9)$$

From the results presented in Appendix A, the above hamiltonian can be written as

$$\hat{\mathcal{H}} = \left(E_a + E_b + C + \frac{J}{2} \right) + 2J\mathbf{S}_1\mathbf{S}_2. \quad (2.10)$$

As we can see from (2.8) the sign of J depends on the product of wavefunctions and their symmetries. When J is negative, a parallel alignment of the spins is favoured and it is known as a *ferromagnetic interaction*. In the case of J positive, the spins are found in an antiparallel alignment, what is called a *antiferromagnetic interaction*.

All this discussion was made considering a two atom system. Now let us generalize this result for a many body system with pair interactions. Omitting the constants and conveniently rescaling the exchange term we can finally write the hamiltonian of the Heisenberg model

$$\hat{\mathcal{H}} = \sum_{ij} J_{ij} \mathbf{S}_i \mathbf{S}_j. \quad (2.11)$$

From this model a large number of magnetic orderings are described. Some overview of these possibilities can be found in reference [42].

2.1.1 Superexchange interactions

In some solids, the atoms are far apart enough to make the exchange interactions between them very small. Also small exchange interactions are found when the wavefunctions are fairly localized. In these examples, any collective magnetic behaviour of the system is expected to be suppressed and noticeable only in a such low temperature range that may be not accessible experimentally.

Nevertheless there are situations as those listed in which a reasonable exchange between the atoms is found and so a collective magnetic behaviour of the system is observable. In such situations the interaction between two magnetic ions are mediated by non-magnetic ligand located between them [43].

As an example we can mention the interaction between two Ni^{2+} ions mediated by a Cl ligand. In this case an electron from the p_z orbital of Cl ligand exchanges with the half-filled

d_z^2 orbital of Ni^{2+} ion [44]. This mechanism result in an indirect exchange between the Ni ions and it is known as a *superexchange interaction*.

2.2 The Zeeman term

When an atom experiences an external magnetic field it is observed that such field breaks the degeneracy of the energy levels and promotes its splitting. This phenomena is known as *Zeeman effect* [45].

Let us consider an external magnetic field H applied parallel to the z axis of our coordinate system. In this situation, a system described by the hamiltonian (2.11) will have an additional term given by

$$\mathcal{H}_{zeeman} = -g\mu_B \sum_{\mathbf{r}} S_{\mathbf{r}}^z, \quad (2.12)$$

where g is the *gyromagnetic factor* and μ_B is the *Bohr magneton*.

2.3 Zero-field splitting

In an atom with two or more unpaired electrons, which results in a ground state spin multiplicity larger than 2, the interactions among the electrons promotes the splitting of degenerate energy levels even in the absence of an external magnetic field [46]. This phenomena is known as *Zero-Field Splitting* (ZFS) and it causes a single-ion anisotropy [44].

There are two main sources for the ZFS. The first one is the dipole-dipole interaction, which is the most important contribution to the ZFS. The second one is the spin-orbit coupling [47]. In this work we are interested in discuss the ZFS due to the dipole-dipole interactions.

To present an overview about the derivation of the ZFS hamiltonian let us start from the hamiltonian for the dipole-dipole interaction

$$\mathcal{H}_{DD} = g^2 \mu_B^2 \left[\frac{\mathbf{s}_1 \cdot \mathbf{s}_2}{r^3} - 3 \frac{(\mathbf{s}_1 \cdot \mathbf{r})(\mathbf{s}_2 \cdot \mathbf{r})}{r^5} \right]. \quad (2.13)$$

Regarding the spin operators for two 1/2-spin particles introduced in Appendix A we have $\mathbf{S}_i = \mathbf{s}_{1i} + \mathbf{s}_{2i}$ and $2\mathbf{s}_{1i}\mathbf{s}_{2i} = \mathbf{S}_i^2 - \frac{1}{2}$ with $i = x, y, z$. Developing equation (2.13) and using such relations, we have [48]

$$\begin{aligned} \mathcal{H}_{DD} = \frac{1}{2} g^2 \mu_B^2 \left[\frac{r^2 - 3x^2}{r^5} \mathbf{S}_x^2 + \frac{r^2 - 3y^2}{r^5} \mathbf{S}_y^2 + \frac{r^2 - 3z^2}{r^5} \mathbf{S}_z^2 - \right. \\ \left. - \frac{3xy}{r^5} (\mathbf{S}_x \mathbf{S}_y + \mathbf{S}_y \mathbf{S}_x) - \frac{3yz}{r^5} (\mathbf{S}_y \mathbf{S}_z + \mathbf{S}_z \mathbf{S}_y) - \frac{3zx}{r^5} (\mathbf{S}_z \mathbf{S}_x + \mathbf{S}_x \mathbf{S}_z) \right]. \quad (2.14) \end{aligned}$$

For convenience let us write the above expression as $\mathcal{H} = \mathbf{S} \mathbf{D} \mathbf{S}$, where \mathbf{D} is a tensor

whose the elements are

$$D_{ij} = \frac{1}{2}g^2\mu_B^2 \left\langle \psi_T \left| \frac{r^2\delta_{ij} - 3ij}{r^5} \right| \psi_T \right\rangle, \quad (2.15)$$

where $|\psi_T\rangle$ are triplet wavefunctions.

Choosing a proper basis, the hamiltonian $\mathcal{H} = \mathbf{S}\mathbf{D}\mathbf{S}$ can be written in a diagonal form as

$$\mathcal{H}_{ZFS} = D_{xx}\mathbf{S}_x^2 + D_{yy}\mathbf{S}_y^2 + D_{zz}\mathbf{S}_z^2. \quad (2.16)$$

After some algebraic manipulations in equation (2.16) we end up with our final form for the ZFS hamiltonian

$$\mathcal{H}_{ZFS} = D \left[\mathbf{S}_z^2 - \frac{1}{3}S(S+1) \right] + E (\mathbf{S}_x^2 - \mathbf{S}_y^2), \quad (2.17)$$

where

$$D = \frac{3}{2}D_{zz} \quad \text{and} \quad E = \frac{1}{2}(D_{xx} - D_{yy}). \quad (2.18)$$

2.4 Magnetic properties of DTN

Most of this work is devoted to study some features of the compound $\text{NiCl}_2 \cdot 4\text{SC}(\text{NH}_2)_2$, named *dichloro-tetrakis-thiourea-nickel*, or simply DTN. It has a body-centred structure in tetragonal symmetry. The chlorine atoms are arranged along the c -axis and are responsible for the superexchange interactions J_c among the Ni^{2+} ions, while in the ab -plane the Ni^{2+} ions display an exchange interaction J_{ab}

In figure 2.1 we present a simplified version of the DTN structure.

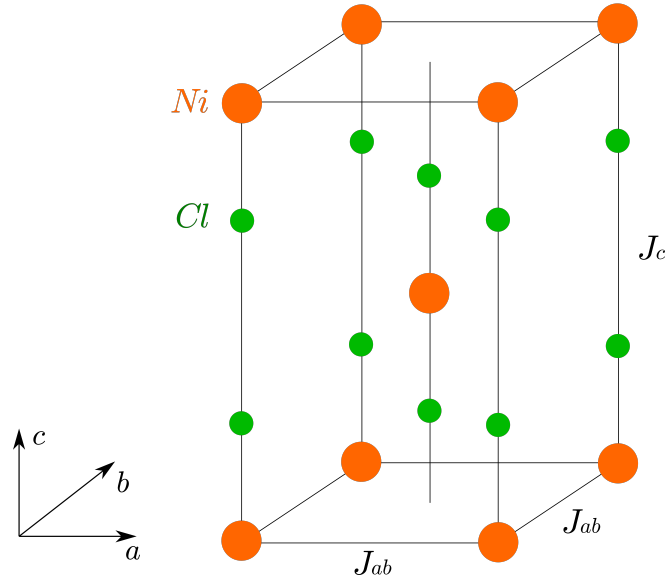


Figure 2.1: Simplified version of the DTN structure (omitting S,C,N and H) atoms denoting the exchange interactions J_{ab} and J_c between the Ni^{2+} ions.

As discussed in the previous sections, the exchange interactions are responsible for the magnetic ordering displayed in the system. Also, the magnetic ordering is subject to other factors, such the single-ion anisotropy from the zero-field splitting and the Zeeman effect in the case that the system is under external magnetic fields.

To describe the magnetic properties of DTN, we take into account all these aforementioned terms. In this sense, this $S = 1$ system is described by the follow hamiltonian

$$\mathcal{H} = J_{ab} \sum_{\mathbf{r}, ab} \vec{S}_{\mathbf{r}} \vec{S}_{\mathbf{r}+\mathbf{e}_{ab}} + J_c \sum_{\mathbf{r}, c} \vec{S}_{\mathbf{r}} \vec{S}_{\mathbf{r}+\mathbf{e}_c} + D \sum_{\mathbf{r}} (S_{\mathbf{r}}^z)^2 - g\mu_B H \sum_{\mathbf{r}} S_{\mathbf{r}}^z, \quad (2.19)$$

with $J_{ab}/k_B = 0.18$ K, $J_c/k_B = 2.2$ K, $D/k_B = 8.9$ K, and $g = 2.2$, estimate in thermodynamic [50], neutron scattering [54] and electron spin resonance measurements [51].

Although DTN is an antiferromagnetic system, the antiferromagnetic ordering in DTN does not manifests itself at $H = 0$ T just by decreasing the temperature. The first studies on the magnetic properties of DTN in 1981 by A. Paduan-Filho *et al* [49] showed that it is a field-induced antiferromagnetic compound, in which the antiferromagnetic ordering exists after the application of an external magnetic field H greater than 2 T applied parallel to the c -axis. After, it was shown that for fields greater than $H = 12.6$ T, the system becomes spin polarized [50]. In figure 2.2 we present the DTN phase diagram obtained from magnetocaloric and magnetization measurements as well as from Quantum Monte-Carlo (QMC) calculations [51].

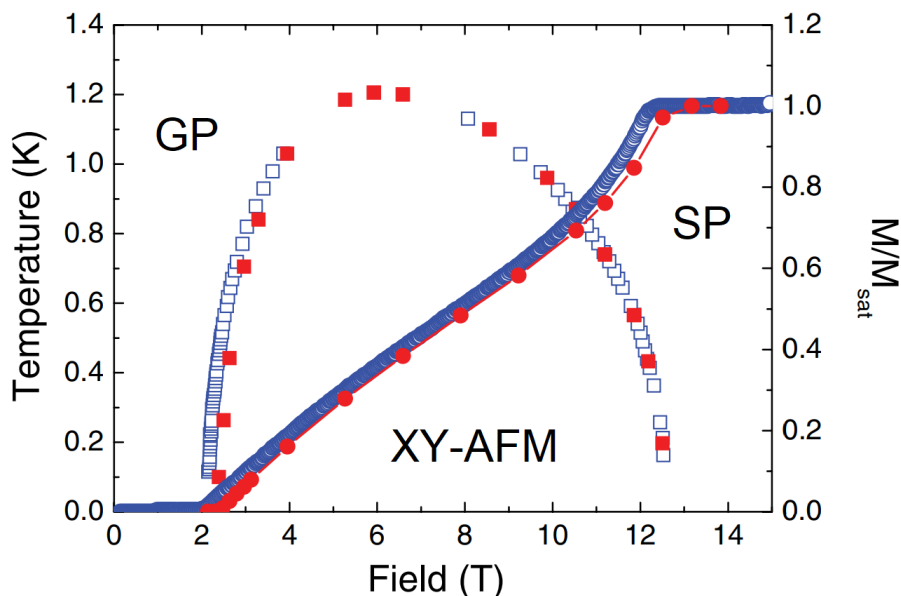


Figure 2.2: Phase diagram of DTN determined from magnetocaloric measurements (open squares) and magnetization measurements (open blue circles) with the external magnetic field applied along the c -axis of the samples. Full red squares and circles are results from QMC calculations. The abbreviation GP stands for the gapped phase, while XY-AFM is the antiferromagnetic phase in the XY plane and SP is the spin polarized phase. This figure was adapted from reference [51].

Elastic neutron scattering (ENS) measurements confirmed the antiferromagnetic ordering in DTN and showed that such ordering happens with the antiparallel alignment of the magnetic moments in the ab -plane [52]. Figure 2.3 illustrates the magnetic ordering of DTN for different values of the external magnetic field applied along the c -axis.

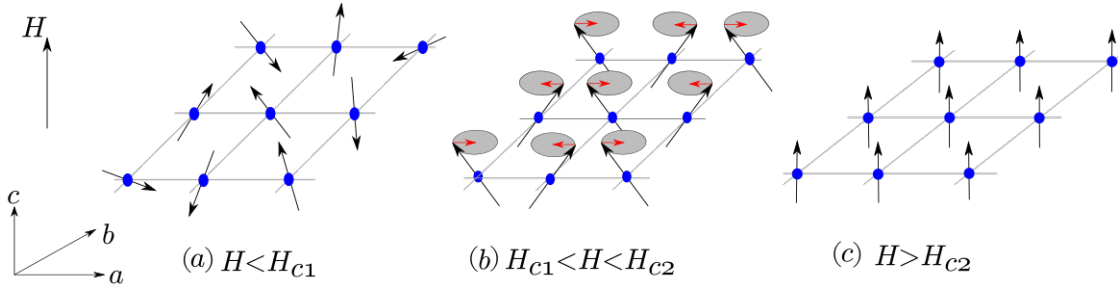


Figure 2.3: Magnetic ordering in DTN for different values of external magnetic field. For $H < H_{c1}$ applied parallel to c -axis (figure a) the system is in the gapped (non-magnetic) phase and so no magnetic ordering is expected. As the field increases, for $H_{c1} < H < H_{c2}$ the gap closes and the system presents a field-induced antiferromagnetic ordering in the ab -plane (red arrows). When the external field is $H > H_{c2}$ the spins are polarized along the c -axis.

Another important feature of DTN is that, although its structure consists in two interpenetrating sublattices, as shown in figure 2.4, no indicative of magnetic frustration was found within the experimental error [53, 54].

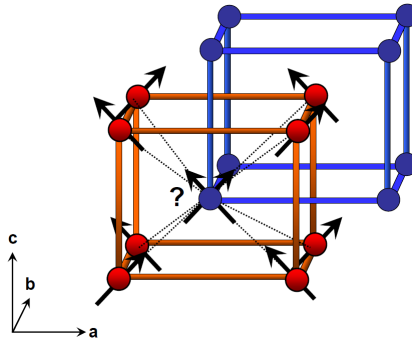


Figure 2.4: Illustration of the DTN body-centered tetragonal structure with two sublattices. Dashed lines represents frustrate couplings that, for DTN are very small. This figure was adapted from reference [53].

The field-induced antiferromagnetic phase in DTN is due to the high single-ion anisotropy which originates a gap between the non-magnetic ground state $S^z = 0$ and the first excited (magnetic) state $S^z = \pm 1$. When such gap closes due to the application of an external magnetic field, there is the overlap between these two states and then the antiferromagnetic ordering takes place. In figure 2.5 we present a schematic representation for the energy levels of Ni^{2+} ion and DTN.

For a linear Heisenberg antiferromagnetic chain with integer spin, as in the case of DTN, F. D. M. Haldane [55, 56] conjectured that must exist an energy gap between a

non-magnetic ground state and lowest-lying excited magnetic state. The size of this gap, known as *Haldane gap* depends on the single-ion anisotropy parameter D . Increasing D , the size of the gap reduces up to a critical value $D_c \simeq J$, when the gaps closes. However for $D > 2J$ the gap reopens due to the doubly-degenerate excitonic modes and, in this case, it is known as *large- D gap* [57–59].

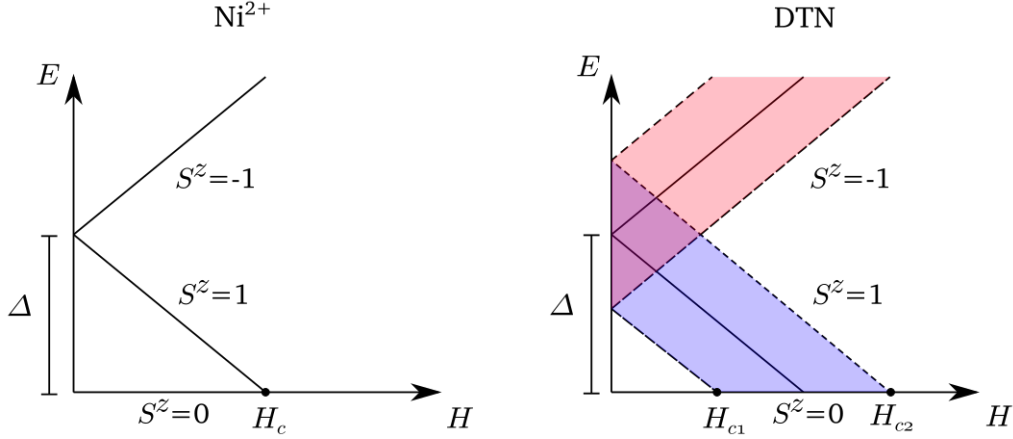


Figure 2.5: Schematic representation for the energy levels of a Ni^{2+} ion (left panel) and the DTN energy levels (right panel). Due to the Ni^{2+} single-ion anisotropy a gap Δ between the $S^z = 0$ ground state and the excited level $S^z = \pm 1$ is present. The application of an external magnetic field H is responsible for the splitting of the excited level, due to the Zeeman effect, and the level crossing at a field H_c . In the case of DTN, the existence of exchange couplings promotes a broad dispersion for the excited level [60].

An expression for the energy gap is obtained from a bosonic representation of spin operators from the DTN hamiltonian (2.19). Using the diagram technique and treating the exchange couplings as perturbations, A. V. Sizanov and A. V. Syromyatnikov obtained an approximation to the dispersion relation for DTN at $H=0$ T [61, 62]

$$\begin{aligned} \omega(\mathbf{k}) = & D + 2 \sum_{\nu} J_{\nu} \cos k_{\nu} + \frac{1}{D} \left[3 \sum_{\nu} J_{\nu}^2 - 2 \left(\sum_{\nu} \cos k_{\nu} \right)^2 \right] + \\ & + \frac{1}{D^2} \left[2 \sum_{\nu} J_{\nu}^3 + 4 \left(\sum_{\nu} \cos k_{\nu} \right)^3 + \frac{5}{2} \sum_{\nu} J_{\nu}^3 \cos k_{\nu} - 7 \left(\sum_{\mu} J_{\mu}^2 \right) \left(\sum_{\nu} J_{\nu} \cos k_{\nu} \right) - \right. \\ & \left. - 2 \left(\sum_{\mu} J_{\mu} \cos k_{\mu} \right) \left(\sum_{\nu} J_{\nu}^2 \cos k_{\nu} \right) \right], \quad (2.20) \end{aligned}$$

with $\nu = a, b, c$.

Even for external fields close to the critical field H_{c1} equation (2.20) is a good approximation. Since the smallest value of $\omega(\mathbf{k})$ is obtained for $\mathbf{k} = (\pi, \pi, \pi)$, the expression for the energy gap is given by

$$g\mu_B H_{c1} = \Delta = \omega[\mathbf{k} = (\pi, \pi, \pi)], \quad (2.21)$$

where, neglecting $\mathcal{O}(1/D)$ contributions,

$$\Delta = D - 2J_c - 4J_{ab}. \quad (2.22)$$

For higher fields the antiferromagnetic phase is suppressed and a spin polarized phases arises. In this case is also possible to write an expression for the dispersion relation of equation (2.19). From such expression we have

$$\epsilon(\mathbf{k}) = g\mu_B H - D - 2 \left(\sum_{\nu} J_{\nu} \right) + 2 \left(\sum_{\nu} J_{\nu} \cos k_{\nu} \right), \quad (2.23)$$

and a second critical field H_{c_2} which marks the transition from the antiferromagnetic phase to the spin polarized phase is given by [62]

$$g\mu_B H_2 = D + 4 \left(\sum_{\nu} J_{\nu} \right). \quad (2.24)$$

2.5 XXZ model and BEC of magnons

Some spin hamiltonians, as in case of DTN, can be mapped into other models such as the weakly-interacting bose gas or the Hubbard model hamiltonians. Through these mappings we can interpret some magnetic phases or short-range regimes as quantum critical phenomena, like the Bose-Einstein condensation, or the Luttinger liquid regime of the quantized magnetic excitations known as *magnons*.

The simplest example of a hamiltonian that allow us to construct such mappings is the so called spin-1/2 XXZ hamiltonian. In this section we introduce such hamiltonian, starting from the one-dimensional case and afterwards describing the three-dimensional case, as well as the mappings that allow us to represent such systems in terms of fermionic and bosonic systems.

2.5.1 XXZ model in one dimension

In one-dimension, the spin-1/2 XXZ hamiltonian is given by

$$\mathcal{H}_{xxz}^{1D} = J \sum_j \left[S_j^x S_{j+1}^x + S_j^y S_{j+1}^y + \delta S_j^z S_{j+1}^z \right] - g\mu_B H \sum_j S_j^z. \quad (2.25)$$

Defining the ladder spin operators

$$S_j^{\pm} = S_j^x \pm iS_j^y, \quad (2.26)$$

and applying such operators in the XXZ hamiltonian leads to

$$\mathcal{H}_{xxz}^{1D} = J \sum_j \left[\frac{1}{2} \left(S_j^+ S_{j+1}^- + S_j^- S_{j+1}^+ \right) + \delta S_j^z S_{j+1}^z \right] - g\mu_B H \sum_j S_j^z. \quad (2.27)$$

This last form of the XXZ hamiltonian can be mapped into a spinless Hubbard model hamiltonian using the so called Jordan-Wigner transformation [63] where spin-1/2 operators are mapped into fermionic spinless operators via a non-local transformation defined by

$$S_j^+ = c_j^\dagger e^{-i\pi \sum_{k<j} c_k^\dagger c_k}, \quad S_j^- = c_j e^{i\pi \sum_{k<j} c_k^\dagger c_k}, \quad S_j^z = c_j^\dagger c_j - \frac{1}{2}. \quad (2.28)$$

Applying these transformations in the 1D-XXZ hamiltonian (2.27) we obtain a spinless Hubbard model, given by

$$\mathcal{H} = \frac{J}{2} \sum_j \left(c_j^\dagger c_{j+1} + c_{j+1}^\dagger c_j \right) + \delta J \sum_j \left(c_j^\dagger c_j - \frac{1}{2} \right) \left(c_{j+1}^\dagger c_{j+1} - \frac{1}{2} \right) - \mu \sum_j c_j^\dagger c_j. \quad (2.29)$$

For $\delta = 0$ this model is reduced to the tight-binding model, easily diagonalized in the momentum space with $c_j = (N)^{-\frac{1}{2}} \sum_q c_q e^{ijq}$ [66]. Here we define $\mu = g\mu_B H$ which suggest that the external magnetic field applied in the z direction is related to the chemical potential of this fermionic system. This will be discussed in more detail in the next section.

2.5.2 XXZ model in three dimensions

In the three-dimensional case, the XXZ hamiltonian written in terms of the ladder operators is given by

$$\mathcal{H}_{xxz}^{3D} = J \sum_{\mathbf{r}, \mathbf{r}'} \left[\frac{1}{2} (S_{\mathbf{r}}^+ S_{\mathbf{r}'}^- + S_{\mathbf{r}}^- S_{\mathbf{r}'}^+) + \delta S_{\mathbf{r}}^z S_{\mathbf{r}'}^z \right] - g\mu_B H \sum_{\mathbf{r}} S_{\mathbf{r}}^z. \quad (2.30)$$

Although a three-dimensional form of the Jordan-Wigner transformation can be applied to the hamiltonian in (2.30), for our purposes we want to introduce another transformation which maps spins operators into bosonic ones. This transformation is defined as

$$S_{\mathbf{r}}^+ = b_{\mathbf{r}}^\dagger, \quad S_{\mathbf{r}}^- = b_{\mathbf{r}}, \quad S_{\mathbf{r}}^z = b_{\mathbf{r}}^\dagger b_{\mathbf{r}} - \frac{1}{2}, \quad (2.31)$$

was introduced by T. Matsubara and H. Matsuda in 1956, where the authors mapped a lattice model for a bose gas into the 3D-XXZ hamiltonian [64]. We note from the definition of this local transformation that it has a much simpler form if we compare to the Jordan-Wigner transformation.

Another transformation that maps spin operators into bosonic operators is the well known Holstein-Primakoff transformation [65]. However, in some applications for practical purposes, a truncated form of the Holstein-Primakoff transformation is used, which leads exactly to the Matsubara-Matsuda transformation.

Using the Matsubara-Matsuda transformation in the 3D-XXZ hamiltonian (2.30) we get

$$\mathcal{H} = \frac{J}{2} \sum_{\mathbf{r}, \mathbf{r}'} \left(b_{\mathbf{r}}^\dagger b_{\mathbf{r}'} + b_{\mathbf{r}'}^\dagger b_{\mathbf{r}} \right) + \delta J \sum_{\mathbf{r}, \mathbf{r}'} \left(b_{\mathbf{r}}^\dagger b_{\mathbf{r}} - \frac{1}{2} \right) \left(b_{\mathbf{r}'}^\dagger b_{\mathbf{r}'} - \frac{1}{2} \right) - \mu \sum_{\mathbf{r}} b_{\mathbf{r}}^\dagger b_{\mathbf{r}}, \quad (2.32)$$

where, again, $\mu = g\mu_B H$.

If we represent the bosonic operators $b_{\mathbf{r}}$ in the momentum space as

$$b_{\mathbf{k}}^\dagger = \frac{1}{\sqrt{L}} \sum_{\mathbf{r}} e^{i\mathbf{r}\mathbf{k}} b_{\mathbf{r}}^\dagger, \quad (2.33)$$

and use this representation in the hamiltonian (2.32) we finally obtain the Bose gas hamiltonian in the momentum space

$$\mathcal{H} = \sum_{\mathbf{k}} (\omega_{\mathbf{k}} - \mu) b_{\mathbf{k}}^\dagger b_{\mathbf{k}} + \frac{1}{2L} \sum_{\mathbf{k}, \mathbf{k}', \mathbf{q}} V_{\mathbf{q}} b_{\mathbf{k}+\mathbf{q}}^\dagger b_{\mathbf{k}'-\mathbf{q}}^\dagger b_{\mathbf{k}} b_{\mathbf{k}'}, \quad (2.34)$$

where

$$\omega_{\mathbf{k}} = J \sum_{\mathbf{r}} (1 + \cos k_{\mathbf{r}}) \quad \text{and} \quad V_{\mathbf{q}} = U + 2\delta J \sum_{\mathbf{r}} \cos q_{\mathbf{r}}. \quad (2.35)$$

In (2.35) we introduce the term U which represents a hard-core potential. The need of such potential is justified by the nature of the Matsubara-Matsuda transformation and their commutation relations. Remembering that spins-1/2 operators obey the commutation relations

$$\begin{aligned} [S_i^+, S_j^+] = [S_i^-, S_j^-] = [S_i^+, S_j^-] = 0, \quad [S_i^+, S_i^+] = [S_i^-, S_i^-] = 0, \\ [S_i^+, S_i^-] = 2S_i^z, \end{aligned} \quad (2.36)$$

while for bosons the commutation relations are given by

$$[b_i, b_j^\dagger] = b_i b_j^\dagger - b_j^\dagger b_i = \delta_{ij}, \quad [b_i, b_j] = [b_i^\dagger, b_j^\dagger] = 0, \quad (2.37)$$

and for fermions we have the anticommutation relations

$$\{c_i, c_j^\dagger\} \equiv c_i c_j^\dagger + c_j^\dagger c_i = \delta_{ij}, \quad \{c_i, c_j\} = \{c_i^\dagger, c_j^\dagger\} = 0 \rightarrow (c_i^\dagger)^2 = (c_i)^2 = 0. \quad (2.38)$$

Let us evaluate the commutation relations for the bosons from Matsubara-Matsuda transformation. From (2.31) and (2.36) we have that for bosons in different sites

$$[b_i, b_j^\dagger] = [b_i, b_j] = [b_i^\dagger, b_j^\dagger] = 0 \quad (i \neq j), \quad (2.39)$$

while for bosons in the same site

$$\{b_i, b_i^\dagger\} = 1, \quad \{b_i, b_j\} = \{b_i^\dagger, b_j^\dagger\} = 0 \rightarrow (b_i^\dagger)^2 = (b_i)^2 = 0 \quad (i = j). \quad (2.40)$$

Clearly, for bosons in different sites the commutation relations obtained from the Matsubara-Matsuda transformation are the usual commutation relations for bosons. However, the on-site commutation relations resembles the ones for fermions. The way to

interpret such apparent contradiction is to assume that the number occupation per site in this representation is limited to one boson. In this sense, such transformation maps a spin system into a *dilute* system of bosons and it is valid only in such condition.

In the Bose gas hamiltonian (2.34) this diluteness requirement is fulfilled if we consider in the potential term (2.35) a hard core potential like

$$U = \begin{cases} \infty, & \text{if two particles are in the same site} \\ U_0, & \text{if two particles are nearest neighbors} \\ 0, & \text{otherwise.} \end{cases} \quad (2.41)$$

2.5.3 BEC of magnons

Since the pioneering work by Matsubara and Matsuda, some speculations about the possibility for occurrence of BEC of magnons in uniaxial magnetic materials were made and finally theoretically demonstrate few decades later [7–10].

The first experimental evidence for the BEC of magnons came in 2000 with the work by T. Nikuni *et al* [18] for the compound TlCuCl_3 . After this work, efforts for finding other materials in which BEC of magnons occurs has been made in many compounds, specially field-induced antiferromagnets, and the BEC of magnons was identified in some systems. An overview of BEC in quantum magnets can be found in reference [17].

In figure 2.6 we present the phase diagram of some quantum magnets in which the BEC phase is observed.

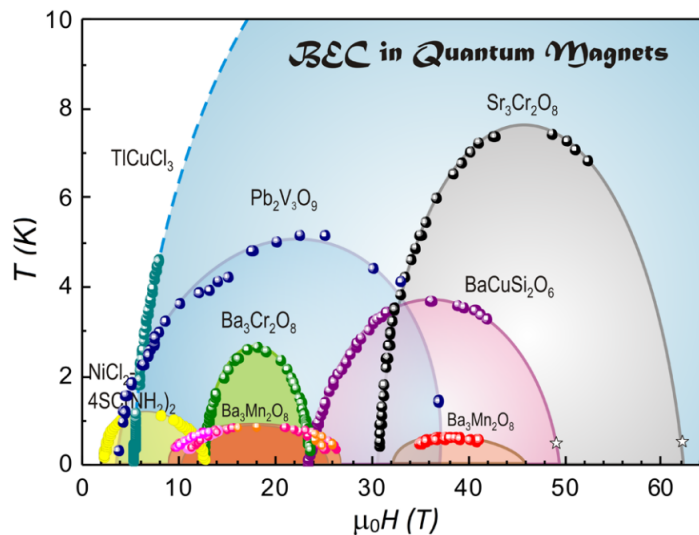


Figure 2.6: Phase diagrams of some quantum magnets in which the BEC phase of magnons is observed. This figure was adapted from reference [17].

In these compounds the BEC phase of magnons corresponds to the field-induced antiferromagnetic phase. The evidences to identify such phases are experiments of neutron

scattering, which determines the spectrum of excitations, and from measurements of thermodynamic properties and the determination of the critical exponents. A sound example, is the critical exponent ϕ from

$$H_c(T) - H_c(0) \sim T^\phi, \quad (2.42)$$

where for these compounds is close to $\phi = 3/2$, which corresponds to the value obtained for an ideal bose gas for the dependence of the chemical potential with the temperature. From the Matsuba-Matsubara mapping we learn that the chemical potential of a bose gas is related to the external magnetic field in a magnetic system, which justifies such correspondence between the critical exponents of both systems.

It is important to mention a few remarks concerning the occurrence of BEC in quantum magnets. As shown in this section, the mapping between magnetic systems and bose systems leads to the weakly interacting bose gas hamiltoninan if we consider a spin hamiltonian which obeys the uniaxial symmetry. A BEC is a system with a U(1) symmetry and a complex order parameter. In the case of XXZ antiferromagnets, we can introduce the complex order parameter $M^{AF} = \sum_{\mathbf{r}} \langle S_{\mathbf{r}}^x + iS_{\mathbf{r}}^y \rangle e^{i\mathbf{r} \cdot \mathbf{k}}$ which is non-zero in the field-induced antiferromagnetic (BEC) phase.

Another correspondences from both spin system and weakly interacting bose gas can be established from the magnetization along the z axis, which is given by

$$M_z = \sum_{\mathbf{r}} S_{\mathbf{r}}^z. \quad (2.43)$$

But from (2.31) we have $S_{\mathbf{r}}^z = n_{\mathbf{r}} - \frac{1}{2}$, which relates the z component of the spin with the number operator. So, the magnetization in the z -axis in these spin system is related to the number of bosons.

We can also interpret this result if we remember that the action of an external magnetic field promotes the emergence of magnons in the system, which are the bosons we are studying. From this fact and from (2.30) and (2.34) we interpret the external magnetic field on the system as a chemical potential.

An important requirement for the occurrence of BEC is the number conservation. In the case of magnetic systems, the uniaxial symmetry is fundamental for this requirement. However, since it is not perfectly true, the idea of BEC in a magnetic systems is an idealization, but a good approximation in many of the studied compounds [17].

In table 2.1 we summarize the correspondences between XXZ antiferromagnets and bose systems.

One of the most studied field-induced antiferromagnetic system in which the BEC phase was identified is the DTN. In fact DTN is one of the lowest critical field compounds for the observation of BEC phase (see figure 2.6). It is important to notice that all the discussion made for BEC of magnons considers a XXZ-1/2 system. Although DTN is also an uniaxial system, it is a $S = 1$ magnet. Despite this fact, all the development for BEC of magnons

presented here still holds for DTN. Regarding the energy levels of DTN in figure 2.5, we notice that close to the critical fields the $S^z = -1$ level are far apart from the $S^z = 0$ and $S^z = 1$ levels. So, in a good approximation the states $|0\rangle$ and $|1\rangle$ can be mapped into the $| -1/2\rangle$ and $|1/2\rangle$ states and the state $| -1\rangle$ can be neglected in the vicinity of the critical field and at low temperatures. It means that the description of BEC of magnons is valid specially in this conditions, where the hamiltonian of the system can be mapped into the XXZ-1/2 hamiltonian [66].

Table 2.1: Correspondence between the characteristics of a XXZ antiferromagnet and a bose system.

Antiferromagnet	Bose system
Magnetization: $M_z = \sum_{\mathbf{r}} S_{\mathbf{r}}^z$	Number of particles: $N = \sum_{\mathbf{r}} n_{\mathbf{r}}$
In-plane ordering	BEC
External magnetic field H	Chemical potential μ
$M^{AF} = \sum_{\mathbf{r}} \langle S_{\mathbf{r}}^x + iS_{\mathbf{r}}^y \rangle e^{i\mathbf{r} \cdot \mathbf{k}}$	$\Psi = \sqrt{n_0} e^{i\theta}$
Transverse spin wave stiffness	Superfluid density

It is also worth to mention that, in the literature, magnons from these triplet state are often called *triplons*. So, since the magnons that forms the condensate are those from the triplet state, the BEC of magnons is also called *BEC of triplons*. However in this work we keep the term BEC of magnons since it is the most used in the literature.

2.6 Heat capacity

The heat capacity in a solid have contributions from different sources. In many cases the total heat capacity is given by

$$C = C_{ph} + C_{mag} + C_{el} + C_{nucl}, \quad (2.44)$$

where C_{ph} is the contribution to the heat capacity due to the lattice vibrations (phonons), C_{mag} is the contribution from the magnetic ions, C_{el} is due to the electron gas and C_{nucl} is the nuclear contribution to the heat capacity.

Since in this work we study insulators, C_{el} can be neglected. The nuclear contribution, which gives a term proportional to T^{-2} [68, 69] is not seen in our measurements, so in our case we can also disregard this contribution.

In this sense, for our compounds only the lattice and the magnetic contributions are relevant. In this section we present a brief discussion about them.

2.6.1 Lattice contribution to the heat capacity

A crystal lattice can be regarded as a collection of many coupled oscillators, where atoms or molecules vibrate around their equilibrium position. According to the model proposed by P. Debye in 1912, such oscillations are small at low temperatures and then they can be considered as harmonic. This model consists in the treatment of the vibrations in the solid as a superposition of stationary elastic waves in longitudinal and transversal directions. Inspired by the treatment of the black body radiation problem proposed by M. Planck, Debye treated the lattice vibrations in a crystal as photons in a cavity. Like photons, these acoustic waves are quantized and they are called *phonons*.

In this section we derive the expression for the lattice contribution to the heat capacity following the path of many references (see [70–72]).

The energy of a phonon with polarization α (transversal or longitudinal) with momentum $\hbar\vec{k}$ and frequency $\omega_{\vec{k},\alpha}$ is

$$\varepsilon_{\vec{k},\alpha} = \hbar\omega_{\vec{k},\alpha}. \quad (2.45)$$

In this model only long wavelength vibrations are considered and then the dispersion relation is linear

$$\omega_{\vec{k},\alpha} = c_{s_\alpha}|\vec{k}|, \quad (2.46)$$

where c_{s_α} is the sound velocity in the polarization direction α . For sake of simplicity, we will consider that the lattice in this model is composed solely by one type of atom. So, the sound velocity is equal in all the polarization directions and this index will be neglected hereafter.

From (2.45) and (2.46) the energy can be expressed as

$$\varepsilon_{\vec{k}} = \hbar c_s |\vec{k}| = \hbar c_s \sqrt{k_x^2 + k_y^2 + k_z^2}. \quad (2.47)$$

Since we have stationary waves the wavevectors in a cubic solid with length L is

$$\vec{k} = (k_x, k_y, k_z) = \frac{2\pi}{L} (n_x, n_y, n_z), \quad (2.48)$$

with $-\pi/d < (k_x, k_y, k_z) \leq \pi/d$, where d is the spacing between two atoms in the lattice and n_α are integer numbers. This relation restricts the wavevectors to the first Brillouin zone, which means that no vibration with wavelength smaller than $2d$ can exist.

In the reciprocal space, the volume of a primitive cell is $(2\pi/L)^3 = 8\pi^3/V$. So the number of states (or number of phonons) with momentum less than or equal to $K = |\vec{k}|$ is equal to the volume of the sphere in the momentum space with radius K divided by the volume of a primitive cell in the reciprocal space. In other words

$$\mathcal{N}(K) = \frac{\frac{4}{3}\pi K^3}{\frac{8\pi^3}{V}}, \quad (2.49)$$

for each polarization.

In terms of the energy of the phonon, the number of states is given by

$$\mathcal{N}(\varepsilon) = \frac{\frac{4}{3}\pi \left(\frac{\varepsilon}{\hbar c_s}\right)^3}{\frac{8\pi^3}{V}} = \frac{V}{2\pi^2} \left(\frac{\varepsilon}{\hbar c_s}\right)^3. \quad (2.50)$$

The density of states is given by

$$\mathcal{D}(\varepsilon) = 3 \frac{d\mathcal{N}(\varepsilon)}{d\varepsilon} = \frac{3V}{2\pi^2} \frac{\varepsilon^2}{\hbar^3 c_s^3}, \quad (2.51)$$

where the factor 3 takes into account the three different polarizations.

Since we are restricted to the first Brillouin zone, we must have a cutoff energy for the phonons, which means that no phonon with an energy up to a certain energy ε_D should exist. From equation (2.50) we find that such energy is

$$\varepsilon_D = \hbar c_s \left(\frac{6\pi^2 N}{V}\right)^{1/3}, \quad (2.52)$$

where N is the number of phonons in one polarization, so the total number of phonons in the system is $3N$.

The total energy of the system can be calculated as

$$U = \int_0^{\varepsilon_D} \varepsilon f(\varepsilon) \mathcal{D}(\varepsilon) d\varepsilon, \quad (2.53)$$

where $f(\varepsilon)$ is the Planck's distribution

$$f(\varepsilon) = \frac{1}{\exp(\varepsilon/k_B T) - 1}. \quad (2.54)$$

So, the total energy of the system is

$$U = \frac{3V}{2\pi^2 \hbar^3 c_s^3} \int_0^{\varepsilon_D} \frac{\varepsilon^3}{\exp(\varepsilon/k_B T) - 1} d\varepsilon. \quad (2.55)$$

We now define the quantity $\xi_D = \varepsilon_D/k_B T = \theta_D/T$, where $\theta_D = \varepsilon_D/k_B$ is the so called *Debye temperature*. Using these definitions, we can rewrite the expression for the energy as

$$U = 9Nk_B T \left(\frac{T}{\theta_D}\right)^3 \int_0^{\xi_D} \frac{\xi^3}{\exp(\xi) - 1} d\xi. \quad (2.56)$$

Differentiating U with respect to the temperature gives us the expression of the heat capacity of the system as

$$C_{ph}(T) = 9R \left(\frac{T}{\theta_D}\right)^3 \int_0^{\xi_D} \frac{\xi^4 \exp(\xi)}{(\exp(\xi) - 1)^2} d\xi, \quad (2.57)$$

where $R = Nk_B$ is the gas constant.

2.6.2 Magnetic contribution to the heat capacity

In our studies, another important contribution to the heat capacity comes from the magnetic excitations (magnons). In this section we discuss this contribution based in a semiclassical approach frequently presented in literature [71, 73].

For sake of simplicity let us consider an isotropic and one-dimensional system with antiferromagnetic nearest-neighbour interactions described by

$$\mathcal{H} = J \sum_j \mathbf{S}_j \mathbf{S}_{j+1}. \quad (2.58)$$

In a semiclassical approach, the spin dynamics is expressed as

$$\hbar \frac{d\mathbf{S}_j}{dt} = \boldsymbol{\mu}_j \times \mathbf{B}_j, \quad (2.59)$$

where $\boldsymbol{\mu}_j = -g\mu_B \mathbf{S}_j$ is the magnetic moment at the j -th site and

$$\mathbf{B}_j = \frac{J}{g\mu_B} (\mathbf{S}_{j-1} + \mathbf{S}_{j+1}), \quad (2.60)$$

is the effective magnetic field at the j -th site generated by the surrounding spins.

So, equation (2.59) can be written as

$$\frac{d\mathbf{S}_j}{dt} = \frac{J}{\hbar} (\mathbf{S}_j \times \mathbf{S}_{j-1} + \mathbf{S}_j \times \mathbf{S}_{j+1}). \quad (2.61)$$

For each cartesian component of the spin we have

$$\frac{dS_j^x}{dt} = \frac{J}{\hbar} \left[S_j^z (S_{j-1}^y + S_{j+1}^y) - S_j^y (S_{j-1}^z + S_{j+1}^z) \right], \quad (2.62a)$$

$$\frac{dS_j^y}{dt} = \frac{J}{\hbar} \left[S_j^x (S_{j-1}^z + S_{j+1}^z) - S_j^z (S_{j-1}^x + S_{j+1}^x) \right], \quad (2.62b)$$

$$\frac{dS_j^z}{dt} = \frac{J}{\hbar} \left[S_j^y (S_{j-1}^x + S_{j+1}^x) - S_j^x (S_{j-1}^y + S_{j+1}^y) \right]. \quad (2.62c)$$

We now consider that the spins are aligned along the z -axis and that $S^z = S$. If the amplitude of the oscillations are small, we can write the previous set of equations as

$$\frac{dS_j^x}{dt} = -\frac{JS}{\hbar} \left[2S_j^y - S_{j-1}^y - S_{j+1}^y \right], \quad (2.63a)$$

$$\frac{dS_j^y}{dt} = \frac{JS}{\hbar} \left[2S_j^x - S_{j-1}^x - S_{j+1}^x \right], \quad (2.63b)$$

$$\frac{dS_j^z}{dt} = 0. \quad (2.63c)$$

Until now we made the assumption that all the spins are point along the same direction,

which is true for a ferromagnetic system. For an antiferromagnetic system, we should consider that the system consists in two sublattices A and B with all the spins in A pointing up along the z -axis and in B all the spins are pointing down along the z -axis.

So, for the antiferromagnetic case, the set of equations (2.63) splits into the following two set of equations

$$\frac{dS_{2j}^x}{dt} = \frac{JS}{\hbar} \left[2S_{2j}^y + S_{2j-1}^y + S_{2j+1}^y \right], \quad (2.64a)$$

$$\frac{dS_{2j}^y}{dt} = -\frac{JS}{\hbar} \left[2S_{2j}^x + S_{2j-1}^x + S_{2j+1}^x \right], \quad (2.64b)$$

and

$$\frac{dS_{2j+1}^x}{dt} = -\frac{JS}{\hbar} \left[2S_{2j+1}^y + S_{2j}^y + S_{2j+2}^y \right], \quad (2.65a)$$

$$\frac{dS_{2j+1}^y}{dt} = \frac{JS}{\hbar} \left[2S_{2j+1}^x + S_{2j}^x + S_{2j+2}^x \right]. \quad (2.65b)$$

Since $S_j^+ = S_j^x + iS_j^y$, the two set of equations (2.64) and (2.65) can be combined into one set

$$\frac{dS_{2j}^+}{dt} = -\frac{iJS}{\hbar} \left[2S_{2j}^+ + S_{2j-1}^+ + S_{2j+1}^+ \right], \quad (2.66a)$$

$$\frac{dS_{2j+1}^+}{dt} = \frac{iJS}{\hbar} \left[2S_{2j+1}^+ + S_{2j}^+ + S_{2j+2}^+ \right]. \quad (2.66b)$$

We seek for solutions to equations (2.66) in the form of plane wave as

$$S_{2j}^+ = u \exp[i2jka - i\omega t] \quad \text{and} \quad S_{2j+1}^+ = v \exp[i(2j+1)ka - i\omega t], \quad (2.67)$$

where u and v are constants and a is the lattice constant.

The substitution of the these plane wave into equations (2.66) results in

$$u\omega = -\frac{JS}{\hbar} (2u + ve^{-ika} + ve^{ika}), \quad (2.68a)$$

$$v\omega = \frac{JS}{\hbar} (2v + ue^{-ika} + ue^{ika}), \quad (2.68b)$$

whose solution is

$$\omega(k) = \frac{2JS}{\hbar} (1 - \cos^2 ka) = \frac{2JS}{\hbar} |\sin ka|. \quad (2.69)$$

For low energy excitations ($ka \ll 1$) the dispersion relation for magnons in an antiferromagnet is

$$\omega(k) = \frac{2JS}{\hbar} a|k|. \quad (2.70)$$

The generalization of this problem to a three-dimensional space is straightforward, with

the dispersion relation written as

$$\omega(\vec{k}) = \frac{2JS}{\hbar} a |\vec{k}|. \quad (2.71)$$

We notice the similarity of equation (2.71) with the dispersion relation for phonons given in (2.46). This similarity allow us to evaluate the heat capacity for magnons as did in the case for phonons.

Analogously to the total energy for phonons given by equation (2.55), the total energy for magnons is

$$U = \frac{3VJSa}{\pi^2} \int_0^\infty \frac{k^3}{\exp(2JSka/k_B T) - 1} dk. \quad (2.72)$$

Defining $x = 2JSKa/k_B T$, we have

$$U = \frac{3VJSa}{\pi^2} \left(\frac{k_B T}{2JSa} \right)^4 \int_0^\infty \frac{x^3}{\exp(x) - 1} dx. \quad (2.73)$$

The integral in equation (2.73) is equal to $\pi^4/15$. Knowing this result, we can express the total energy as

$$U = \frac{V\pi^2 k_B^4}{48(JSa)^3} T^4, \quad (2.74)$$

and finally, the heat capacity of antiferromagnetic magnons is given by

$$C_{mag} = \frac{dU}{dT} = \frac{V\pi^2 k_B^4}{12(JSa)^3} T^3, \quad (2.75)$$

with the well known T^3 dependence of the heat capacity.

2.6.3 Schottky anomaly

Let's consider a system with a finite set of energy levels E_1, \dots, E_k . So the partition function of this system is expressed as

$$Z = \sum_{i=1}^k e^{-\beta E_i}, \quad (2.76)$$

where $\beta = (k_B T)^{-1}$.

From the expressions for the energy

$$U = k_B T^2 \frac{\partial \ln Z}{\partial T}, \quad (2.77)$$

and for the heat capacity,

$$C = \frac{\partial U}{\partial T}, \quad (2.78)$$

is easy to show that

$$C = \frac{N}{k_B T^2} \frac{1}{Z^2} \left[Z \sum_{i=1}^k E_i^2 e^{-\beta E_i} - \left(\sum_{i=1}^k E_i e^{-\beta E_i} \right)^2 \right], \quad (2.79)$$

where N is the number of constituents of the system.

From the expression above we see that in both limits $\beta \rightarrow 0$ and $\beta \rightarrow \infty$ we have $C \rightarrow 0$, with a broad maximum for a finite temperature. This behavior is known as *Schottky anomaly* and it is characteristic of system with finite set of energy [74].

2.6.4 Entropy

In terms of the heat capacity, the entropy of a system between $T = 0$ to $T = T_F$ can be calculated as [68]

$$S(T_F) = \int_0^{T_F} \frac{C(T)}{T} dT. \quad (2.80)$$

From measurements of heat capacity combined with this expression we can calculate the magnetic entropy in our systems. From statistical mechanics we learn that the entropy of a system with equiprobable microscopic configurations (microstates) is temperature independent and equal to the Boltzmann constant times the logarithm of the number of the microscopic configurations that this system can access [74]. So

$$S = k_B \ln \Omega, \quad (2.81)$$

where Ω is the number of microscopic configurations of the system. For a single magnetic dipole with spin S the number of possible spin configurations is $(2S + 1)$. If we consider an ideal paramagnet consisting in a collection of N particle the total number of configurations in this system is $\Omega = (2S + 1)^N$. So, for such system, the entropy is given by

$$S = R \ln(2S + 1), \quad (2.82)$$

where $R = k_B N$ is the gas constant. This result is particularly useful when analysing the entropy of magnetic systems in the limit of high temperatures, since in such situation the thermal fluctuations may overcome the interactions among the spins and, in some approximations, the system can be regarded as an ideal paramagnet. So, if the entropy of the system as a function of the temperature tends to the constant value given by 2.82, the ideal paramagnet approximation is valid. Otherwise, it is an indicative that some interactions in the system are not negligible in such temperatures.

2.7 Quantum Monte-Carlo and the Stochastic Series Expansion method

In order to corroborate some of our experimental results we performed Quantum Monte-Carlo (QMC) calculations to evaluate thermodynamic properties such as magnetization, magnetic susceptibility and specific heat. We used a QMC package provided by the Algorithms and Libraries for Physics Simulations (ALPS) project which, for the Heisenberg spin hamiltonian, makes use of the Stochastic Series Expansion (SSE) method to determine the thermodynamic properties of the system [75].

The SSE method is one of the most used and efficient QMC methods for simulations with spin hamiltonians, allowing the inclusion of further terms such as phonon degrees of freedom. It is based in a series expansion of the partition function as [76]

$$Z = \text{Tr} \left(e^{-\beta \hat{\mathcal{H}}} \right) = \sum_{\alpha} \sum_{n=0}^{\infty} \frac{(-\beta)^n}{n!} \langle \alpha | \mathcal{H}^n | \alpha \rangle, \quad (2.83)$$

where $|\alpha\rangle$ is a basis of \mathcal{H}

Now we write the hamiltonian \mathcal{H} as a sum of operators

$$\mathcal{H} = \sum_{b=1}^M \mathcal{H}_b. \quad (2.84)$$

In a practical example \mathcal{H}_b can be the either diagonal or the non-diagonal parts of the hamiltonian or can designate different sublattices.

Now let us expand \mathcal{H}^n as a sum over all the possible product configurations of \mathcal{H}_b and introduce the index S_n to designate a sequence of products of \mathcal{H}_b . In this way we can rewrite (2.83) as

$$Z = \sum_{\alpha} \sum_{n=0}^{\infty} \sum_{S_n} \frac{(-\beta)^n}{n!} \left\langle \alpha \left| \prod_{i=1}^n \mathcal{H}_{b_i} \right| \alpha \right\rangle = \sum_{\alpha} \sum_{n=0}^{\infty} \sum_{S_n} W(\alpha, S_n), \quad (2.85)$$

where we define the weight

$$W(\alpha, S_n) = \frac{(-\beta)^n}{n!} \left\langle \alpha \left| \prod_{i=1}^n \mathcal{H}_{b_i} \right| \alpha \right\rangle, \quad (2.86)$$

From the expression of the weight we can write the expected value of an operator \hat{A} as

$$\langle \hat{A} \rangle = \frac{\sum_{\alpha} \sum_{n=0}^{\infty} \sum_{S_n} A(\alpha, S_n) W(\alpha, S_n)}{\sum_{\alpha} \sum_{n=0}^{\infty} \sum_{S_n} W(\alpha, S_n)}. \quad (2.87)$$

In the Monte-Carlo method, two successive configurations (α', S'_n) and (α, S_n) are

generated. Then, the ratio R between the respective weights is evaluated as

$$R = \frac{W(\alpha', S'_n)}{W(\alpha, S_n)}. \quad (2.88)$$

and this is related to the probability of accepting or not a new configuration.

Equations (2.85)-(2.88) are the main point of the formalism for the SSE method. Of course it is a much more complex problem, having a number of important points, simplifications and further considerations. However, going through these points is beyond the scope of this thesis. Some good texts that go properly deeper in this technique can be found in references [67, 76–78].

For a ferromagnetic system, the simulation of the problem is straightforward. However, if we deal with a system with antiferromagnetic interactions, in principle we should expect the hindrance of the so-called *sign problem*, related to the minus sign that emerge from the permutation of two fermions. This problem causes an exponential growth of the statistical errors and so the non-convergence of numerical results [78].

In some cases we can overcome this problem by simple algebraic operations, as for an antiferromagnetic system where we can define a simple unitary transformation such that $S_i^+ \rightarrow -S_i^+$, $S_i^- \rightarrow -S_i^-$ with S_i^z remaining unchanged. This transformation does not change neither the commutation relations nor the spectrum of the problem but allow us to avoid the sign problem [67].

Chapter 3

Samples: Crystal structure, preparation and characterization

In this chapter we describe the crystal structure, synthesis and the characterization of the samples by using the X-Ray diffractometry (XRD) and X-Ray fluorescence (XRF) techniques. We begin discussing the crystal structure of the compounds used in this work. After, we describe the method for the synthesis of the samples, which is known as *the method of supersaturated solution*. Then, a description of the preparation of the samples is presented. The results from the XRD, analyzed through the method of Rietveld refinement, are shown as well as its confirmation that the samples produced are the ones expected. Finally, the results from XRF, which allowed us to determine the concentration of Br dopant in our samples, are presented.

3.1 Crystal structure of the compounds

The compound $\text{NiCl}_2\text{-4SC}(\text{NH}_2)_2$, named *dichlorotetrakisithioureanickel* (DTN), forms a body-centered structure with a tetragonal symmetry and belongs to the spacial group I4 [79]. The orientation of DTN crystals is easy to determine since the samples are in general more elongated in the *c*-axis. Also, once the crystal is consisted of chains of DTN molecules lined up along the *c*-axis and due to the non-isotropic geometry of DTN molecule it is expected that DTN samples have different index of refraction along different axis. In this way, DTN samples are birefringents [80]. So, when one sample is exposed to visible light and varying the relative angle between the sample and a polarizer, differences in the intensity of light are easily seen, except when the light comes out through the sample in the direction parallel to the *c*-axis, which is the direction of the polarization. This is a simple but efficient method to confirm the orientation of the samples.

In figure 3.1 we present representations of the DTN molecule and the unit cell of DTN crystals.

The crystal structure of $\text{MnCl}_2\text{-4SC}(\text{NH}_2)_2$ (DTM), $\text{FeCl}_2\text{-4SC}(\text{NH}_2)_2$ (DTF), and $\text{CdCl}_2\text{-4SC}(\text{NH}_2)_2$ (DTC) compounds is also tetragonal. They form face-centered structures

and belong to the space group $P 4_2/n Z$ [81–83]. In figure 3.2 we present the representation for the unit cell of these crystals.

DTM, DTF and DTC crystals have a tetragonal bipyramidal shape with the c -axis pointing along the top of the two opposite pyramids. While DTM and DTC crystals are transparent, DTF crystals have a dark-green color when they just grow. However, after some weeks (depending on the size of the crystal) or after few minutes of exposition in temperatures around $80\text{ }^\circ\text{C}$, the crystal turn from dark-green to white. The dark-green color of the crystals is due to the presence of O_2 molecules during the growth process, that are kept trapped in the crystal structure. After some time or through the application of heat, these O_2 molecules leave the crystal structure, turning the color of the crystal into white [84]. The orientation of DTF crystals is also possible to determine due to its birefringence.

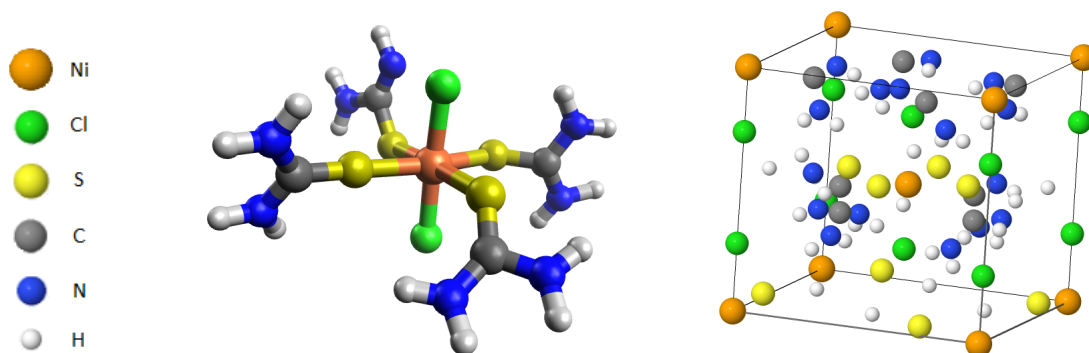


Figure 3.1: Representations of the DTN molecule and the DTN crystal unit cell. The figure of the DTN unit cell was reproduced from ref. [79].

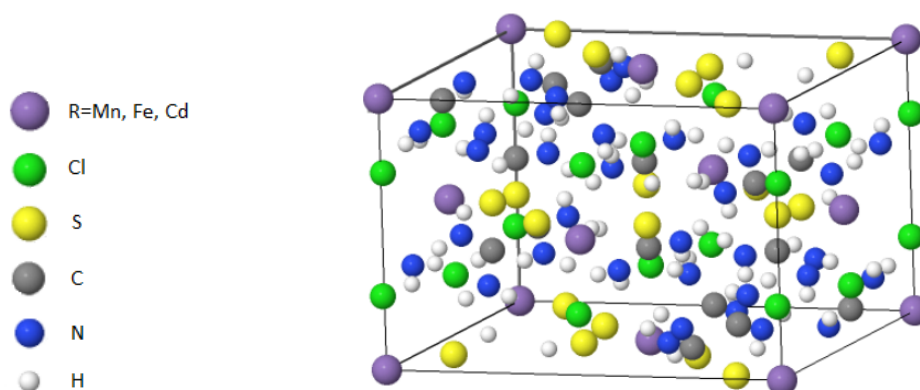


Figure 3.2: Representation of DTM, DTF or DTC crystal unit cell. This figure was reproduced from ref. [81].

3.2 Method of supersaturated solution

The method of supersaturated solution consists in prepare a heated solvent and dissolve in it an amount of solutes above the limit for the saturation in a lower temperature. Once the solution is prepared, it is kept in a thermal bath in a lower (and constant) temperature. Depending on the proportion of the compounds, the volume of the solution, the type of the solvent, the temperatures during the preparation and the unperturbed rest in the thermal bath, crystals are formed in periods from some hours to weeks [85].



Figure 3.3: Thermal bath with some DTN solutions.

3.3 Synthesis of the samples

3.3.1 DTN

Typical DTN samples used in this work were prepared by adding 20 g of $\text{NiCl}_2 \cdot 6\text{H}_2\text{O}$ and 5.5 g of $\text{CS}(\text{NH}_2)_2$ (thiourea) in 75 ml of distilled water at $100\text{ }^\circ\text{C}$ ¹. The solution is stirred during 1 hour and then filtered. Around 3 ml of HCl is added, once it was noted that the reduction of pH in the solution increases the time of the growth of the samples and then improving their quality. After, the solution is left in the heater at $100\text{ }^\circ\text{C}$ to evaporate until reach a volume of approximately 50 ml. Finally the solution is capped, allowing just a small aperture to promote a slow evaporation, and inserted in a thermal bath at $35\text{ }^\circ\text{C}$. In a period of a couple of days, DTN crystals are formed in the bottom of the becker. Some DTN samples are shown in figure 3.4.

¹All the chemical compounds used in this work have a high level of purity ($\geq 99.0\%$) and were obtained from commercial sources.



Figure 3.4: DTN samples of different sizes produced from the method of supersaturated solution. All the samples in the figure were align with the *c*-axis pointing vertically according to the red arrow.

3.3.2 DTM and DTC

DTM and DTC samples are produced in the same way of DTN. For DTM, the proportion of the chemical compounds are 25 g of $\text{MnCl}_2 \cdot 4\text{H}_2\text{O}$ and 9 g of thiourea, the same proportion presented in ref. [86,87]. DTC crystals are made by mixing 1.5 g of $\text{CdCl}_2 \cdot 2 \frac{1}{2} \text{H}_2\text{O}$ and 4.5 g of thiourea, according to ref. [88]. For both samples, the solutes are mixed in 75 ml of distilled water at 100 °C, stirred during 1 hour and then filtered. For these samples we realized that there are no need to add HCl, since they grow very slowly and regularly. The solutions are partially capped when their volume is around 50 ml to promote the slow evaporation in a thermal bath at 35 °C. In the period between one to two weeks, transparent crystals are formed.

3.3.3 DTF

The DTF samples are also produced by the supersaturated solution method. However the solvent employed is pure ethanol. For these samples 3 g of $\text{FeCl}_2 \cdot 4\text{H}_2\text{O}$ and 3 g of thiourea was dissolved 100 ml of ethanol, according to the proportion employed in [84,89–91]. The solution was heated to 100 °C and stirred in an erlenmeyer with a separatory funnel attached to its end. In this way, the ethanol that was evaporated from the erlenmeyer enters in the separatory funnel and cools down, condensing and entering again in the erlenmeyer. This procedure is known as *reflux*, where the evaporated solvent is condensed and returns to the solution [92].

After 1 hour the solution is filtered, totally capped and kept in rest in a temperature of 0 °C. After some hours, dark green crystals are formed. However they are collected, in general, after 2 days since it is observed that the crystals do not grow more after this period. This crystals have a bipyramidal shape and maximum size around $3 \times 3 \times 3$ mm.

3.3.4 DTN-Br

The preparation of DTN samples with Br doping follows the same procedure as the pure DTN samples. The difference is the addition of HBr-40% in the solution containing $\text{NiCl}_2 \cdot 6\text{H}_2\text{O}$ and thiourea. Different percentages of Br in the samples requires different proportion of the solutes. To the preparation of these samples we choose to keep the amount of $\text{NiCl}_2 \cdot 6\text{H}_2\text{O}$ as 20g in the solution and vary the amount of thiourea and HBr.

To determine the percentage of Br in each sample we performed XRF analysis, which is discussed in section 3.5 of this thesis.

3.4 XRD characterization and Rietveld refinement

In order to characterize our samples, we perform some XRD measurements from the sample powder using a commercial X-ray Bruker-D8 Advance diffractometer in 2-theta configuration [93]. The diffractogram was analyzed through the method of Rietveld refinement.

The Rietveld refinement is based in a least-square method that fits a function to the peaks of a diffractogram. Among several functions that can be fitted, the most used (and the one used in this work), due to the good results provided, is the *pseudo-Voigt* function, which consists in a convolution between a gaussian and a lorentzian functions [94],

$$V(x, \sigma, \alpha) = \int_{-\infty}^{\infty} G(x', \sigma)L(x - x', \alpha)dx', \quad (3.1)$$

where

$$G(x, \sigma) = \frac{e^{-x^2/(2\sigma^2)}}{\sigma\sqrt{2\pi}} \quad \text{and} \quad L(x, \sigma) = \frac{\alpha^2}{(x^2 + \alpha^2)}, \quad (3.2)$$

are, respectively, the gaussian and the lorentzian functions.

From the fit of the pseudo-Voigt function by varying the several parameters presents in the model it is possible to extract informations such as the the lattice parameters, thermal exponents, existence of additional phases of the material, and many other properties. This fit is in general made by some Rietveld refinement software. In this work we made use of the *Fullprof* software [95].

The diffractograms presented in figure 3.5 correspond to the measured and refined spectra for our samples. As we see, there is a good agreement between the measurement and the adjust by the Rietveld refinement for all samples, which points that our samples are the ones expected without any additional phase.

In the table 3.1 we summarize the results for the lattice parameters obtained by the refinement with those from the literature [79, 81–83]. It is important to mention that, for each compound studied in this work, the lattice parameters a , b and c correspond to the distance between two consecutive magnetic ions along the a , b and c -axis respectively.

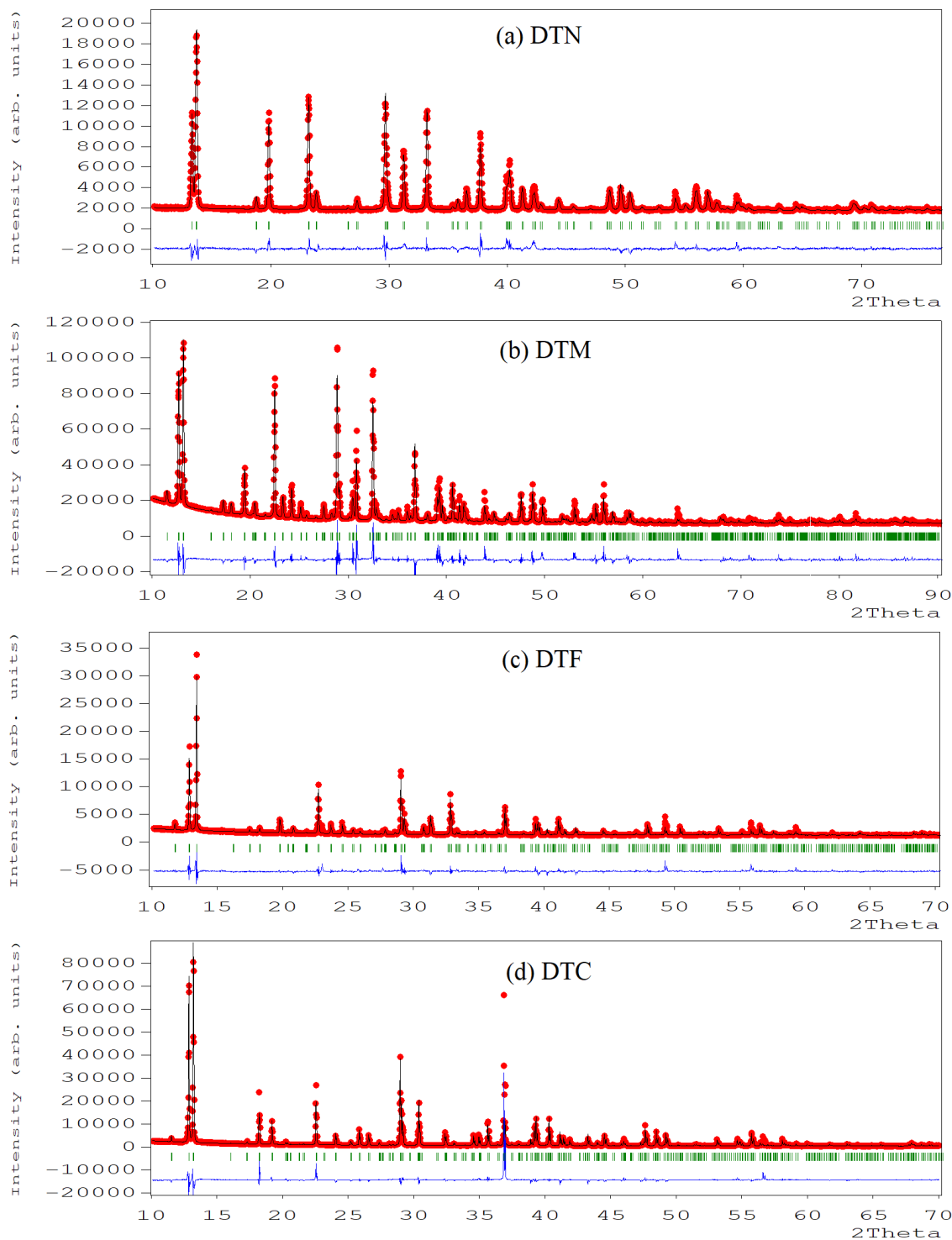


Figure 3.5: Rietveld refinement of (a) DTN, (b) DTM, (c) DTF and (d) DTC. The red dots are obtained in the XRD measurements. The black curve is the adjust of the refinement, the blue curve is the error between the XRD data and the adjust and the green tics point out the position of the peaks.

Table 3.1: Comparison between the lattice parameters (in Angstroms) from the refinement and literature.

Sample	$a = b$ (refined)	$a = b$ (literature)	c (refined)	c (literature)
DTN	9.559	9.599	8.974	9.082
DTF	13.708	13.710	8.943	8.940
DTM	13.760	13.753	9.066	9.079
DTC	13.804	13.804	9.267	9.268

3.5 X-ray Fluorescence

In the X-ray Fluorescence (XRF) a photon with a certain amount of energy ionizes the K shell of an atom. This process generates a vacancy in the K shell, that is filled by an atom in an outer shell, such as L or M shells. Consequently, the transition of an electron from the L or M shell to the K shell results in the emission of a X-ray photon.

The principle of XRF technique consists in measuring the energy and intensity of photons emitted by a sample. Since each element has distinct energy levels one from another, the energy of a photon emitted by fluorescence is characteristic of each element. In this way, the XRF technique allows the determination of the composition of a certain material through the detection of photons emitted from fluorescence [96].

In this technique, photons from the $L \rightarrow K$ transition, also known as K_α emission, are predominant during the detection. Photons from the $M \rightarrow K$ transition, known as K_β emission, are also detected with a reasonable resolution.

A XRF spectrometer consists, basically, in a X-ray source and detector. The X-ray source is a vacuum tube where an electron beam is accelerated by a potential difference of the order of kV. The beam collides on a target and so the electrons stop abruptly. This slow down process generates a continuous spectrum of radiation and it is called *Bremsstrahlung* (from German, *bremsen* “to brake”, and *Strahlung* “radiation”).

In this work, the detector used was a XR-100 Silicon Drift Detector (SDD) by Amptec [97]. In this solid state detector, the incoming photon ionizes the atoms from the crystalline lattice, generating an electric current measured by an electronic circuit. Figure 3.6 shows the setup of X-ray source and detector used in this work.

3.5.1 Analysis

The first XRF measurement performed was the analysis of the paper used as a sample holder in the experimental setup. This analysis was made in order to characterize the elements from the sample holder that could, eventually, introduce errors in the sample measurements. Figure 3.7 shows the XRF spectra for the sample holder.

In figure 3.7 two sharp peaks in the spectrum can be seen. The energies correspondent to these two peaks, in 2.95 keV and 3.17 keV, are respectively those for the K_α and K_β transitions for the argon, since this element is present in the air.



Figure 3.6: XRF setup used in this work with the X-ray source (on the left) and the X-ray detector (on the right).

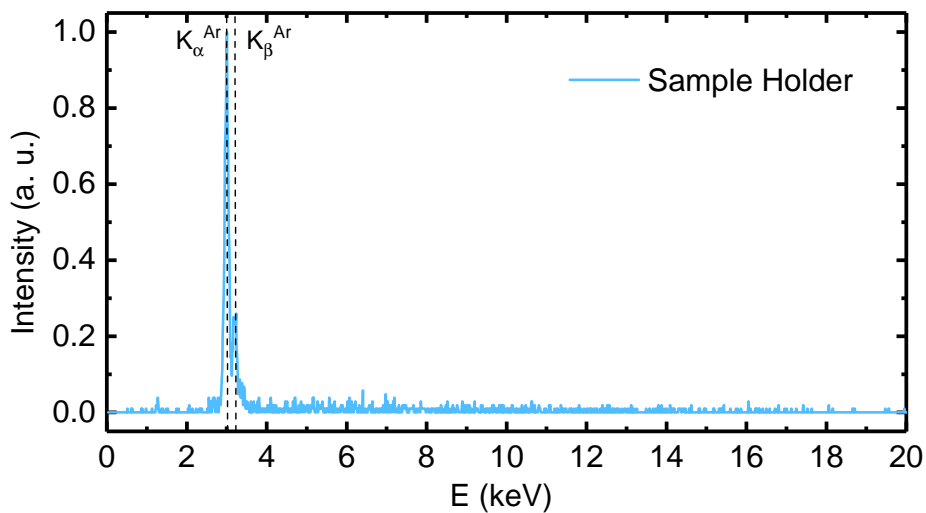


Figure 3.7: XRF spectra for the paper used as the sample holder. Dashed lines mark denote the position of the K_{α} and K_{β} transitions of argon [98].

After the sample holder characterization, we started the analysis for the pure DTN and DTN-Br samples. In figure 3.8 we present our results from the XRF measurements for the Br-doped DTN samples.

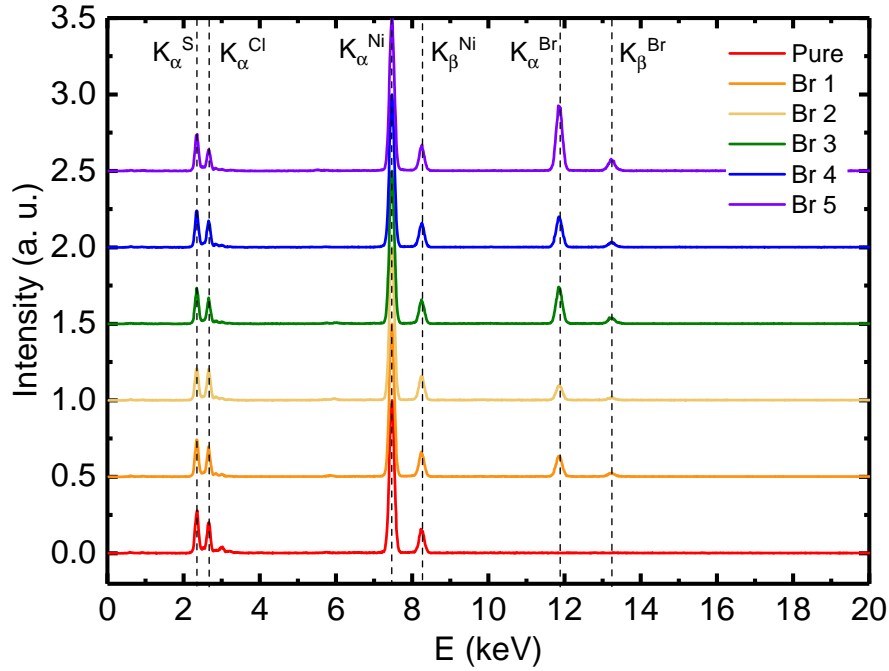


Figure 3.8: XRF spectra for Br-doped DTN samples. Dashed lines mark denote the position of the K_{α} and K_{β} transitions of each element [98].

For the pure DTN and for each DTN-Br batch 3 samples were analyzed in order to check the reproducibility of the results and verify if for a single batch samples with different Br concentration were grown. However no appreciable differences were seen in the XRF spectra between samples from the same batch, indicating the good reproducibility of our XRF measurements and the homogeneity of the solutions during the synthesis of the samples.

To obtain relative the percentage of bromine in our samples we apply the following procedure. First we normalize the intensity of K_{α} peak for the nickel atoms to 1 for all measurements. Since we know that in pure DTN the proportion of nickel and chlorine atoms are 1:2 we use this normalization to have a reference for the height of K_{α} peak for chlorine and bromine. Once the amount of any element in the sample is directly proportional to the intensity of the peak and knowing the height of the K_{α} peaks for chlorine and bromine in each sample, the determination of the relative Br and Cl concentration of each sample is straightforward.

From the analysis of chlorine K_{α} peaks we should be able to extract the absolute concentration of chlorine and, consequently, bromine in the samples. However, due to the low K_{α} peak height for chlorine, not so pronounced as for bromine, determining the chlorine absolute concentration may lead to non-trustworthy results. So a more precise estimation for the halogen concentrations in the samples is given by analysing the K_{α} peaks for bromine. From this we were able to determine only the relative bromine concentration in the samples since we had no sample with a known bromine concentration. In order to have a reference sample and so obtain the absolute value of such concentrations, we analysed some samples by the chemical analytical method of Schöniger oxidation, in Instituto de

Química in Universidade de São Paulo. Knowing the absolute concentration of, at least, one sample we were able to estimate the absolute concentration of all samples using the relative concentrations obtained from XRF measurements.

Another alternative to obtain the absolute concentration of chlorine and bromine in our samples would be analysing them through XRD and Rietveld refinement. We performed such analysis but the results were elusive since no appreciable difference for the lattice parameters and bromine concentration was observed among the samples analysed. Our hypothesis is that bromine concentrations in the sample are small and such differences from one sample to the other are hardly observable. For higher concentrations these differences may be more pronounced.

The results of our analysis are summarized in table 3.2.

Table 3.2: Br-doping percentage for different batches of DTN-Br samples according to the XRF analysis.

Sample batch	NiCl ₂ ·6H ₂ O (g)	Thiourea (g)	HBr (g)	% Br
DTN-Br1	20	8	8	4.8
DTN-Br2	20	4	4	3.3
DTN-Br3	20	15	15	8.8
DTN-Br4	20	9	12	7.0
DTN-Br5	20	8.4	13	15.5

Chapter 4

Experimental techniques

In this chapter we present the instruments used in the measurements to study the magnetic properties and specific heat of our samples. Initially we discuss the commercial SQUID device used to perform magnetization and AC susceptibility measurements. Then we describe the multi-platform device employed to take specific heat measurements. Also, we present the cryostat in which we performed measurements of AC magnetic susceptibility and magnetization using a VSM in lower temperatures and higher magnetic fields than that the commercial SQUID device can achieve. Finally, we discuss the Adiabatic Demagnetization Refrigeration (ADR) technique used in one of our cryostats for AC magnetic susceptibility measurements.

4.1 MPMS SQUID magnetometer

The Magnetic Property Measurement System (MPMS) is a commercial SQUID magnetometer used to perform magnetization and AC magnetic susceptibility measurements. This device works in a temperature range from 1.8 K to 400 K and has a 7 T superconducting magnet, which allows to study the magnetic properties of samples under high external magnetic field. MPMS is connected to a personal computer which makes possible to execute automatized experiments.

SQUID is an acronym for (Superconducting QUantum Interference Device). These devices are very sensitive magnetometers, being used for many applications. The operation principle is based on the flux quantization in superconducting loops and in weak links on superconductor junctions, which originate the so-called *Josephson Effect*, named after B. D. Josephson.

A well known fact is that the total magnetic flux passing through a superconductor loop is quantized in the form [71, 99]

$$\Phi = \frac{h}{2e}s = \Phi_0 s, \quad (4.1)$$

where h is the Planck constant, e is the electron charge and s an integer. The quantity

$\Phi_0 = h/2e = 2.07 \times 10^{-15} \text{ Tm}^2$ is called *flux quantum* [99].



Figure 4.1: MPMS Model XL-7 SQUID magnetometer by Quantum Design used in our measurements.

Now let us consider two pieces of superconductors separated by a thin (around 10 \AA) insulating layer. This configuration is called *Josephson Junction*. Due to the small thickness of this layer, Cooper pairs are able to tunnelling from one superconductor piece to another. Josephson showed that the current flowing from these superconductor junction is given by [100]

$$I = I_0 \sin \delta, \quad (4.2)$$

where $\delta = \theta_2 - \theta_1$ phase difference between the Cooper pairs wavefunctions in both sides of the junction and I_0 is proportional to the density of Cooper pairs [99].

The next step to understand the SQUID basic principles is to consider two Josephson junctions in parallel, as in figure 4.2.

When a magnetic flux passes through this circuit, the currents in the junctions are given by [71]

$$I_a = I_0 \sin \left(\delta_0 + \frac{e}{\hbar} \Phi \right) \quad \text{and} \quad I_b = I_0 \sin \left(\delta_0 - \frac{e}{\hbar} \Phi \right), \quad (4.3)$$

where $\delta_0 = \delta_b - \delta_a$ and δ_a (or δ_b) is the phase difference between the both sides of the *a* (or *b*) junction.

So the total current in the circuit is

$$I = I_a + I_b = I_0 \left[\sin \left(\delta_0 + \frac{e}{\hbar} \Phi \right) + \sin \left(\delta_0 - \frac{e}{\hbar} \Phi \right) \right] = 2I_0 \sin(\delta_0) \cos \left(\frac{e}{\hbar} \Phi \right). \quad (4.4)$$

This expression is the basis of the quantum interference device that is known as a SQUID.

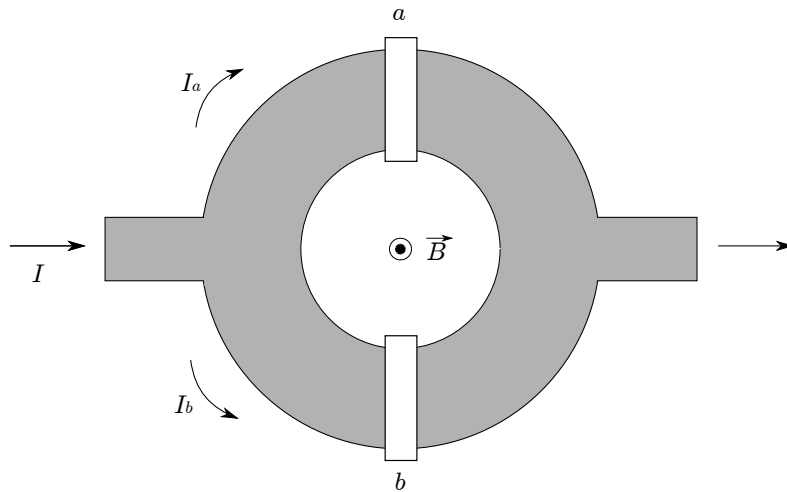


Figure 4.2: Two Josephson junctions in parallel. These junctions are formed by superconductors separated by two insulators a and b . I_a and I_b are the currents passing through the a and b branches of the loop and \vec{B} is an external magnetic field applied to the loop.

In a SQUID magnetometer, a superconductor loop with Josephson junctions, as sketched in figure 4.2, is coupled to the inductive system of detection, consisting in a assembly with pick-up coils (see figure 4.3). Small variations of the magnetic field in the pick-up coils due to the extraction magnetization or AC field from a primary coil, produces measurable changes in the voltage V of the superconducting loop, that are translated by the MPMS software into magnetic units.

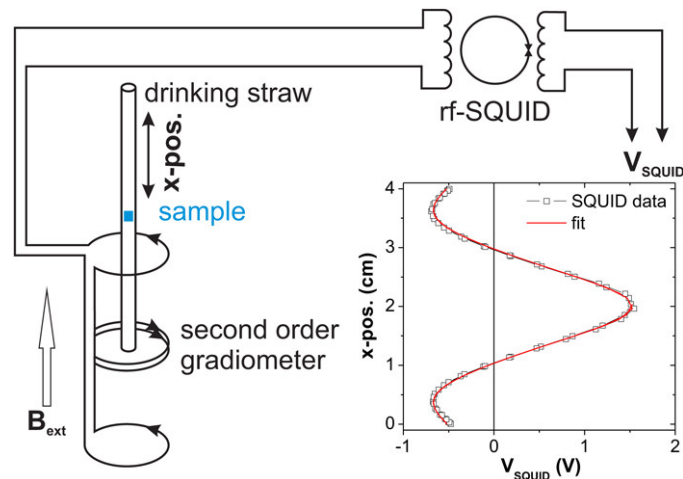


Figure 4.3: Schematic representation of the SQUID circuitry. The straw with a sample inside is inserted and further extracted from the pick-up coils, here called second order gradiometer and sometimes also second derivative detector array [101]. Inset: Voltage signal measured during the extraction of the sample from the pick-up coils. Figure reproduced from [102].

4.2 PPMS

The Physical Property Measurement System (PPMS) is a commercial platform to perform a variety of measurements, such as heat capacity, transport phenomena, optics, and many others, in low temperatures and high magnetic fields. The temperature range of operation is from 1.8 K to 400 K and a 9 T superconducting magnet provides the external magnetic field to the measurements. Also, with our PPMS there is an insert coupled to a dilution refrigerator (DR) which makes possible to perform experiments down to 50mK. PPMS also is connected to a personal computer and it is able to automatically run experiments in the same way as the MPMS does.

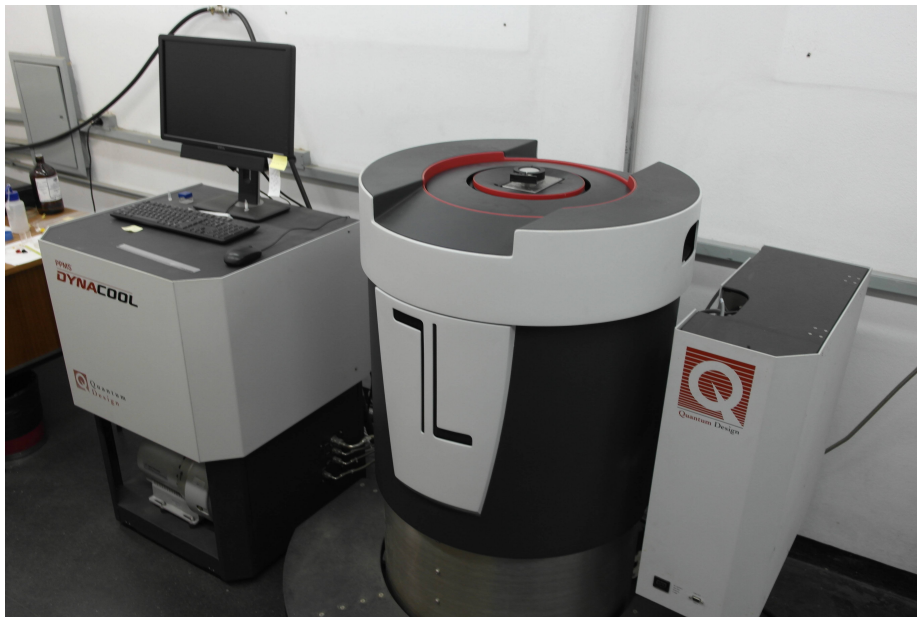


Figure 4.4: Physical Property Measurement System (PPMS) platform by Quantum Design.

4.2.1 Specific heat measurements

Specific heat measurements are performed in a puck, consisting in a metallic frame which supports in the middle of it a small sapphire platform suspended by eight thin gold wires. In this way, the platform is nearly thermally isolated from the environment. The platform has in one edge a heater and in the opposite edge a thermometer. The eight gold wires also provided the electric current needed by the heater and the thermometer. The sample is placed in the middle of the platform and it is fixed by Apiezon grease. This assembly is shown in figure 4.5.

Under the puck there are electric terminals connected to the gold wires. For the measurements the puck is attached in a rod and guided to the bottom of the PPMS chamber, where the puck terminals are connected to a socket. So then, the puck is connected to the PPMS and ready to perform the experiments.

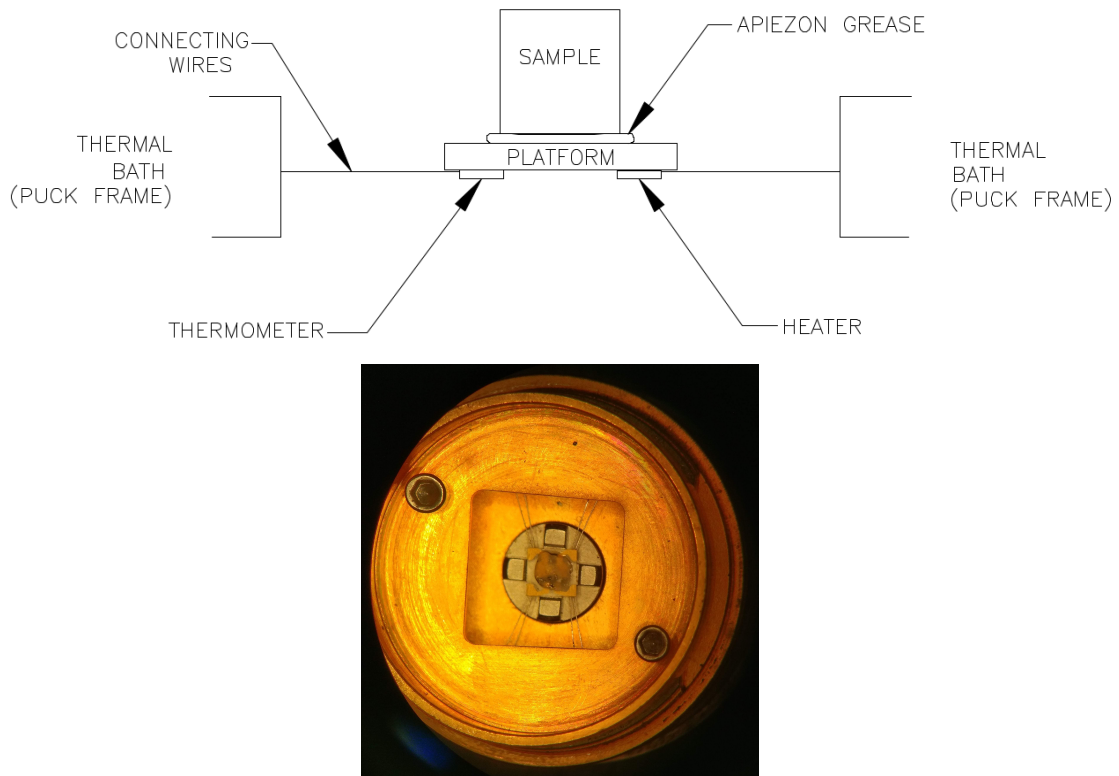


Figure 4.5: Top panel: Schematic representation of the heat capacity puck. This figure was reproduced from ref. [103]. Lower panel: heat capacity puck with a sample.

The measurements are controlled by the PPMS software. Basically, a measurements consists in giving through the heater some well known amount of heat to the system and measure the heat transmitted to the thermometer. The PPMS software, using some mathematical models, fits parameters such as the measured temperature and the power of the heater to calculate the heat capacity.

There are two models used to infer the heat capacity. The first one, *the simple (one-tau) model* considers that the heat capacity is given by,

$$C_{tot} \frac{dT}{dt} = -K_w(T - T_b) + P(t), \quad (4.5)$$

where C_{tot} is the total heat capacity, T is the temperature of the platform, t is the time of the measurement, K_w is the thermal conductance of the wires, T_b is the temperature of the thermal bath (puck frame) and $P(t)$ is the power given by the heater.

The solution of equation 4.5 is expressed as an exponential with a time constant τ . This model considers that there is a very good coupling between the sample and the platform. If the coupling is poorer or the thermal conductance of the sample should be taken into account when, for example, the sample is thick, the software uses the *two-tau model*, expressed as

$$C_p \frac{dT_p}{dt} = P(t) - K_w (T_p(t) - T_b) + K_g (T_s(t) - T_p(t)), \quad (4.6)$$

$$C_s \frac{dT_s}{dt} = -K_g (T_s(t) - T_p(t)), \quad (4.7)$$

where C_p and C_s are, respectively, the heat capacity of the platform and sample, T_p and T_s the temperatures of the platform and sample, and K_g is the thermal conductance between the sample and the platform due to the grease [103].

In this work typical samples measured are approximately 2 mm \times 2 mm wide and less than 1 mm high.

It is worth to mention that before measuring a sample, the amount of Apiezon grease to fix the sample should be measured first. This is called the *addenda measurement*. From this measurement, the software will subtract the contribution of the grease to the heat capacity from the total value when the sample is measured.

4.2.2 Slope analysis

In this work we made two kinds of specific heat measurements. In the first one, each point of the specific heat curve consists is a short pulse, providing a increase of the heat around 2% and followed by its measurement in the thermometer. So the software adjusts the heating and cooling curves to is mathematical model. From this technique it is possible to get specific heat curves in a wide range of temperatures but with a low resolution. The second technique, known as *slope analysis*, consists in applying a large pulse of heat (around 30% of increasing of heat) and then measure the specific heat in this single shot. This allows to get a very detailed curve but in a small range of temperatures. This method is good to study in detail the region where a phase transition occurs [103].

4.2.3 Vibrating Sample Magnetometer (VSM) option

One of the options present in the PPMS is a Vibrating Sample Magnetometer (VSM), which allows to study the magnetic properties of samples.

This device consists in a sample holder rod in which one of its ends hosts the sample to be measured and the other is connected to a source of harmonic vibrations, such as a speaker, linear actuator or a piezoelectric oscillator. An uniform magnetic field H from a superconducting coil is applied to the samples perpendicular to the axis of the oscillations. The response of the sample is measured in a pickup coil set with help of a lock-in amplifier [104, 105].

In figure 4.6 we present a schematic representation of a VSM.

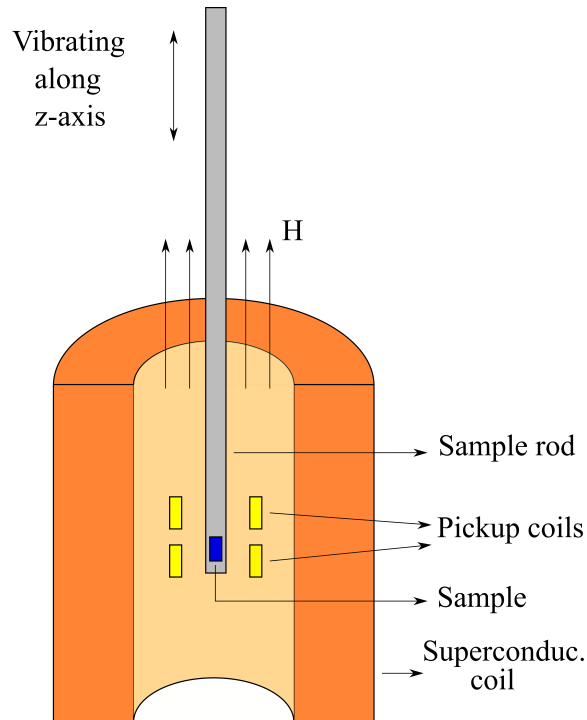


Figure 4.6: Schematic representation of a VSM.

4.2.4 Dilution Refrigerator (DR) option

Currently dilution refrigerators (DR) are one of the most efficient technologies to achieve temperatures from 1 K down to 50 mK, typically. It is based on the properties of liquid ^3He - ^4He mixtures.

According to the phase diagram presented in figure 4.7, a mixture of ^3He and ^4He with at least 6.6% of ^3He goes to a separation of rich- ^3He phase and rich- ^4He for temperatures below 0.87 K. When these phases are cooled down, the rich- ^3He phase becomes even more pure but for the rich- ^4He phase the concentration of ^3He reaches the constant value of 6.6% [106].

For pedagogical purposes, a very simple plot of the working principle of a DR can be depicted if we imagine a U shape tube as illustrated in figure 4.8.

In this assembly, almost pure ^3He is inserted in the left side of the tube. The rest of the tube is filled with the ^3He - ^4He mixture with 6.6% of ^3He . A pump is connected to the right side of the tube to remove the vapour on this side. If the temperature of the mixture is around 0.7 K, most of the vapour will consist in ^3He atoms. When this vapour is pumped out from the system, the amount of ^3He in the mixture is no more of 6.6%. To restore the equilibrium of the concentration, ^3He atoms from the almost pure portion will be transferred to the mixture. In this process, the system is cooled down due to the latent heat of mixing [107].

The example above is quite simplistic, but gives an idea of the working principle of DRs. More detailed descriptions can be found in references [106, 107].

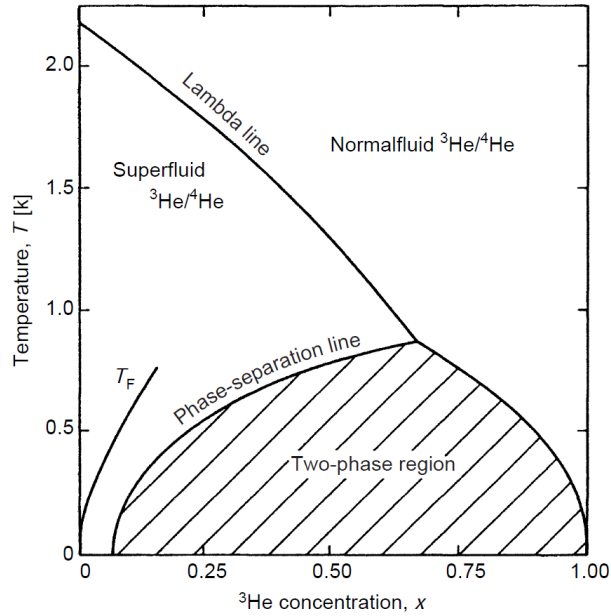


Figure 4.7: Phase diagram of liquid ^3He - ^4He mixture. The lambda line denote transition between the normal phase to the superfluid phase of ^4He . In the two-phase region, the separation of rich- ^3He phase and rich- ^4He occurs. T_F is the fermi temperature of ^3He . Figure adapted from reference [106].

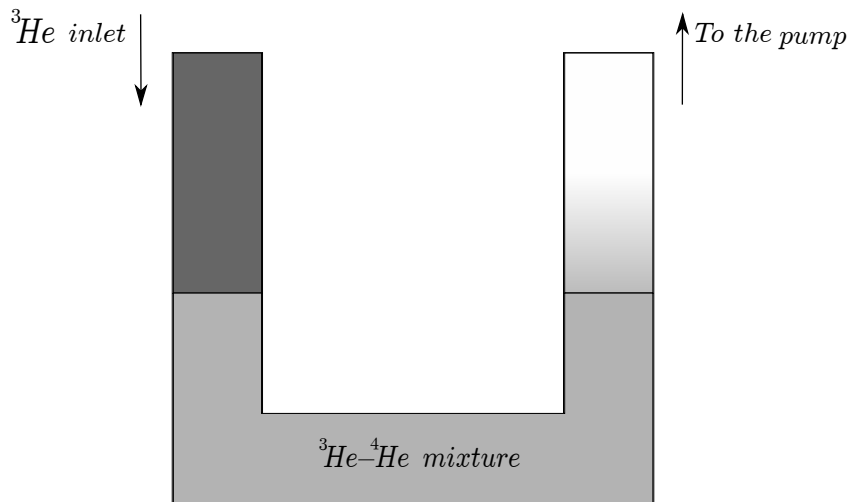


Figure 4.8: Schematic representation of an simplified version of a DR.

In figure 4.9 we show a picture of our DR system with the ^3He - ^4He mixture cylinder and DR insert.

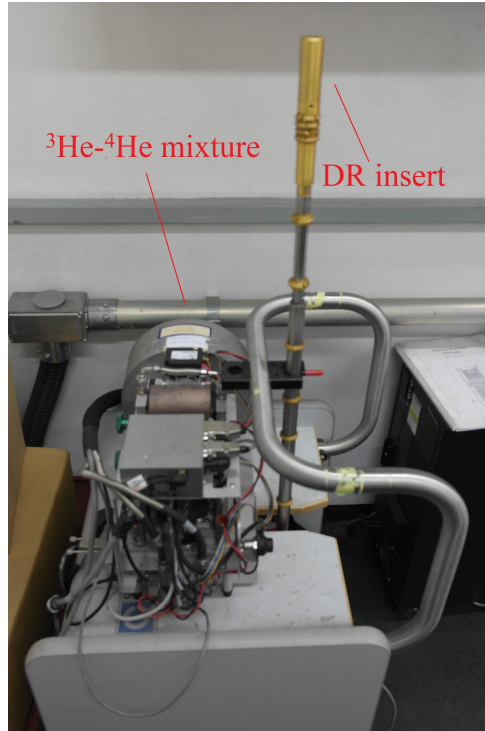


Figure 4.9: PPMS DR assembly with the ^3He - ^4He mixture cylinder and DR insert.

4.3 AC susceptibility and VSM measurements setups

The AC susceptibility and some magnetization measurements are performed in two cryostats, one with a 7.5 T and the other with a 20 T superconducting coil. In these setups it is possible to achieve temperatures down to 1.4 K by pumping condensed ^4He or even cool down to 0.5 K using ^3He . Also, they allow the sample to be immersed in the helium bath, what improves the thermal coupling and favors the sample thermalization.

We perform AC susceptibility measurements using a mutual inductance bridge (see figure 4.11). In this bridge a lock-in amplifier provides to the primary (excitation) coil P a sine wave signal with well defined amplitude and frequency. The pick-up (secondary/detection) coils S are concentric to the primary coil and they consist in two equal coils connected in series but one opposite direction to the other. In this way they cancel each other's signal generated by the primary excitation when there is no sample inside them. They are also connected to the lock-in amplifier, measuring the amplitude and phase of the detected signal. Also this bridge contains a reference toroidal inductance T and a Dekapot potentiometer R_x to balance the resistive component of the signal [108].

Initially the bridge is adjusted from the Dekatran autotransformer D to have a total null inductance. When the sample is inserted and centered in one of the two pick-up coils, it promotes an unbalance of the bridge. The resultant inductance from this unbalance is proportional to the signal of the sample. The lock-in amplifier displays the measured signal as a voltage and provides an output terminal to read this signal in an external voltmeter.

Then, the external voltmeter is connected to a computer via a GPIB connection and a data acquisition software register the result of the measurement.



Figure 4.10: 7.5 T (left) and 20 T (right) cryostats.

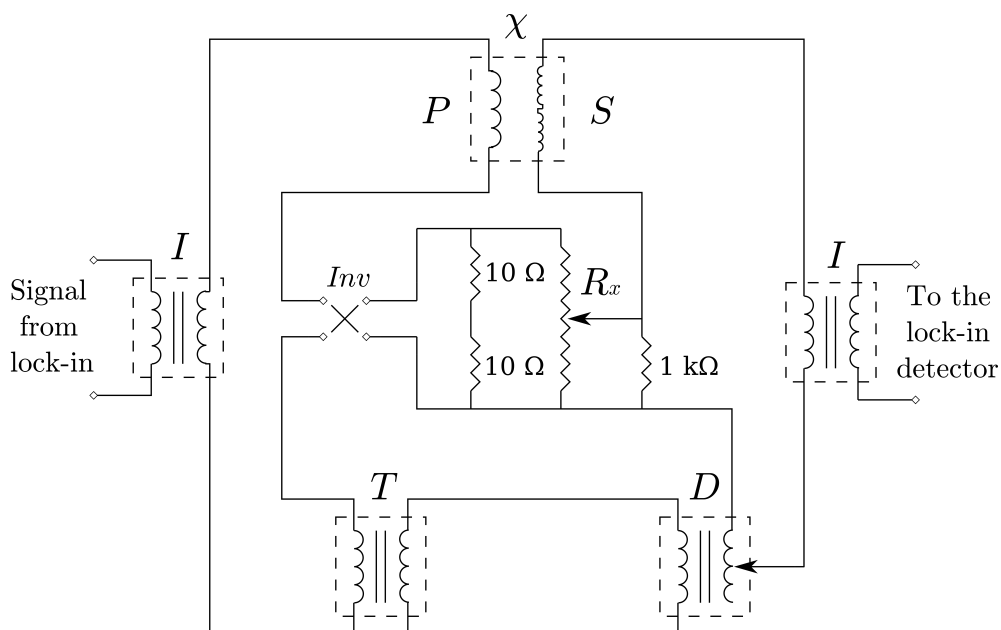


Figure 4.11: Simplified mutual inductance bridge circuit, where a sine wave signal from the lock-in amplifier provides an excitation to the primary coil P . χ is the set with the primary and pick-up (secondary) S coils. The inductive and resistive components of the signal measured in S are respectively balanced by setting the Dekatran autotransformer D and the Dekapot potentiometer R_x . The circuit also contains the toroidal transformer T as a reference inductance to the bridge and two isolation transformers I for the input and the output signals. Inv is a switch that provides the inversion of the sign of the excitation.

In this arrangement we are able to perform measurements of samples with a signal in the order of magnitude of $\sim 10^{-5}$ emu.

We can express the AC magnetic susceptibility χ by $\chi = \chi' + i\chi''$ where $\chi' = \chi \cos \phi$ is the real part of the magnetic susceptibility, $\chi'' = \chi \sin \phi$ is the imaginary component related to dissipative process in the sample and ϕ is phase of the signal relative to the wave signal generated by the lock-in and the measured signal. In the lock-in amplifier it is possible to adjust this phase in order to minimize the χ'' component.

During a measurement, since in this arrangement the absolute value of the magnetic susceptibility is difficult to determine, we just look to the real component χ' without loss of generality. However we always adjust the phase of the signal the best we can in order to minimize the χ'' component and maximize the χ' component.

Coupled to the 20T cryostat we also have a VSM to perform magnetization measurements.

4.4 Adiabatic Demagnetization Refrigeration (ADR)

The technique known as adiabatic demagnetization of a paramagnetic salt is an alternative to dilution refrigerators to reach temperatures of the order of few milikelvin.

The idea behind this technique is the cooling by the reduction of the entropy of a system. From Section 2.6 we saw that the entropy of an ideal paramagnet tends to $S = R \ln(2S + 1)$, where R is the gas constant and $(2S + 1)$ are all possible spin configurations. Let us also consider a paramagnetic salt in which all the contributions to the entropy of the salt (e.g. lattice and electronic entropies) are very small compared to the magnetic disorder entropy.

Of course, when the temperature of the salt is reduced, some magnetic ordering may arise. So the temperature achieved in this cooling process will be limited and comparable to the magnetic ordering temperature.

An example of thermodynamic cycle for the ADR is depicted in figure 4.12. The first step in the ADR is to couple the paramagnetic salt to a liquid ^4He reservoir. By pumping the ^4He vapour, the achieved temperature is around 1 K. Then, an external magnetic field, generally on the order of 0.1 T to 5 T is switched on. In this process, the magnetic moments of the paramagnetic salt will at least partially line up along the direction of the applied field. This reduces the entropy of the system and, since the paramagnetic salt is coupled to the liquid ^4He reservoir this is an isothermal process, as shown by the curve $A - B$ in figure 4.12. The next step is to remove the coupling between the paramagnetic salt with the liquid ^4He reservoir. So in this situation we have the isolated salt with the temperature of the liquid ^4He reservoir but now decoupled from it. Then, the external magnetic field is adiabatically removed and the temperature of the system reduces by an isentropical process (curve $B - C$ in figure 4.12). Finally, when the external magnetic field is nearly zero, the system starts to slowly warm up by heat leaking and the process needs to be restarted if the low temperature achieved is required once more for the experiments [106].

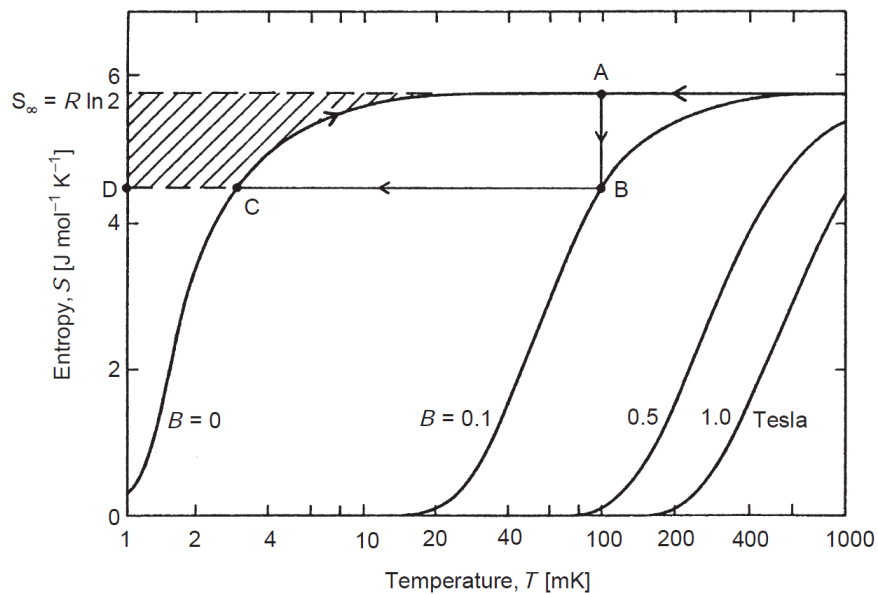


Figure 4.12: An example of thermodynamic cycle for the ADR, showing the entropy of a paramagnetic salt for different external magnetic fields applied. Figure reproduced from reference [106].



Figure 4.13: Cryostat with an ADR system to measurements of AC magnetic susceptibility at zero external magnetic field.

While dilution refrigerators can work in a continuous way, being able to keeping the temperature of the system nearly constant even for days, an adiabatic demagnetization refrigeration is a one-shot process, which means that once the desired temperature is reached, the system is warmed up by heat leaking.

In this work, some measurements of AC magnetic susceptibility at zero external magnetic field were performed in a cryostat with an ADR system by Cambridge Cryogenics, showed in figure 4.13. In this system it is possible to achieve temperatures down to 50 mK.

The measurement of AC magnetic susceptibility in this setup is very similar to the process described in the last section. However this setup has two pick-up coils sets, one of 1 mm bore and the other with 5 mm bore, allowing to host two samples to be measured at the same time.

Chapter 5

Quasi-1D regime in DTN

In this chapter we discuss our results regarding the characterization of a quasi-1D regime in DTN, through AC susceptibility and specific heat measurements, which are compared with our Quantum Monte-Carlo calculations. Initially we give an overview of some examples and features of quasi-1D systems, emphasizing antiferromagnetic systems which exhibit both BEC phase of magnons and a quasi-1D regime. Then we present our results, where the determination of the quasi-1D regime is displayed along the phase diagram of DTN, showing a 3D-to-1D crossover, speaking in terms of magnetic behaviour. Finally, we extended our studies for higher temperatures, where the interaction among the spins is expected to become negligible. For such situation we discuss our estimate for D , which corroborate some results from literature and show discrepancy with others. The results presented in this Chapter were published in H. Fabrelli *et al*, J. Alloys Compd. **853**, 157346 (2021).

5.1 Quasi-1D systems in condensed matter

Matter and their interactions manifest themselves in the three-dimensional ($d = 3$) space. However, in some situations, depending on the symmetry of the system, boundary conditions and strength of the interaction along different directions of the space, one or more degrees of freedom can be neglected. So the description of such systems can be approximated as if they were low dimensional ($d < 3$) entities.

In condensed matter physics, specially in magnetism, there are a number of systems for which a low dimensional description is valid, leading to interesting results and potential applications [109–111].

One-dimensional systems are interesting not just for their conceptual simplicity but also for the possibility of finding exact solutions as in the case of the 1D Ising model [74, 112] and for some quantum models by means of the so called *Bethe ansatz* [113–115].

Regarding 1D fermi systems, the role of dimensionality leads to drastic changes in the behaviour of such systems in different dimensions. Fermi systems with interaction are well described by the Fermi liquid theory [116] for 2D and 3D cases. However, this theory fails for 1D systems due to intractable infrared divergences of vertices in the perturbation

theory [117]. In order to deal with this problem, the Tomonaga-Luttinger Liquid (TLL) theory was formulated [117, 118], and it shows some proprieties that are not present in higher dimension Fermi systems. Some characteristics of a TLL include [114, 117]:

- The non-existence of individual excitations but collective ones, which implies the appearance of charge and spin excitations separately, each one with its propagation velocity, v_{ch} and v_{sp} , respectively.
- The power-law decay of correlation functions at $T = 0$ and all other low-energy proprieties driven by the exponents u and K from the TLL model hamiltonian

$$H = \frac{\hbar}{2\pi} \int \left[\frac{uK}{\hbar^2} (\pi\Pi(x))^2 + \frac{u}{K} (\nabla\phi(x))^2 \right] dx, \quad (5.1)$$

where $u = (v_{ch}v_{sp})^{1/2}$ is the sound velocity, K is a dimensionless parameter, $\Pi(x)$ is the canonical momentum and $\phi(x)$ is the free scalar field operator [114].

- The gapless linear energy dispersion at long wavelength which, as in the case of a Fermi liquid, leads to a linear dependence of the specific heat with the temperature in the form

$$c_{TLL} = \frac{R\pi}{6u} T, \quad (5.2)$$

where R is the gas constant.

Since the conception of TLL theory, several quasi-1D systems has been experimentally investigated in order to verify the predictions from the theory. Carbon nanotubes [119, 120], electronic quantum circuits [121], optically trapped Bose and Fermi gases [122, 123], and quantum magnets are some examples of systems described by TLL theory.

Regarding quantum magnets, since field-induced antiferromagnetism can be mapped into bosonic systems and the TLL behavior is also linked to a 1D bosonic system via bosonization [114] both systems are closely related. Some efforts have been made in the past years to identify such phenomena in magnetic systems [20, 21, 124–131]. One requirement of such systems is that the interactions among the spins in one direction is much larger than in other directions, which make these systems behave nearly as 1D systems and so display the physics of the TLL regime. In table 5.1 we present some examples of magnetic systems where the TLL regime is observed.

The possibility for the existence of a TLL regime was also studied in DTN. NMR experiments [133] and theoretical predictions [132] claim that a genuine TLL regime in DTN should occur for a energy scale comparable to the one in which the BEC of magnons occurs, due to the interplay between the large- D gap and the interchain interactions. In fact, the observation of a pure TLL regime in DTN is difficult to achieve since the interchain interactions are not negligible regarding the intrachain interactions ($J_{ab}/k_B = 0.18K$ and $J_c/k_B = 2.2K$) if we compare with the exchange interactions of compounds in which the TLL regime is observed (see table 5.1).

Table 5.1: Some examples of quasi-1D quantum magnets in which the existence of the TLL regime was identified. The exchange coupling J_{\perp} , also known as J_{rung} , leads to the formation of dimmers while J_{\parallel} , also called J_{ladder} is responsible to the coupling of dimmers along one dimension. The term J' is the interladder (interchain) coupling which for these examples is very small and, in some cases, hard to determine. T_{maxLL} is the maximum temperature in which the TLL regime is observed while H_{LL1} and H_{LL2} delimit the range of the external magnetic field in that such regime is observed. All the compounds presented here are quasi-1D $S = 1/2$ AFM dimmers except in the case of NTENP which is a $S = 1$ bond-alternating chain.

Compound	J_{\perp}/k_B	J_{\parallel}/k_B	J'/k_B	T_{maxLL}	H_{LL1}, H_{LL2}	References
$\text{Cu}(\text{NO}_3)_2 \cdot 2.5\text{D}_2\text{O}$	5.16(4) K	1.39(5) K	0.06 K	220(5) mK	3.10 T, 3.92 T	[124].
F_5PNN	5.6 K	2.8 K	0.07 K	>0.8 K	? T, 5.8 T	[125, 126].
$\text{Ni}(\text{C}_9\text{H}_{24}\text{N}_4)(\text{NO}_2)\text{ClO}_4$ (NTENP)	54.2 K	24.4 K	0.12 K	>2.5 K	12 T, ?	[20, 127].
$(\text{C}_5\text{H}_{12}\text{N})_2\text{CuBr}_4$ (BCBP)	12.9 K	3.6 K	0.02 K	1.5 K	6.99(5) T, 14.4(1) T	[128–130].
$(\text{C}_7\text{H}_{10}\text{N})_2\text{CuBr}_4$ (DIMPY)	9.5 K	16.5 K	?	>1.5 K	2.6 T, 29 T	[21, 131].

Nevertheless, the emergence of a quasi-1D in DTN was reported from some magnetoacoustic measurements [134], where the authors suggest the presence of the crossover between 1D fermionic to the 3D bosonic magnetic excitations.

In this work we performed AC magnetic susceptibility and specific heat measurements along with QMC calculations and we also verify the existence of a quasi-1D regime in DTN. Our results are presented in the next section.

5.2 Results for the quasi-1D regime

In this section we present our results of magnetization, AC magnetic susceptibility and specific heat measurements along with 1D and 3D QMC calculations for DTN. We concentrate our studies in a range of temperature right above 1.2 K, which corresponds to the maximum temperature for the observation of the BEC of magnons in DTN. In such temperatures the thermal fluctuations are higher than J_{ab}/k_B , so the interchain coupling becomes small in comparison with the thermal fluctuations and, as a consequence, the long-range order is suppressed. However if the temperature of the system is lower or comparable with J_c/k_B , a short-range rather than a long-range ordering manifests itself. In this situation the system is a collection of quasi-1D chains along the c -axis. Further, when $T \gg J_c/k_B$, the thermal fluctuations overcome the interaction among the spins and the system is in the paramagnetic phase.

Figure 5.1 illustrates the magnetic ordering of DTN in different ranges of temperature.

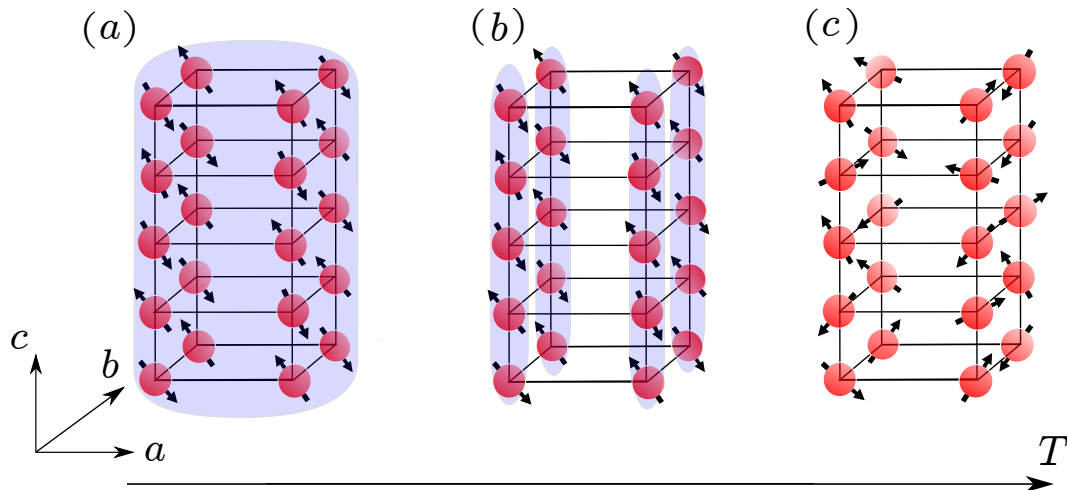


Figure 5.1: Schematic representation of the correlations among Ni^{2+} in DTN for different temperature ranges. In (a), corresponding to $k_B T \sim J_{ab}$, the system displays a the field-induced antiferromagnetic long-range order, represented by the blue-shaded region. With an increasing of the temperature, for $k_B T \sim J_c$, the long-range ordering vanishes, but a short-range ordering is present and the system becomes a collection of quasi-1D chains, as shown in (b). When $k_B T \gg J_c$, the interaction among the spins becomes negligible and the system is a collection of independent spins (as shown in (c)).

The first result presented in this chapter concerns our measurement of AC magnetic susceptibility χ_{AC} as a function of the external magnetic field H , applied parallel to the c -axis, for temperatures higher than 1.2 K - the highest temperature for the observation of BEC of magnons in DTN.

Additionally to the experiments we performed QMC simulations in order to compare with our experimental results. For 1D simulations we considered a chain with 256 spins with periodic boundary conditions and initially ran over 4×10^5 QMC steps, which we discarded due to the thermalization, and took the next 8×10^6 steps to calculate the magnetization. In the fully 3D calculations we employed a $8 \times 8 \times 32$ grid with periodic boundary conditions and discarded the first 2×10^5 steps, taking the next 4×10^6 steps. For these simulations we consider as the parameters of the hamiltonian $J_{ab}/k_B = 0.18$ K, $J_c/k_B = 2.2$ K, $D/k_B = 8.9$ K and $g = 2.2$, as estimate in thermodynamic [50], neutron scattering [54] and electron spin resonance measurements [51]. In 1D simulations we take $J_{ab}/k_B = 0$ K.

Once we have the magnetization, we obtain the susceptibility by the derivative of $M(H)$ with respect to H . It is worth to mention that this susceptibility, sometimes called *static susceptibility* can differ from the AC susceptibility for high frequencies of the AC excitation field. However in our measurements we apply a 155 Hz AC field, which is sufficiently low and allow us to compare the AC and the static susceptibilities.

In figure 5.2 (a) and (b) we present our results of AC magnetic susceptibility with the 1D and 3D QMC simulations both for BEC regime temperatures (a) as well as above it (b). We see from the curves that the more we increase the external magnetic field H the more χ_{AC} increases, due to a weak paramagnetic response of the large- D gap. Keeping increasing the field the gap closes and both ground state ($S_z = 0$) and the excited state ($S_z = 1$) becomes degenerated. In figure 5.2 (a) we observe cusps around the critical fields, which are characteristic of a long-range ordering. In figure 5.2 (b), since in the measurements the temperature is higher than 1.2 K, which makes $T \gg J_{ab}/k_B$, a long-range ordering do not manifests itself. Instead, a quasi-1D antiferromagnetic behavior arises, characterized by the presence of a broad maximum which is a consequence of the short-range correlations [44]. For even higher fields a spin polarized phase arises and, consequently, the saturation of magnetic moments. This is characterized by the appearance of a second maximum in the $\chi_{AC}(H)$ curves.

To characterize the results in figure 5.2 (b) as the signature of a quasi-1D regime, we compare the $\chi_{AC}(H)$ curves both above and below 1.2 K with 1D and 3D QMC calculations.

As we would expect, for BEC regime temperatures (figure 5.2 (a)) the best agreement between the experimental and theoretical results is given by the 3D QMC rather than 1D QMC calculations, once a 3D ordering of the system is expected for such temperatures.

This situation changes for $T > 1.2$ K, where a long-range ordering is no longer expected. In fact for this case (figure 5.2 (b)) we observe that both 1D QMC as well 3D QMC calculations displays nearly the same results and they significantly corroborate our experimental results. It indicates that for such temperatures a 1D description of the system is suitable.

In figures 5.2 (c) and (d) we highlight the differences between the 3D and 1D QMC calculations for $T = 0.6$ K, which corresponds to a BEC regime temperature.

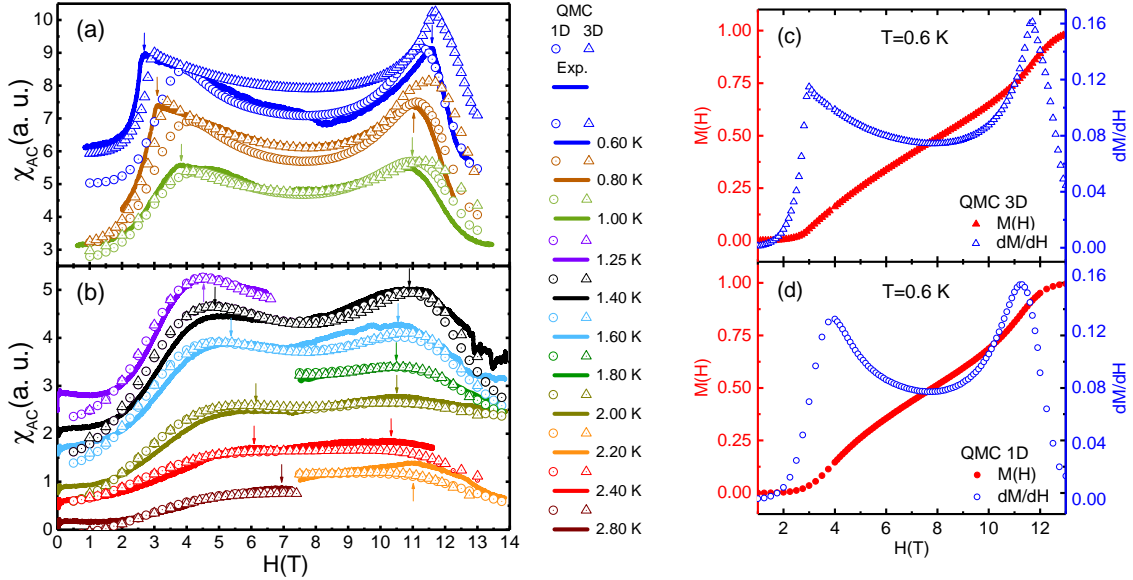


Figure 5.2: $\chi_{AC}(H)$ measurements for temperatures to the occurrence of the BEC phase (a) and above those for the occurrence of the BEC phase (b). Continuous lines correspond to our measurements. Dotted circles and triangles are the results from 1D and 3D QMC calculations respectively. The maximum of susceptibility curves are indicated by arrows. In figure (c) and (d) we display magnetization and static susceptibility results from 1D and 3D QMC calculations at $T = 0.6$ K.

From figure 5.2 we see a good agreement between the experimental data and the 1D numerical simulations, confirming the quasi-1D nature of DTN for such temperatures.

We also performed specific heat measurements as a function of H for temperatures down to 1.8K and magnetic fields up to 9T, applied parallel to the c -axis. We observe that the $C(H)$ curves display a non monotonic behaviour, since they decrease with the field up to a certain value which coincides with the first maximum of the χ_{AC} curves. Then the curves start to increase again with the increasing of H .

Similar results were reported theoretically for $S = 1$ chains with large easy-plane anisotropy [135], in measurements for the spin-1/2 ladder compound $(C_5H_{12}N)_2CuBr_4$ [129, 136], as well as in the context of optically trapped ultracold bose gases in a TLL regime, where the authors present curves of specific heat of the ultracold gas as a function of the chemical potential μ [137]. According to the spin-boson mapping presented in chapter 2, the external magnetic field in a spin system is equivalent to the chemical potential in a bose system, which makes the comparison of our results with those in reference [137] straightforward. These results are presented in figure 5.3.

From the position of the maxima in the magnetic susceptibility in both experimental and QMC data and the minima of $C(H)$ curves, we present the phase diagram of DTN with our results for the quasi-1D regime in figure 5.4. Magnetocaloric effect and specific heat data measurements were obtained from reference [54].

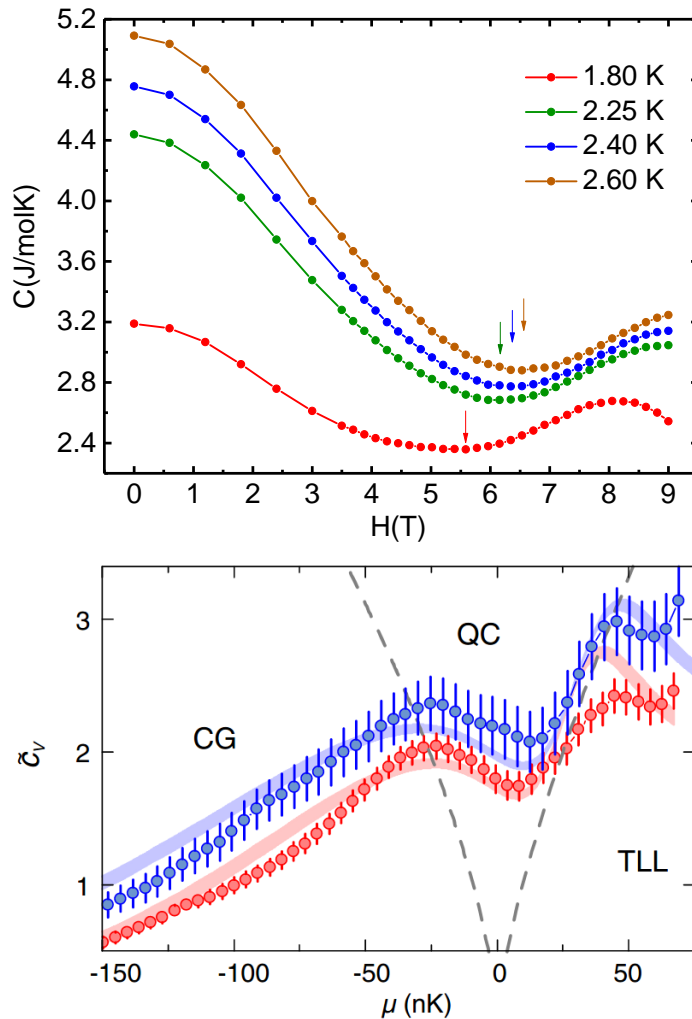


Figure 5.3: Top panel: Specific heat of DTN as a function of the external magnetic field H for some temperatures. The arrows indicate the position of the minima for each curve. Bottom panel: Specific heat of an optically trapped ultracold gas as a function of the chemical potential μ (figure adapted from reference [137]).

We see in the diagram of figure 5.4 a reasonable agreement between the experimental points and the theoretical data. Some discrepancies may have origin in the size of de grids employed in the simulations and a small misalignment of the samples. The curves of 1D and 3D QMC calculations nearly display the same results, from what we can attest the quasi-1D nature of the system. From slight displacement from both 1D and 3D curves we can conclude that, although the system in a good approximation behaves as a quasi-1D system in these temperature and field ranges, the interchain interaction J_{ab} still gives a small contribution in these conditions.

Very similar phase diagrams are also presented for the compounds presented in table 5.1, where the authors presents both the BEC phase diagram and the region of the TLL regime. Although such compounds really display the TLL regime due to their negligible interchain interactions our results resembles to these presented in the literature.

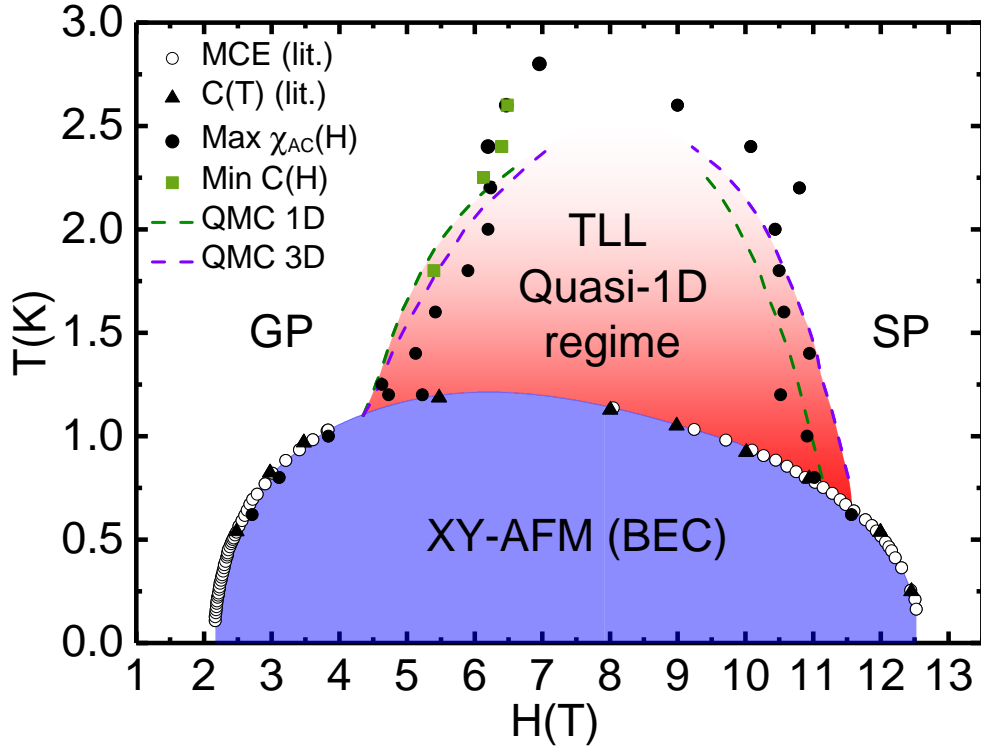


Figure 5.4: BEC phase diagram for DTN (blue shaded region) with our results in the quasi-1D regime (red shaded region). Black circles correspond to the maxima of $\chi_{AC}(H)$ curves while the green squares denote the minima of $C(H)$ curves. Dashed green and purple curves were obtained from 1D and 3D QMC calculations respectively. GP stands for gapped regime while SP is the spin-polarized regime. The BEC phase diagram presented here was obtained from previous magnetocaloric effect (MCE) and specific heat measurements from reference [54].

We suggest that for DTN the spin chains along the c -axis are weakly coupled to each other and this leads to a regime of weakly coupled TLL chains [10, 128, 138]. However, in order to explore this hypothesis more theoretical and experimental efforts are necessary. This can motivate further studies.

5.3 Higher temperatures ($T > J_c/k_B$) results

Until now we have discussed the temperature range where $T > J_{ab}/k_B$. Now, let us consider the case for higher temperatures, where $T > J_c/k_B$ and the contribution to the magnetism of the system is given mostly by the single-ion anisotropy and by the Zeeman term.

We performed magnetization measurements using the PPMS-VSM in a range of temperature from 2 K to 10 K under different values of the external magnetic field. These results are presented in figure 5.5 (left panel), where we display curves of DC magnetic susceptibility, defined as $\chi_{DC}(T) = M(T)/H$, where $M(T)$ is the magnetization as a function of the temperature. We compare these results with 1D QMC calculations.

Initially we used in our simulations the same parameters in the hamiltonian mentioned before. However we note that in order to fit the simulations with our experimental data the value of D should be around 15% smaller. In other words, instead of adopting $D/k_B = 8.9$ K best fittings are found when we consider $D/k_B = 7.6$ K.

Additionally we compare the experimental results and the QMC calculations with an analytic expression to the magnetization given for an ideal paramagnet. In such situation, where $T \gg J_c/k_B$, the magnetization per ion in this system, according to the theory presented in Appendix C, is given by

$$M(T, H) = g\mu_B \frac{\sinh(g\mu_B H\beta)}{\cosh(g\mu_B H\beta) + \frac{1}{2}e^{\beta D}}, \quad (5.3)$$

where $\beta = 1/k_B T$.

From figure 5.5 (right panel), where we plotted the temperature in which the maximum of $\chi_{DC}(T)$ is observed as a function of the external magnetic field, we see that the smaller the value of H the better are our adjusts considering $D/k_B = 7.6$ K. For higher fields the maximum of $\chi_{DC}(T)$ is observed in lower temperatures and so the contribution of J_c cannot be neglected. This explains why the results given by (5.3) diverge comparing with the experimental data for higher H .

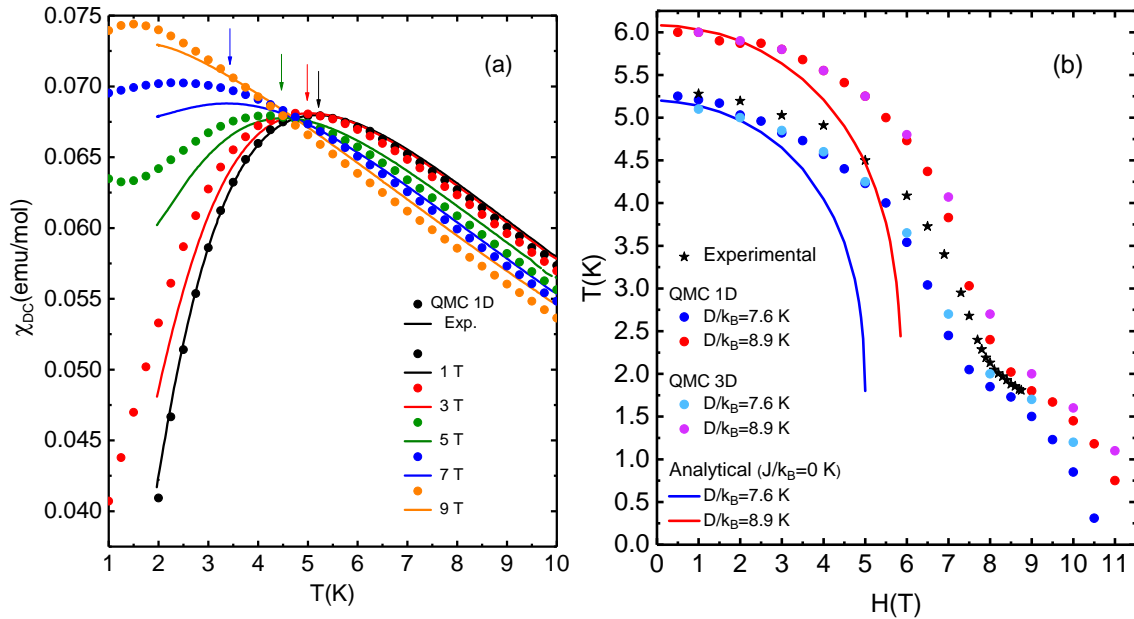


Figure 5.5: Left panel: DC magnetic susceptibility (χ_{DC}) of DTN as a function of the temperature for different values of external magnetic field. Full lines correspond to our experimental data while dots are from 1D QMC calculations. The arrows indicate the maxima of $\chi_{DC}(T)$ curves. Right panel: Temperature of the maximum of $\chi_{DC}(T)$ curves for different values of H . The experimental data is denoted by black stars, while the results from QMC calculations are denoted by full circles. The continuous lines were obtained from the equation (5.3) for the paramagnetic phase.

We also see that, the higher the external magnetic field and the lower the temperature, the better are the agreement between both theoretical and the experimental results. The reason is that, for such conditions, the contributions of Zeeman term as well as the exchange interactions became more and more relevant. In this sense, whatever the value of the single-ion anisotropy between $D/k_B = 7.6$ K and $D/k_B = 8.9$ K, the experimental and theoretical results tends to agree at low temperatures and high magnetic fields.

In fact, in the literature different values for the single-ion anisotropy in D are reported. The first work which identified the field-induced antiferromagnetic phase in DTN gave an estimate for the single-ion anisotropy as $D/k_B = 7.6$ K, by fitting mean-field expressions to AC magnetic susceptibility experimental curves [49]. Later, electron spin resonance (ESR) measurements together with theoretical fittings to the spectrum found $D/k_B = 7.72$ K for external magnetic fields near H_{c1} and $D/k_B = 8.9$ K near H_{c2} [62]. In reference [54], the authors estimated from neutron scattering measurements $D/k_B = 8.12(4)$ K. However, the most adopted value for D/k_B in literature is $D/k_B = 8.9$ K, given by ESR experiments at external magnetic field up to 25 T [51].

It is worthwhile to mention that the advantage of determining the magnitude of parameters of the system, such as exchange couplings, anisotropies and gyromagnetic factor, by making measurements in low fields is that one minimizes any eventual effects, for example magnetostriction, demagnetizing factor and torque, that manifest due to the presence of the applied magnetic field. The influence of these high fields effects may leads to errors when one estimates the magnitude of the desired parameters.

We suggest that such discrepancy between the values of the single-ion anisotropy may arises either by these aforementioned effects that manifest themselves under high external magnetic fields or from other interactions not took into account in the hamiltonian that describes the DTN, for example Dzyaloshinskii-Moriya or even higher-order-neighbour interactions. Therefore further investigation are necessary in order to elucidate this issue.

5.4 Conclusions

In this chapter we present our AC magnetic susceptibility, magnetization and specific heat measurements as well as QMC calculations in 1D and 3D for the DTN above 1.2 K, which is the maximum temperature for the observation of BEC of magnons in this compound. Our studies shows that under these conditions, the system displays a quasi-1D behaviour rather than the long-range order observed in the BEC phase. This allow us to delimit the region in the phase diagram where such regime is observed.

For some examples of field-induced antiferromagnets in the literature a TLL phase was also identified. Although our results resembles these results, a genuine TLL regime in DTN is not expected since the contribution of interchain interactions J_{ab} is small but not negligible. However the existence of the crossover between the bosonic excitations in the BEC phase to fermionic excitations in temperatures correspondent to the quasi-1D regime [133, 134] may indicate that some reminiscent of a TLL regime still plays some

role in DTN. One possibility that deserves further investigation is the existence of weakly coupled TLL chains, leading to complex behaviour of the magnetic excitations.

Furthermore, we performed magnetization measurements for $T > J_c/k_B$ where the magnetism of the system is mainly ruled by the Zeeman term and the single-ion anisotropy. The comparison between our results with QMC simulations and a theoretical approximation shows that the value of the single-ion anisotropy is around 15% less than the value usually adopted in the literature, which is $D/k_B = 8.9$ K. Our results reinforce the discrepancy of such result in the literature with other reported values. This issue invites to further investigation in order to clarify this unconformity.

Chapter 6

Magnetic and Specific heat investigations on DTM and DTF compounds

In addition to our studies on the DTN compound presented in the previous chapter we also synthesized and performed magnetic and specific heat measurements in the Mn and Fe based parent compounds of DTN, $\text{MnCl}_2\text{-4SC(NH}_2)_2$ (DTM) and $\text{FeCl}_2\text{-4SC(NH}_2)_2$ (DTF). Initially we discuss some existing results for DTM and DTF compounds. Then we present our magnetization results of DTM and DTF, comparing with DTN results and estimate, from the Curie-Weiss law and mean-field calculations, the exchange couplings J , the single-ion anisotropy D and gyromagnetic factor g of such compounds. We also performed AC magnetic susceptibility and specific heat measurements, revealing the existence of two phase transitions occurring in DTM, which allow us to construct a magnetic phase diagram for this compound, and the absence of phase transitions in DTF down to 100 mK. Finally, we make some general remarks on the nature of exchange interactions in these compounds.

6.1 DTM and DTF compounds

Despite the DTN compound has been intensively studied in the past two decades, very few studies were dedicate to explore the physics of its parent compounds DTM and DTF.

Regarding DTM, some AC magnetic susceptibility measurements at $H = 0$ T in single crystals were performed by H. J. Van Till, where the author identified an antiferromagnetic transition around $T = 0.56$ K [139]. Later, some magnetic measurements parallel to the (111) plane and down to 2 K as well as specific heat measurements down to 0.4 K for some values of external magnetic fields up to 4 T applied perpendicular to the (111) plane did not pointed out any indicative of phase transitions [87]. We reproduce these results in figure 6.1, for the specific heat curves, and figure 6.2, for the estimate energy levels obtained from multi-level Schottky fits given by (2.79).

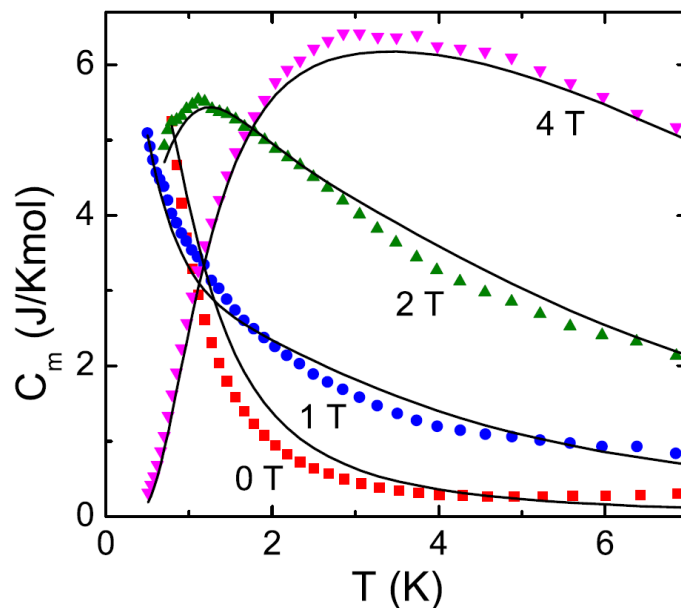


Figure 6.1: Specific heat of DTM measured for magnetic field applied perpendicular to the (111) plane (colourful dots) and multi-level Schottky fits (black curves) obtained from expression (2.79). This figure was adapted from reference [87].

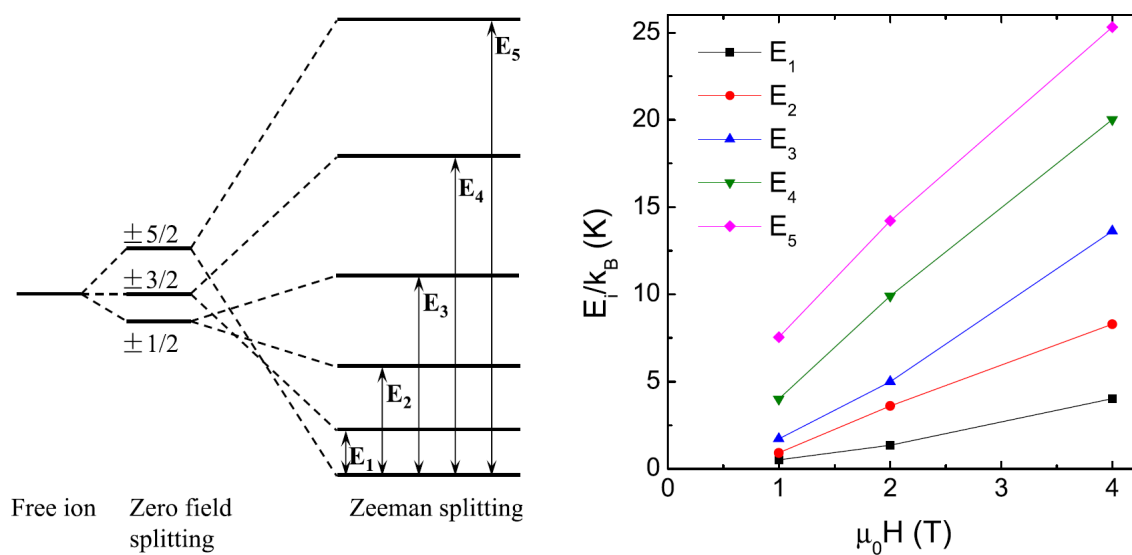


Figure 6.2: Representation of the energy levels in Mn^{2+} taking into account the zero-field and Zeeman splittings (left panel). Energy levels of DTM as a function of external magnetic field (right panel) obtained from multi-level Schottky fits to the specific heat data in figure 6.1. These figures were adapted from reference [87].

For the DTF compound, a magnetic measurement was carried out down to 4 K for the powdered samples and no indicative of magnetic ordering was identified [140]. After, some Mössbauer measurements determined the electronic transition energy to the 5E_g level equal to 8700 cm^{-1} [141, 142]. The value for the ${}^5T_{2g}$ transition was not reported.

Motivated by the lack of magnetic and specific heat measurements we devoted part of this work to study both DTM and DTF compounds under external magnetic fields and at lower temperatures.

6.2 Results from magnetic measurements

The first results of this section are the $\chi_{DC}(T)$ measurements at $H = 0.01$ T and $M(H)$ measurements for DTM and DTF single crystals in different orientations and the comparison with DTN results. These results are presented in figures 6.3 and 6.4.

As we can see from figures 6.3 and 6.4, DTM and DTF displays each one the same behaviour of $\chi_{DC}(T)$ and $M(H)$ along two directions perpendicular to the c -axis, since for these directions the curves of the measurements lies in each other, which points out that both compounds have an uniaxial magnetic anisotropy.

In order to estimate a exchange coupling J , the single-ion anisotropy D and the gyromagnetic factor g for DTN, DTM and DTF we fitted the curves in figure 6.3 with mean-field expressions for the zero field magnetic susceptibility given by [44, 46, 143]

$$\chi(T) = \frac{\chi_0(T)}{\left(1 + \frac{2zJ}{Ng^2\mu_B^2}\chi_0(T)\right)}, \quad (6.1)$$

where z is the coordination number and $\chi_0(T)$ is the zero field magnetic susceptibility calculated for a single ion. In Appendix C we present the zero field magnetic susceptibility expressions calculated for single ions with $S = 1$, $S = 2$ and $S = 5/2$.

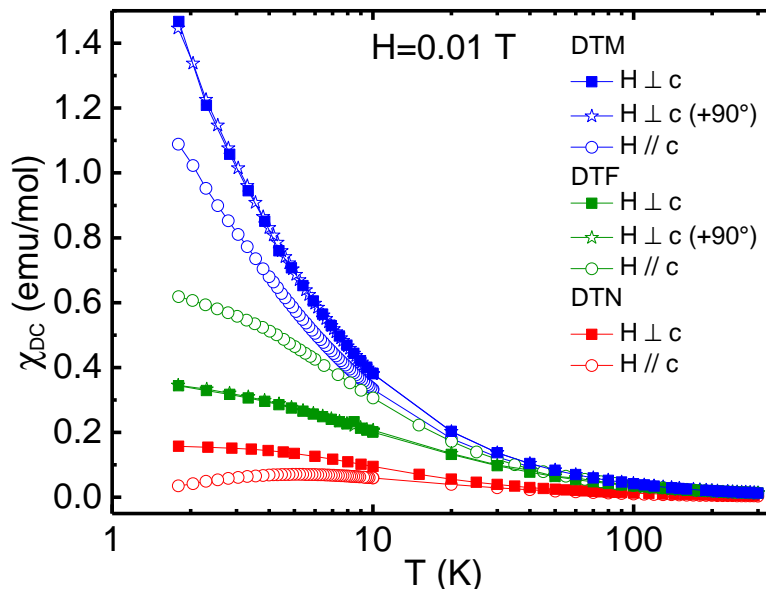


Figure 6.3: $\chi_{DC}(T)$ curves of DTN (red curves), DTM (blue curves) and DTF (green curves) measured under an external magnetic field $H = 0.01$ T in different orientations, with magnetic field applied parallel to c -axis, perpendicular to c -axis and perpendicular to the c -axis with a rotation of 90° from the previous one.

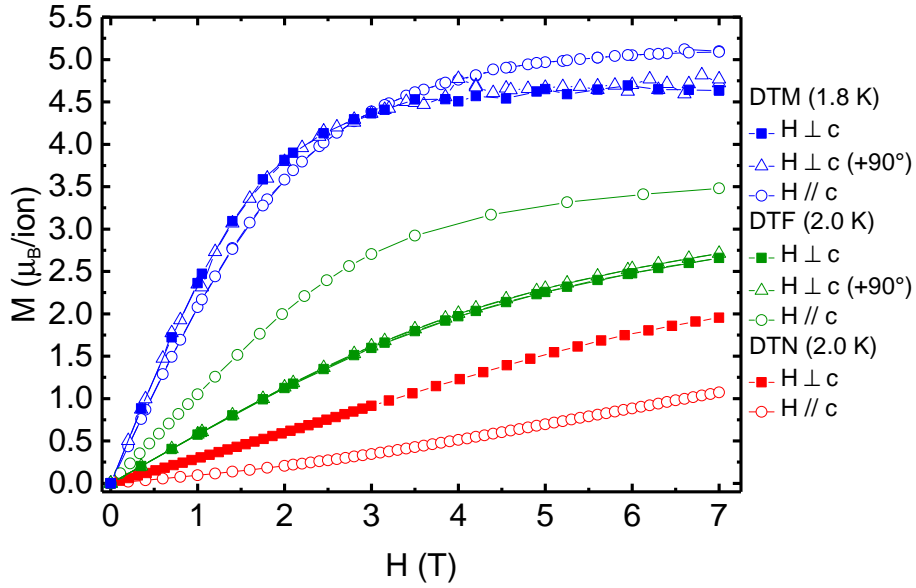


Figure 6.4: $M(H)$ curves of DTN (red curves), DTM (blue curves) and DTF (green curves) measured in different orientations, with magnetic field applied parallel to c -axis, perpendicular to c -axis and perpendicular to the c -axis with a rotation of 90° from the previous one.

In figure 6.5 we display in each panel the $\chi_{DC}(T)$ curves of each compound studied in this chapter as well as the correspondent fittings obtained from the expression (6.1). We see in figure 6.5, in all the $\chi_{DC}(T)$ curves presented, a very good agreement between the experimental data with the fittings from the mean-field theory. The obtained values of J , D and g parameters from these fits are presented in table 6.1.

To obtain a hint on the magnetic ordering and the strength of interactions in these systems we can analyse our results with help of the well known Curie-Weiss law, which states that the inverse of the magnetic susceptibility follows as

$$\frac{1}{\chi} = \frac{1}{C}(T + \theta_{CW}), \quad (6.2)$$

where $C = Ng^2\mu_B^2/3k_B$ and for convenience we write a plus sign before θ_{CW} which means that if $\theta_{CW} > 0$ an antiferromagnetic ordering is expected in the system, otherwise, for $\theta_{CW} < 0$, the system may display a ferromagnetic ordering.

For such analysis, the results from figure 6.5 are plotted as $1/\chi_{DC}(T)$ in figure 6.6, from which we can extract the values of g and θ_{CW} from the Curie-Weiss law (6.2). The obtained values of J , D and g from these fittings are also presented in table 6.1.

We observe for all three compounds in both parallel and perpendicular directions of applied H with respect to the c -axis that the estimate of θ_{CW} gives a positive value. According to (6.2) it means that an antiferromagnetic ordering is expected for the three compounds.

From table 6.1 we see a good agreement for the values of p comparing with the data from the literature for single ions of Ni^{2+} , Fe^{2+} and Mn^{2+} [71]. For DTN and DTM we see that the linear adjust gives approximately the same value of θ_{CW} in the parallel and perpendicular directions. For DTF the values of θ_{CW} in the perpendicular directions are around 10 times grater than for the parallel direction with respect to the c -axis. Another point is that the greatest value θ_{CW} for DTF is around 1.5 times grater than for DTN. This suggests that an antiferromagnetic ordering should appear for temperatures comparable to those for DTN.

Table 6.1: Values of J/k_B , D , g and θ_{CW} obtained through the mean-field theory fittings and the Curie-Weiss law for measurements parallel and perpendicular to the c -axis. From literature [71] $p = 3.2$ for Ni^{2+} , $p = 5.9$ for Mn^{2+} and $p = 5.4$ for Fe^{2+} ions. The relation of p and g is given by $p = g[S(S + 1)]^{1/2}$.

	DTN		DTM		DTF	
	H c	H \perp c	H c	H \perp c	H c	H \perp c
θ_{CW} (K)	6.52	6.28	1.52	1.06	1.89	10.15
g_{CW}	2.08	2.34	1.89	1.97	2.21	2.25
g_{XDC}	2.17	2.29	1.89	1.97	2.29	2.24
p_{CW}	2.95	3.31	5.59	5.84	5.42	5.51
p_{XDC}	3.07	3.23	5.59	5.83	5.61	5.49
D_{XDC}/k_B (K)	7.62	7.53	-0.17	0.15	1.42	1.44
zJ_{XDC}/k_B (K)	4.93	3.53	0.73	0.44	0.37	4.76

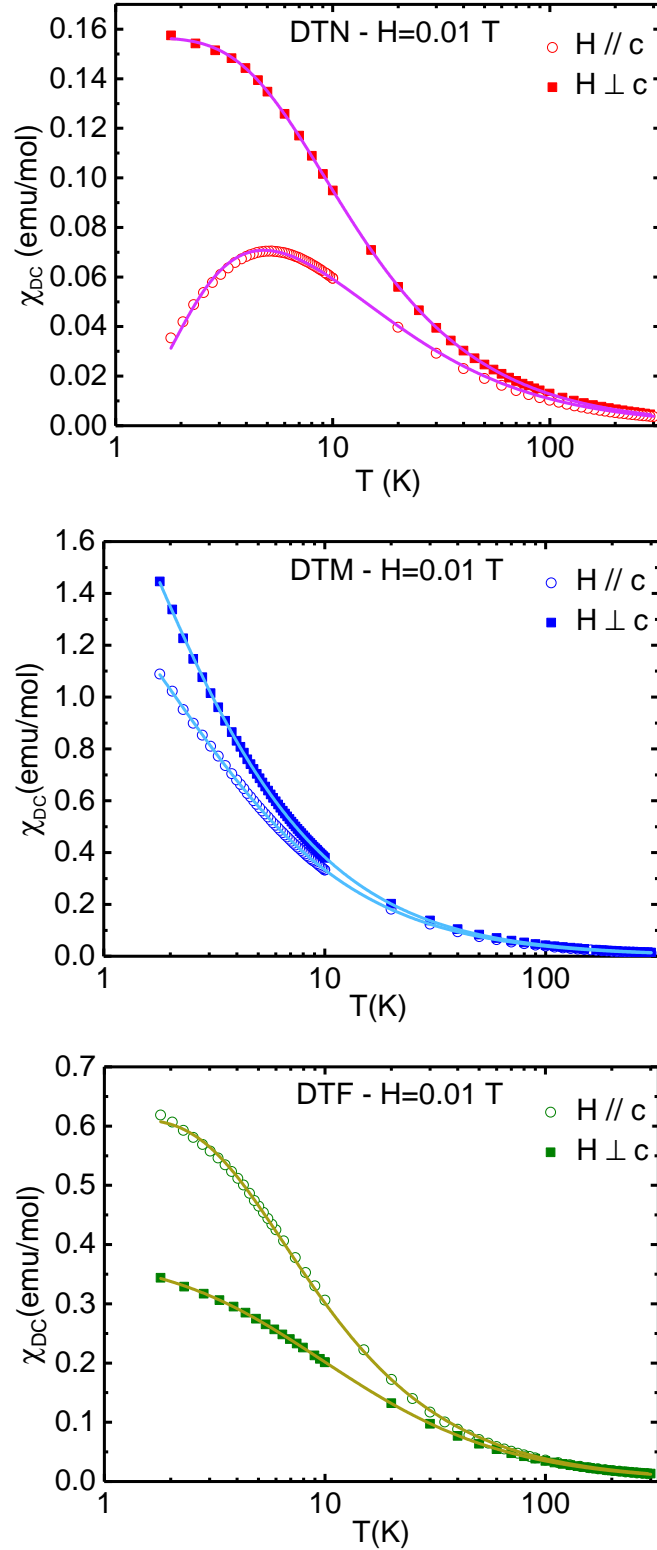


Figure 6.5: $\chi_{DC}(T)$ curves of DTN (top panel), DTM (middle panel) and DTF (bottom panel) measured under an external magnetic field $H = 0.01$ T in different orientations, with magnetic field applied parallel and perpendicular to c -axis. The lines correspond to the fittings obtained from equation (6.1).

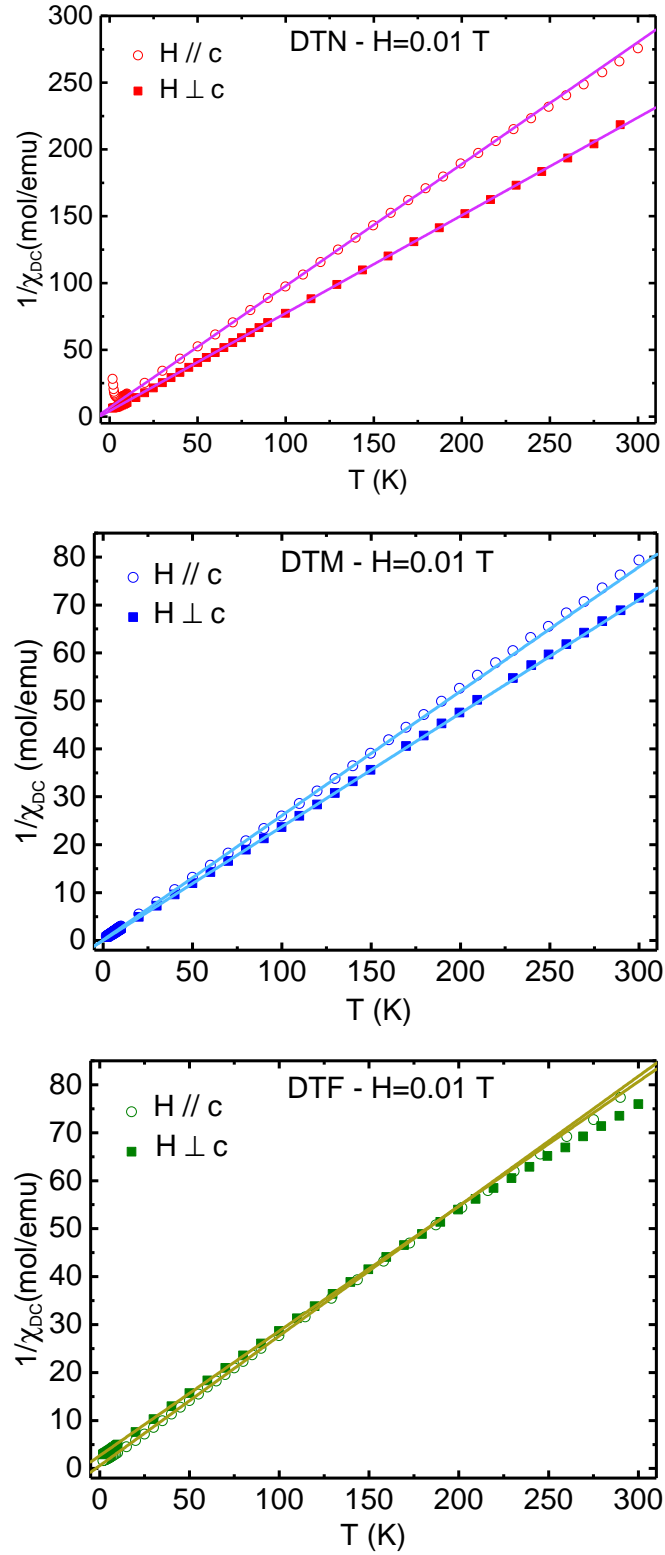


Figure 6.6: $1/\chi_{DC}(T)$ plots of DTN (top panel), DTM (middle panel) and DTF (bottom panel) measured under an external magnetic field $H = 0.01$ T in different orientations, with magnetic field applied parallel and perpendicular to c -axis. The lines correspond to linear fittings according to the Curie-Weiss law given by equation (6.2).

Figure 6.7 shows the magnetization curves as a function of H for DTM and DTF compounds.

We also compare these results with a theoretical model for an ideal paramagnet. Usually, experimental $M(H)$ curves are compared with the well-known Brillouin expression for ideal paramagnets. However, such expressions do not take into account the single-ion anisotropy, making this theoretical model inaccurate when single-ion anisotropies are relevant. In fact, if we try to adjust the Brillouin expression in our results of figure 6.7, the obtained curves do not fit the experimental results.

In order to provide a more accurate model which present a better agreement with our experimental results we derived expressions of $M(H)$ for an ideal paramagnet considering that our hamiltonian has both the Zeeman term and the single-ion anisotropy. The derived expressions are presented in Appendix C. However, one limitation of our proposed model is the fact that obtaining the analytical expressions for $M(H)$ curves for H applied perpendicular to the c -axis is very difficult since the expressions for the eigenvalues of the hamiltonian for this problem are very complicated. So, we compare our experimental results with a theoretical model only for H applied parallel to the c -axis.

As we see from figure 6.7 such fittings provide very good results. In the case of DTM we see that, even at low temperatures, $T = 0.52$ K, the fitted curve adjust very well to the experimental results, which suggest that for this compound a paramagnetic description is valid and so the exchange interactions should be small comparing to $k_B T$ (in other words, $J/k_B \ll T$). Additionally, the curves tends to saturate approximately around $M(\mu_B/\text{Mn}^{2+}) = 5$, which correspond to the expected saturation value for Mn^{2+} ions.

For DTF we observe a slightly different plot. While for temperatures down to 2 K the fittings also suggest a paramagnetic nature of the compound for such temperatures, for the $M(H)$ curve, at 0.58 K the fitted curve does not provide a good agreement. This may indicate that for such temperature and values of the external magnetic field the contribution of exchange interactions are significant, which explains the deviation of the theoretical curve obtained for an ideal paramagnet from our experimental result.

In the case of DTM compound we also performed some magnetic measurements for temperatures down to 0.45 K. In figure 6.8 we display $\chi_{DC}(T)$ measurements under an external magnetic field $H = 0.1$ T. As we see from this figure in both parallel and perpendicular directions to c -axis the $\chi_{DC}(T)$ present a kink around 0.6 K, what points out to an antiferromagnetic ordering below such temperature.

In addition to the already presented $\chi_{DC}(T)$ measurements, we also performed a $\chi_{AC}(T)$ measurement for the DTF powder to temperatures below to 0.3 K, as presented in figure 6.9. For this compound we observe a broad maximum around $T = 1.5$ K for the $\chi_{AC}(T)$ measurement of the powder rather than a kink as for the DTM, which would indicate the existence of an antiferromagnetic ordering. Despite the significant values of θ_{CW} summarized in table 6.1, such indicative of magnetic ordering is not present these measurements.

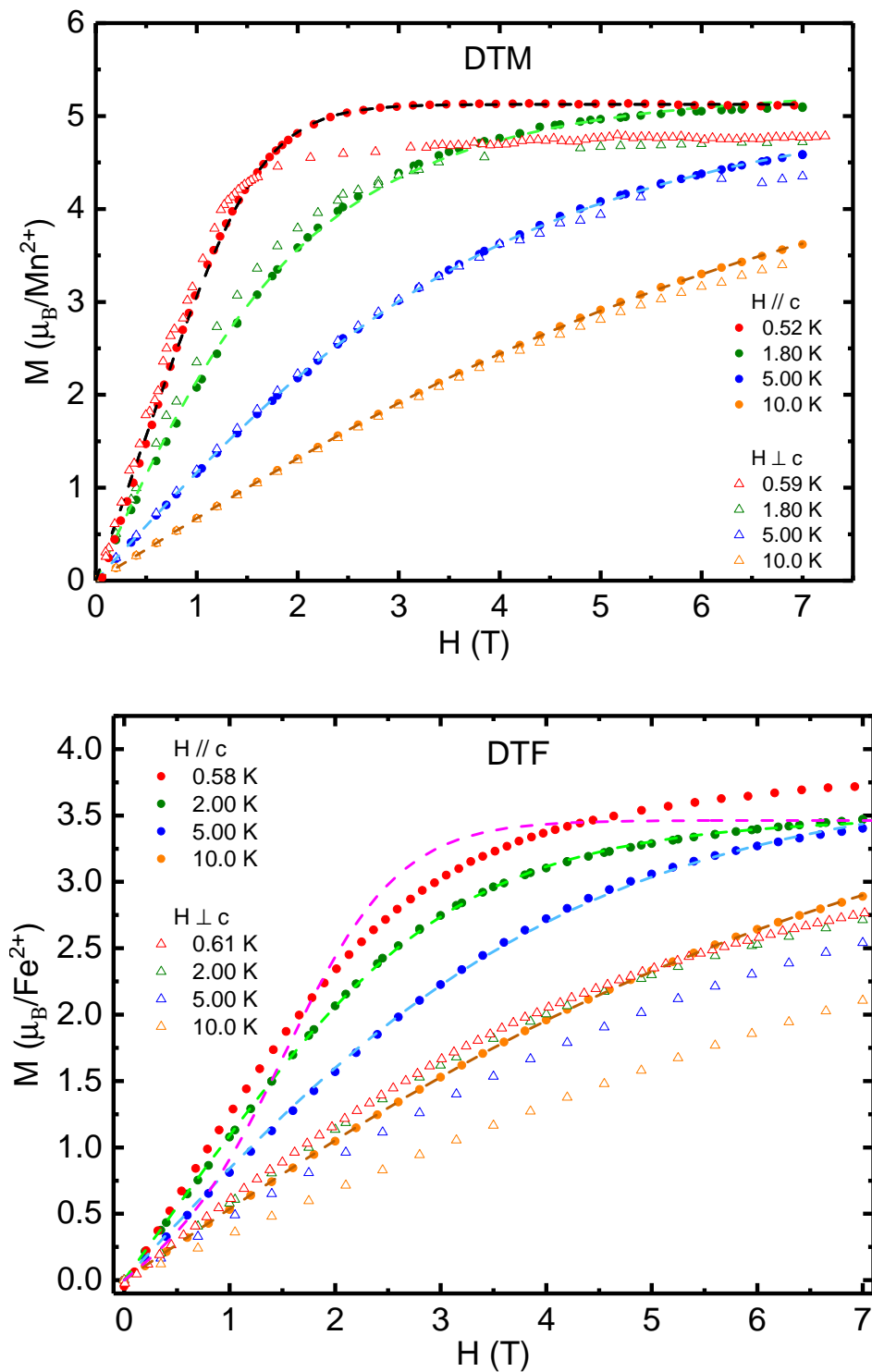


Figure 6.7: Magnetization measurements for DTM (top panel) and DTF (lower panel) as a function of the external magnetic field H for different temperatures. Circles and open triangles are experimental results while dashed curves are theoretical fittings from expressions in Appendix C for an ideal paramagnet under an external magnetic field applied parallel to the c -axis.

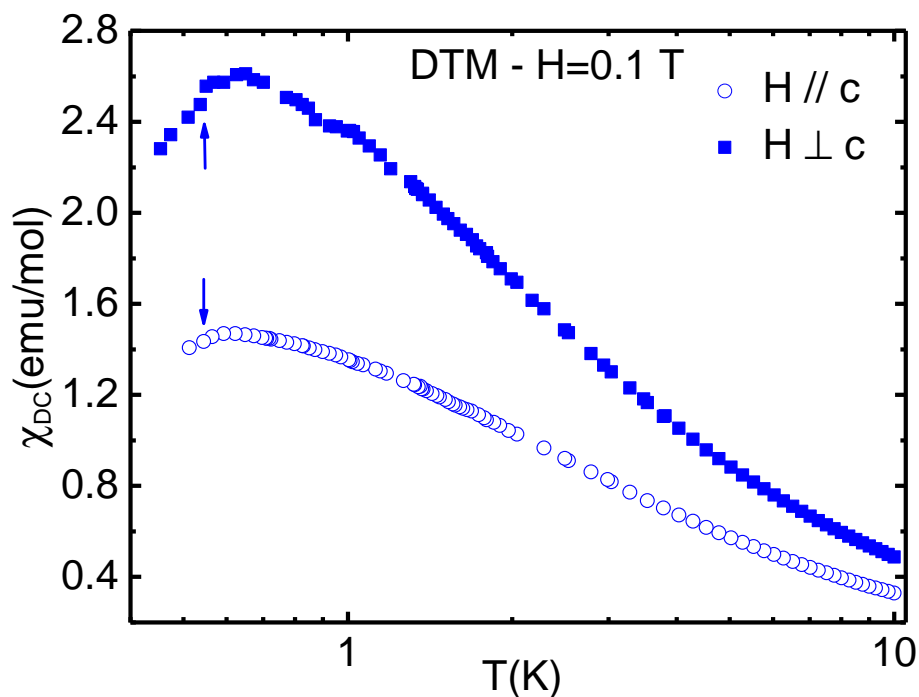


Figure 6.8: $\chi_{DC}(T)$ curves of DTM measured under an external magnetic field $H = 0.1$ T with magnetic field applied parallel and perpendicular to c -axis. The arrows indicate the position of the inflection point of such curves.

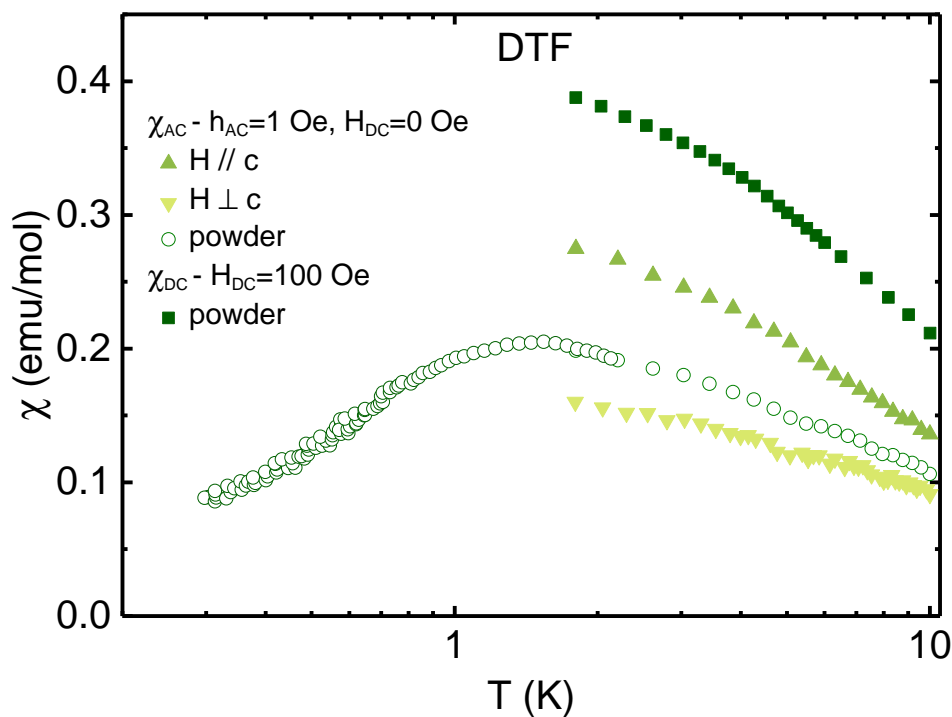


Figure 6.9: $\chi_{AC}(T)$ and $\chi_{DC}(T)$ for DTF in different crystal orientations and for powder samples.

6.3 Results from specific heat measurements for DTM

For DTM and DTF compounds we also performed measurements of specific heat for several values of applied magnetic field and temperatures.

As mentioned in the first section of this chapter, earlier specific heat measurements for DTM revealed no magnetic phase transitions for temperatures down to 0.4 K and external magnetic fields up to 4 T [87].

In our work we measured DTM and DTF samples for even lower temperatures, down to 100 mK.

In figures 6.10 and 6.11 we present our results for the total specific heat and for the magnetic contribution to the specific heat after the subtraction of the lattice contribution obtained from the non-magnetic parent compound $\text{CoCl}_2 \cdot 4\text{SC}(\text{NH}_2)_2$ (DTC).

Since both DTM and DTC compounds have different masses, it is expected that their lattice contributions are not equal to each other. From Chapter 2 we learn that the Debye temperature is linearly proportional to the sound velocity c_s of the acoustic waves in the solid. In a good approximation, $c_s \sim 1/\sqrt{M}$, where M is the molecular mass of the constituents in a lattice site. From this fact, we can rescale the Debye temperature of both compounds in order to express the lattice contribution of a compound as a function of the other [144]. Let us introduce the parameter r given by

$$r = \frac{\theta_D^{DTM}}{\theta_D^{DTC}} = \frac{M^{DTC}}{M^{DTM}}, \quad (6.3)$$

where θ_D^{DTM} and θ_D^{DTC} are the Debye temperatures of DTM and DTC, respectively. $M^{DTC} = 487.59$ u and $M^{DTM} = 430.12$ u are the molecular masses of DTM and DTC, respectively.

Using the rescaling parameter r , we can finally write the lattice contribution C_{latt}^{DTM} for DTM as a function of the lattice contribution C_{latt}^{DTC} for DTC as

$$C_{latt}^{DTM}(T) = C_{latt}^{DTC}(rT). \quad (6.4)$$

Regarding the magnetic contribution to the specific heat in figures 6.11, we see that in both orientations, with the external magnetic field applied parallel and perpendicular to the c -axis, the sample displays antiferromagnetic phase transitions for several values of magnetic field. For a large enough field we observe the usual suppression of the antiferromagnetic transition with the transition temperature T_N moving to lower temperatures while decreasing the height of the peak.

Specially for the sample oriented in the perpendicular, there are two transitions. From these curves we extracted the phase diagram shown in figure 6.12.

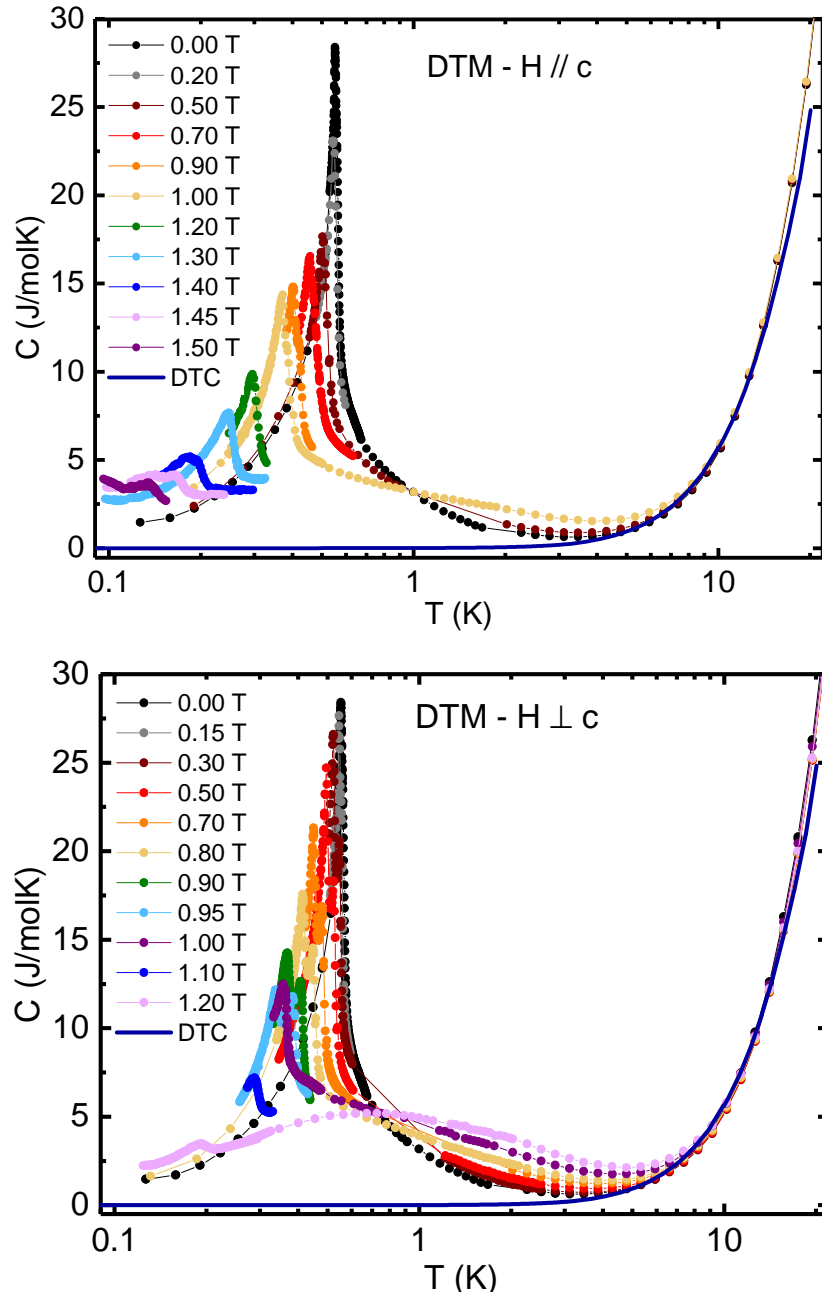


Figure 6.10: Total specific heat measured for DTM for several values of external magnetic field applied in parallel (top panel) and perpendicular (bottom panel) to the c -axis orientation. In both figures we compare the measured curves with the specific heat measurement of DTC compound (see text).

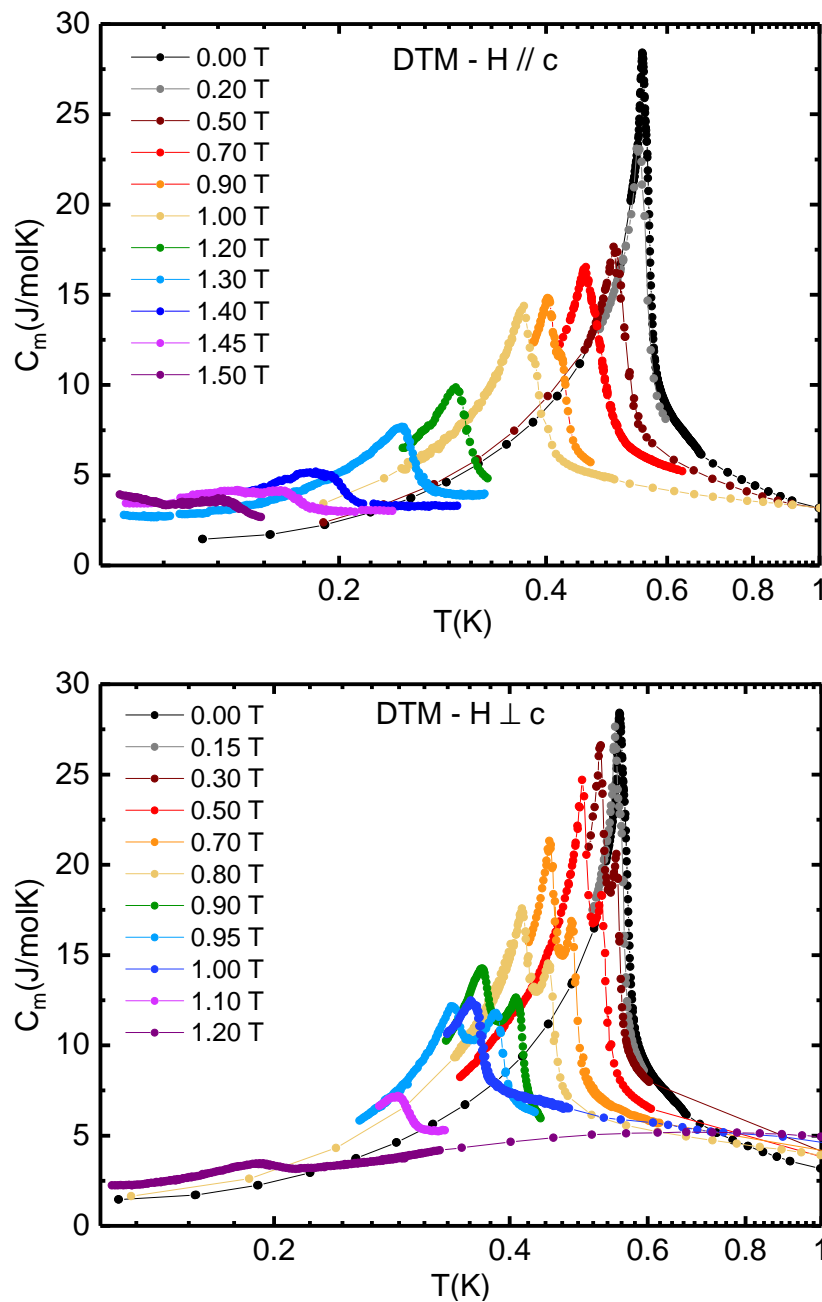


Figure 6.11: Magnetic contribution to the specific heat of DTM for several values of external magnetic field applied in parallel (top panel) and perpendicular (lower panel) to the c -axis orientation. These curves were obtained after subtracting the lattice contribution, obtained from the specific heat of DTC compound, from the total specific heat curves presented in figure 6.10.

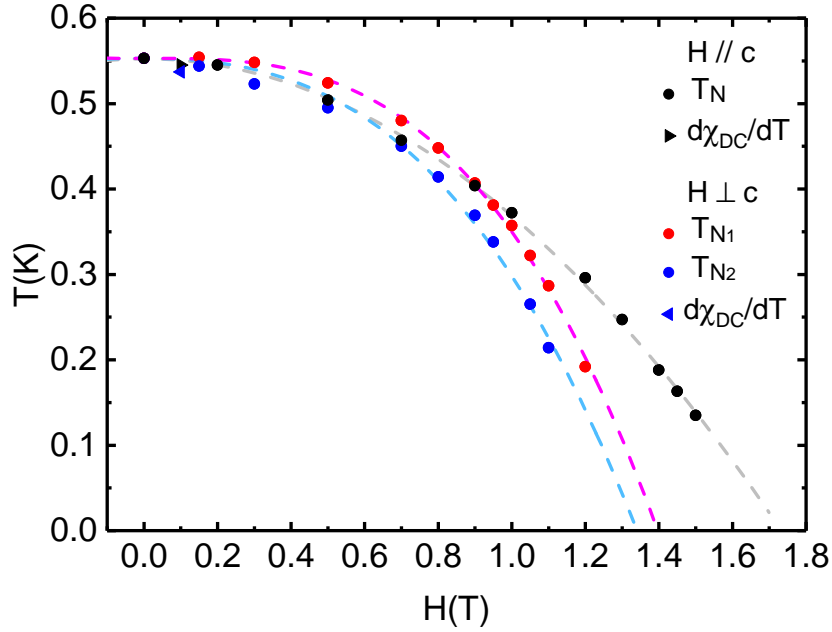


Figure 6.12: Phase diagram of DTM obtained from the peaks in the specific heat curves in figure 6.11 and from the inflection point of $\chi_{DC}(T)$ curves in figure 6.8. T_N stands for the temperature of the transition, delimited by the peaks of the specific curves in figure 6.11. Dashed lines are guide for the eyes.

In the phase diagram of figure 6.12 we plot the temperature T_N of the transitions in the specific heat curves. We also represent in the phase diagram the inflection points for the magnetic susceptibility curves in figure 6.8, which is given by the maximum value of the derivative $d\chi_{DC}/dT$. According to a well known result by M. A. Fisher, in an antiferromagnetic system, the temperature of such inflexion point is approximately equal to T_N [145], which shows to be consistent in our the phase diagram.

We analyse the dependence of the magnetic contribution to the specific heat with the temperature for $T < T_N$. In figure 6.13 we plot the $C_m(T)$ curve at $H=0$ T as a function of T^3 .

As we see, the low temperature portion of the curve is proportional to T^3 . The reason for this behaviour lies in the fact that the specific heat contribution of magnons in an antiferromagnetic system is proportional to T^3 , as we demonstrated in Chapter 2. From this fact we again have an indicative for the antiferromagnetic nature of the system.

Another feature of the specific heat curve in figure 6.13 is the slight deviation of the curve from the T^3 behaviour at low temperatures. As in some examples of antiferromagnets, such deviation may be an indicative for the existence of an energy gap in the spin-wave spectrum induced by an anisotropy [146–149].

We also calculate the magnetic contribution to the entropy by integrating $C_m(T)/T$, as given in the Chapter 2 by equation (2.80). Our result for the entropy calculated from the $C_m(T)$ curve at $H=0$ T is presented in figure 6.14.

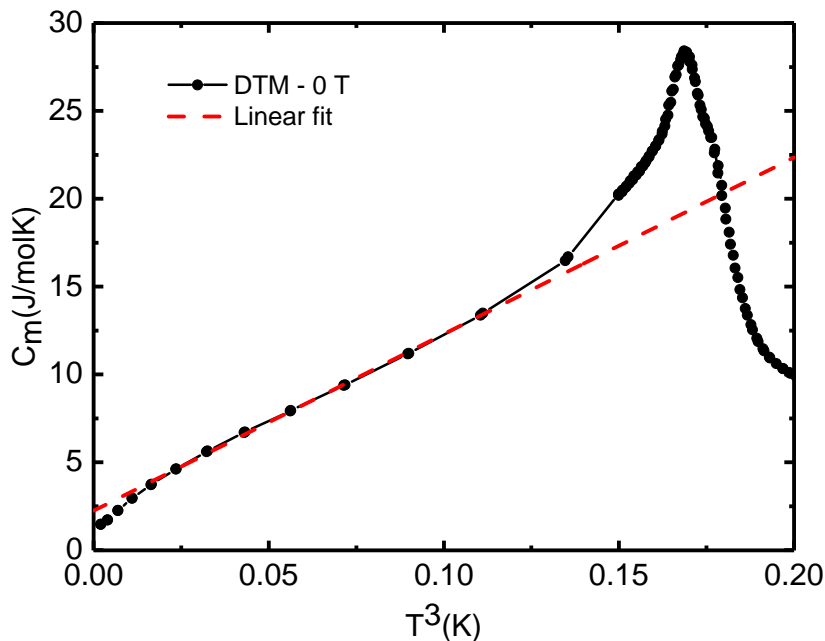


Figure 6.13: Magnetic contribution to the specific heat at $H=0$ T as a function of T^3 . The dashed red curve is a linear fit in the low temperature ($T < T_N$) portion of the $C_m(T)$ curve.

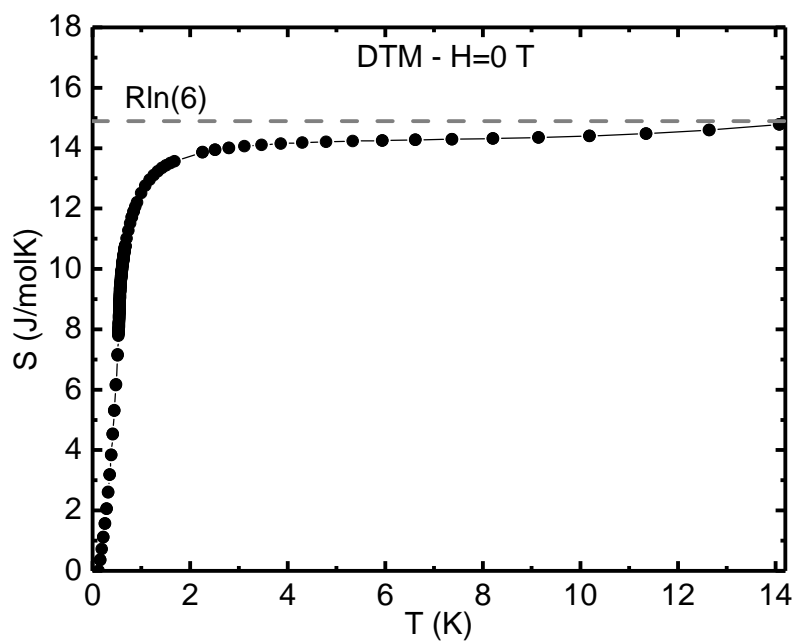


Figure 6.14: Magnetic contribution to the entropy obtained by integrating $C_m(T)/T$ for the specific heat curve at $H=0$ T .

In figure 6.14, we see that the magnetic contribution to the entropy, saturates at the value $S = R \ln(6)$. According to equation (2.82) from Chapter 2 it corresponds to the value for the entropy of an ideal paramagnetic system with $S = 5/2$. Then we conclude that all the magnetic contribution to the entropy was taken into account in the $C_m(T)/T$ integration.

Finally, regarding the two peak structure in our specific heat curves, we would like to mention the existence of other examples in literature for compounds that exhibit two sharp anomalies in the specific heat. We highlight some examples: the metal dihalides compounds MnCl_2 [150, 151] and NiI_2 [152]; also $\text{NiCl}_2 \cdot 2\text{H}_2\text{O}$ [153, 154], and $\text{NiBr}_2 \cdot 2\text{H}_2\text{O}$ [155]; the related compounds to the ones we study $\text{NiBr}_2 \cdot 6\text{SC}(\text{NH}_2)_2$ [156], $\text{NiI}_2 \cdot 6\text{SC}(\text{NH}_2)_2$ [157] and the frustrated Ising system $\text{CoCl}_2 \cdot 2\text{SC}(\text{NH}_2)_2$ [158]; the compound $\text{K}_2\text{PbCu}(\text{NO}_2)_6$ [159].

One explanation for such double peak behaviour in the specific heat curves is a partial ordering of the spins, then followed by the full ordering of the spins at a lower temperature. In the case of MnCl_2 and $\text{K}_2\text{PbCu}(\text{NO}_2)_6$ it is suggested that the existence of next-nearest neighbours interactions and their competitions with the nearest neighbours interactions leads to the partial ordering at certain temperatures and a subsequent full ordering of the spins for lower temperatures. This competition can also lead to different spin structures like different types of antiferromagnetic ordering or even helimagnetic ordering, and the two peaks can be related to the transition between different types of ordering. Also, the possibility of a structural phase transition can be considered to explain the nature of one of the peaks. In order to investigate which picture happens in DTM, our results urge for neutron scattering measurements to account for the amount of ordered magnetic moment and for the structure at low temperatures.

6.4 Results from specific heat measurements for DTF

In this section we present the results for the specific heat of DTF for different orientations of the crystal and under different values of external magnetic field, as shown in figures 6.15 for the total specific heat and figure 6.16 for the magnetic contribution. Confirming our magnetic susceptibility measurements, no indicative of magnetic ordering is observed down to 0.1 K.

From the curves of the magnetic contribution to the specific heat we see that they display a broad maximum, which shifts for higher temperatures the higher the value of the external magnetic field. We identify the existence of such maxima as Schottky anomalies, from fitting these curves with the multi-level Schottky expression (2.79) from Chapter 2 taking into account five energy levels, since it is expected for Fe^{2+} ion the existence of five energy levels, in a simplified scheme with a zero-field splitting and external magnetic field as depicted in figure 6.17

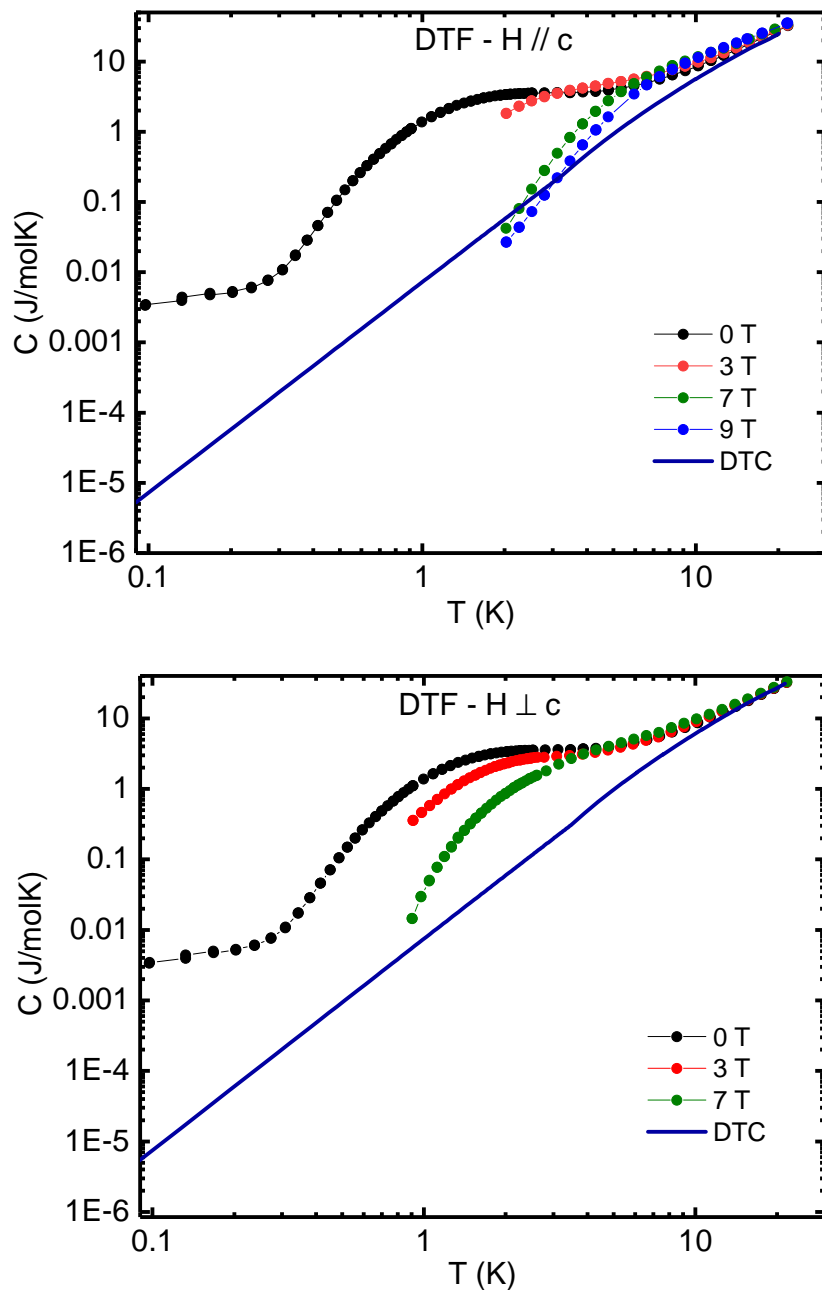


Figure 6.15: Total specific heat measured for DTF for several values of external magnetic field applied in parallel (top panel) and perpendicular (bottom panel) to the c -axis orientation. In both figures we compare the measured curves with the specific heat measurement of the specific heat measurement of DTC compound.

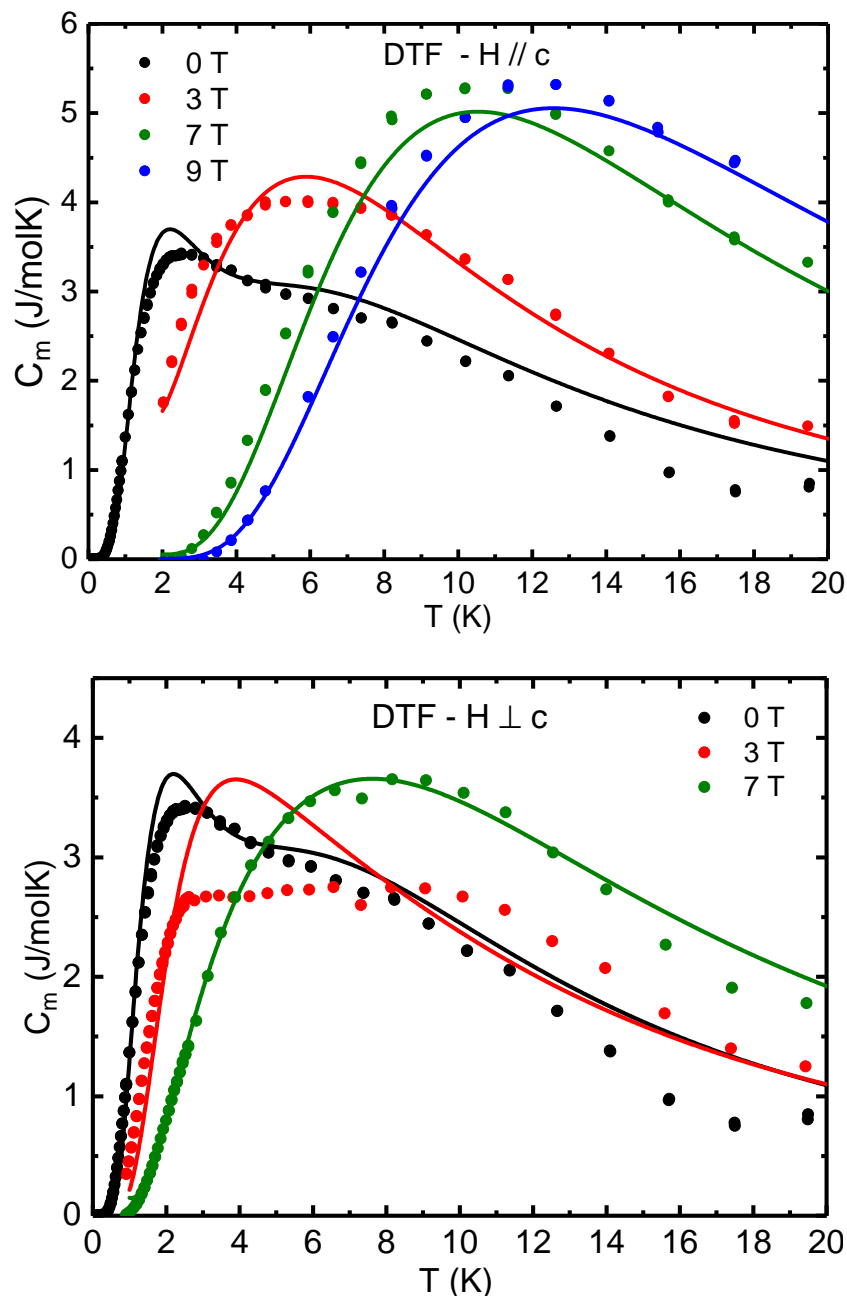


Figure 6.16: Magnetic contribution to the specific heat of DTF for several values of external magnetic field applied in parallel (top panel) and perpendicular (lower panel) to the c -axis orientation. These data were obtained after subtracting the lattice contribution, obtained from the specific heat of DTC compound, from the total specific heat curves presented in figure 6.15. Solid lines are adjust obtained from the expression (2.79) for the Schottky anomaly of specific heat.

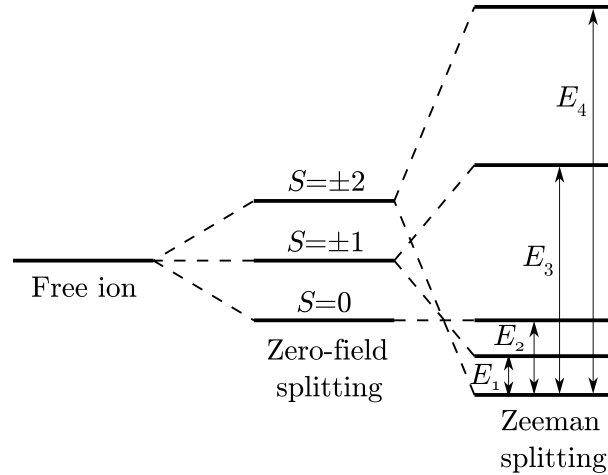


Figure 6.17: Simplified energy level scheme for a Fe^{2+} ion, taking into account the zero-field splitting and the Zeeman splitting due to the application of an external magnetic field.

In figure 6.18 we present the energy levels of DTF as a function of the external magnetic field, estimated from fits of the Schottky model for the specific heat curves in figure 6.16. The E_i energies presented in figure 6.18 account for the difference between a certain energy level and the lowest energy level, as represented in figure 6.17.

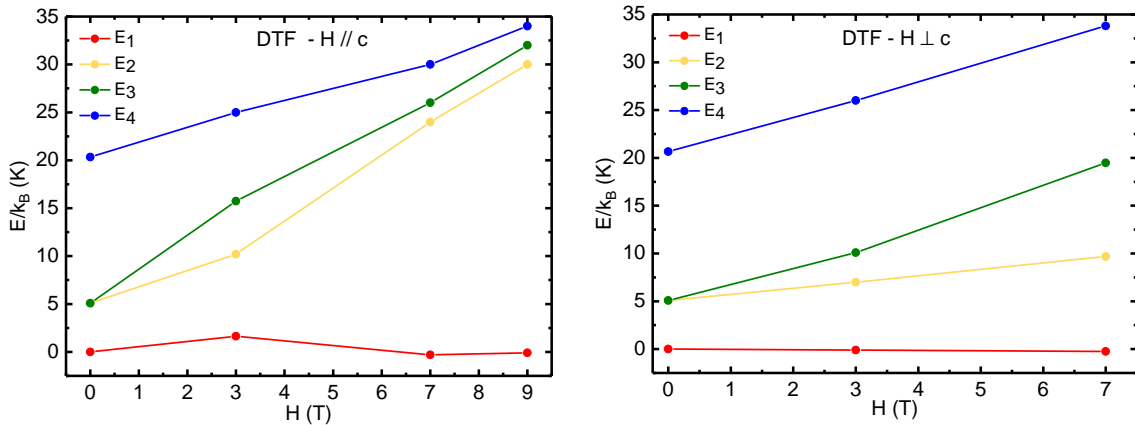


Figure 6.18: Energy levels of DTF as a function of the external magnetic field obtained from multi-level Schottky fits to the magnetic contribution of the specific heat, for the applied field parallel to the c -axis (left panel) and perpendicular to this axis (right panel).

We see from figure 6.18 that the energy levels present, in a good approximation, a linear behaviour as a function of the magnetic field, which is due to the Zeeman splitting.

As in the previous section, we calculate the magnetic contribution for the entropy of DTF for the specific heat curve at $H=0$ T. Our result is shown in figure 6.19.

Unlike the entropy curve for DTM, the curve of magnetic contribution to the entropy of DTF does not saturate to the value for the entropy of an ideal paramagnetic system with $S = 2$, but for a smaller value. The main reason for this fact is due to the absence of a phase transition in DTF in the range of temperature studied.

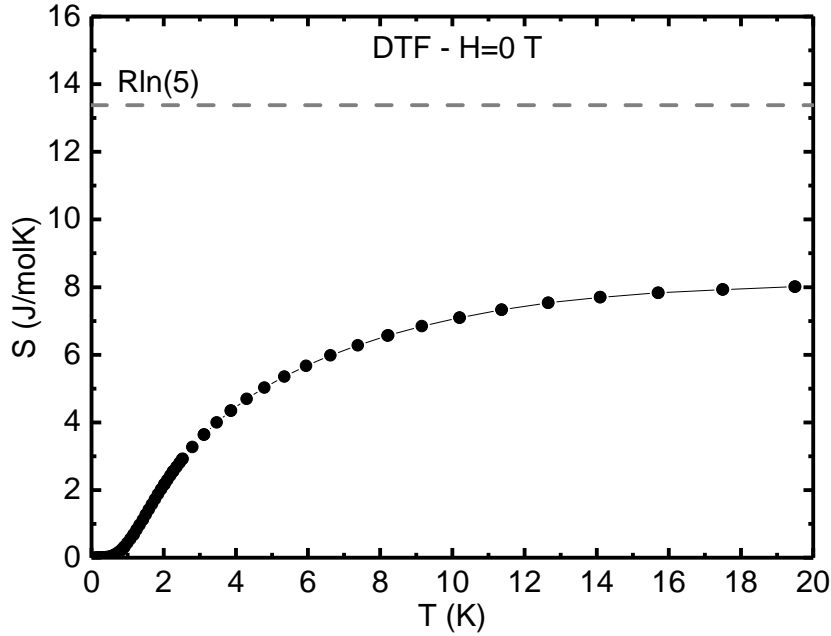


Figure 6.19: Magnetic contribution to the entropy obtained by integrating $C_m(T)/T$ for the specific heat curve at $H=0$ T.

Despite the value of $\theta_{CW} = 10.15$ K for DTF, we do not see any indicative of magnetic ordering down to 100 mK, which makes this compound a candidate for magnetic frustration, with a frustration parameter $f = |\theta_{CW}|/T_N > 100$. More studies, specially neutron scattering, are necessary in order to confirm the possibility of magnetic frustration in this compound.

6.5 Considerations about the exchange interactions in DTM and DTF

Due to the lack of works dedicated to determine the exchange interactions in DTM and DTF compounds some of our results cannot be fully understand and some few questions are still opened. On the other hand, some of our results help to extract some informations about such interactions.

First, from magnetization measurements (see figures 6.3 and 6.4) for external magnetic fields applied along the c -axis and along two directions perpendicular to it, we verify that along these two directions perpendicular to the c -axis the magnetization measurements display the same behaviour. Such results are seen in both DTM and DTF compounds. Also, taking into account that for both compound the distance between two magnetic ions along the a -axis and b -axis are equal ($a = b = 13.760$ Å for DTM and $a = b = 13.708$ Å for DTF) we conclude that the strength of exchange interactions along both a -axis and b -axis should be equal, namely J_{ab} , but different from the exchange interactions J_c along the c -axis.

Since DTM and DTF are face-centered structure, we may also consider a interaction J_f among the atoms in a corner and in the center of a face of the unit cell. Such interaction may not be non-negligible comparing to J_{ab} and J_c .

In figure 6.20 we depicted a simplified representation of DTM and DTF structure with the aforementioned exchange interactions.

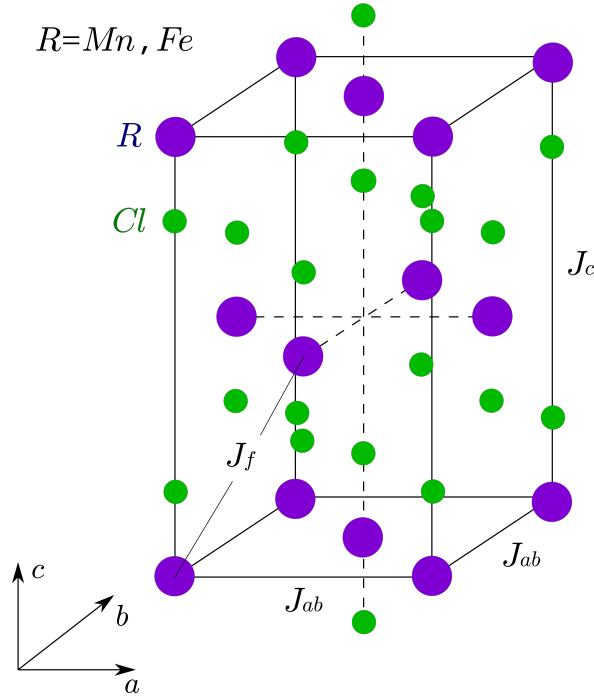


Figure 6.20: Simplified representation of DTM and DTF structure. J_{ab} are the exchange interactions along a and b -axis, J_c is the exchange interaction along the c -axis and J_f is the interaction among atoms in a corner and in the center of a face of the unit cell. Purple spheres represent Mn or Fe atoms while Cl atoms are represented by green sphere. S,C,N and H atoms were omitted for clarity.

Recalling table 6.1, where we summarize our estimates for the exchange interactions for measurements with field applied parallel ($H \parallel c$) and perpendicular ($H \perp c$) to c -axis, we observe some puzzling results which the explanation to then remains open. These results regard the estimation of J for DTF for both $H \parallel c$ and $H \perp c$. In principle, due to smaller distance among the magnetic ions along to the c -axis ($c = 8.940 \text{ \AA}$) comparing to the distance between two magnetic ions along the a -axis and b -axis ($a = b = 13.708 \text{ \AA}$) and also the disposition of Cl atoms along the c -axis, which leads to superexchange interactions along such axis, we would expected a larger value for J in the estimate for $H \parallel c$ measurements rather than for $H \perp c$ measurements. However we observe the opposite scenario, with the $H \perp c$ measurements more than 10 times larger than the $H \parallel c$ measurements and we are still working for interpret such results.

Another feature that deserves more studies, concerns on the double peak structure of specific heat in DTM. As mentioned, two transitions are also observed other compounds, including in a related compound to DTM, the MnCl_2 . In this compound some neutron

measurements [160] revealed that the contribution of second and third-neighbour interactions are also relevant and may lead to different spin structures like different antiferromagnetic orderings and helimagnetism. The relevance of such high order interactions in this compound is explained by an intricate combination of different mechanism of superexchange interactions. So, some similar study is necessary for DTM in order to explain the nature of the two transitions.

Finally, the absence of magnetic ordering in DTF for temperatures down to 100 mK and the its value for $\theta_{CW} = 10.15$ K, may suggest the existence of strong magnetic frustration in this compound. A non-negligible contribution (if we compare with J_{ab} and J_c) of J_f interactions among the atoms in a corner and in the center of the face of the unit cell, as represented in figure 6.20, may lead to frustration in this compound.

6.6 Conclusions

Through magnetization, magnetic susceptibility and specific heat measurements we studied the parent compounds of DTN, named DTM and DTF. We estimate the exchange couplings J , single-ion anisotropy parameter D and gyromagnetic factor g for these compounds through Curie-Weiss law and mean field fittings in magnetization curves.

From magnetic susceptibility and specific heat measurements for DTM we verify the existence of sharp peaks in the curves of these measurements, which are associated to antiferromagnetic transitions. In some specific heat curves we observe the existence of two transitions, which may be related to a partial, followed by a full ordering of the magnetic moments, as well as transitions between different spin structures or a structural phase transition followed by a magnetic ordering. Neutron scattering measurements are needed in order to corroborate these hypothesis.

For the DTF compound, no transition was observed for temperatures down to 100 mK, despite its value for $\theta_{CW} = 10.15$ K, making this compound a candidate for strong magnetic frustration, with a frustration parameter $f = |\theta_{CW}|/T_N > 100$. Again, in order to verify this issue further experiments are needed, specially neutron scattering.

Chapter 7

Magnetic susceptibility studies on Br-doped DTN

The aim of this chapter is to present our preliminary results of AC magnetic susceptibility of Br-doped DTN samples $\text{NiCl}_{2x}\text{Br}_{2(1-x)}\cdot 4\text{SC}(\text{NH}_2)_2$ with different amounts x of the dopant. From our results we were able to construct a three-dimensional BEC phase diagram relating the temperature, magnetic field H and the percentage of bromine in the system and compare our results with previous measurements. Although some few magnetic studies were performed in Br-doped DTN samples [24, 25, 161–166], to the best of our knowledge, no phase diagram obtained from magnetic measurements relating the temperature, critical magnetic field and bromine percentage was presented so far.

7.1 Disorder in quantum magnets and Br-doped DTN

In many systems in condensed matter physics, from basic research to technological applications, disorder is an unwanted feature. Specially in the study of phase transitions, disorder can prevent the occurrence of symmetry breaking and consequently suppress the existence of phases in the system [167].

It turns out to be that, specially in quantum systems, the effects of disorder can lead to unexpected behaviours. An important example was proposed by P. W. Anderson in 1958 where he considered the behaviour of electrons in a crystal with the tight-binding model with a random potential. He showed that, even in the absence of interactions, the localization of the wave functions is observed [168]. Since that, it has been discussed if such mechanism can also describe the metal-to-insulator transition in some materials [169].

The effects of disorder have been also studied in bosonic systems. In the Bose-Hubbard model, an analogous of the Hubbard model, it was shown that disorder in a bosonic system leads to the suppression of the global phase of the system and the formation of localized and isolated superfluid clusters of different sizes, the so-called *Bose-Glass* (BG) phase [17, 170, 171]. Some efforts have been made in order to verify the scaling laws relating the critical exponents and the universality class of bosonic disordered systems [167, 172], both

theoretically and experimentally in studies with bosons in optical lattices [172], superfluid helium in porous media [173] and in quantum magnets [174].

Regarding quantum magnets, disorder can be created either by site dilution, where the magnetic ion is replaced by a non-magnetic ion, or bond dilution, where the ligand atoms are replaced by other element. Some examples of materials where the effects of disorder have been studied are the IPA-CuCl_{3-x}Br₃ [26–28, 38], Tl_{1-x}K_xCuCl₃ [29–32] and the DTN [17].

In the case of DTN, both site and bond dilutions have been studied in the past few years. The site dilution consist in the replacement of some Ni ions by Cd ions [175], while in the bond dilution some Cl atoms are replaced by Br atoms. Most of studies of disorder in DTN focus on the Br-doped DTN, NiCl_{2x}Br_{2(1-x)}-4SC(NH₂)₂.

From magnetic and specific heat measurements in 8% ($x=0.08$) Br-doped DTN, R. Yu *et al* [24] showed that the doping is responsible for the lowering of H_{c1} . This happens because the substitution of Cl by Br atoms locally increases the exchange couplings. As shown in Chapter 2, the gap depends on the exchange couplings, which means that the Br doping in DTN tends to lower the gap. The authors also found that the exponent ϕ , which relates the critical fields and temperature as $T_c \sim |H - H_c|^\phi$, is $\phi = 1.1$ for the Br-doped DTN. This value is consistent with the predictions for the BG-to-BEC transition and the results of this work are in a good agreement with QMC calculations. Finally, the authors present the first experimental evidence of a *Mott-Glass* phase, where the susceptibility, which is related to the compressibility of a Bose gas, vanishes despite the locally gapless spectrum.

Also, some neutron scattering studies [161] as well as specific heat measurements [162,163] for some Br-doped DTN with different amounts of Br indicates that the gap closes, when $H=0$ T, for a Br content around 20%.

Finally, some Nuclear Magnetic Resonance (NMR) measurements combined with QMC calculations in a 13% Br-doped DTN identified the resurgence of a quantum coherence which implies in a *disorder-induced* BEC phase right after the critical field H_{c2} for a maximum temperature around 200 mK [164–166].

In our work we performed AC magnetic susceptibility measurements of Br-doped DTN for different dopant amounts and we built a phase diagram relating the critical magnetic field and temperature for the occurrence of the BEC phase with the percentage of the bromine dopant.

7.2 Results

In this section we present our results of AC magnetic susceptibility measurement as a function of external magnetic fields up to 5 T and temperatures down to 0.55 K for our Br-doped DTN samples.

The results of these measurements are presented in figure 7.1 for several temperatures from 0.55 K to 1.10 K. The kinks in the χ_{AC} curves, which marks the existence of a

transition to an ordered state, are indicated by arrows. In some curves the position of the kink was not clear at first sight. So, to determine the kinks we observe that right before and after the region where the kink is located the χ_{AC} curves display a nearly linear behavior. So we use the technique from reference [50] which consist in drawing straight lines in these linear region and extrapolate them. Finally we identify the kink as the crosspoint of these two lines. An example of the application of this technique is presented in figure 7.1 for the $\chi_{AC}(H)$ curve measured for the 3.3% Br-doped sample at 0.55 K.

Once we determine the value of the field H_{c1} , which marks the position of the kink for each $\chi_{AC}(H)$ curve we are able to construct a three-dimensional phase diagram for DTN relating the critical temperature and field for the occurrence of the BEC phase with the percentage of Br in the sample. This phase diagram is presented in figure 7.2.

From the panels of figure 7.1 and the phase diagram of figure 7.2 we see that increasing of Br impurities lowers the critical field necessary to achieve the BEC phase. In other words, for measurements of samples with different percentages of dopant performed at a certain temperature, the higher the amount of Br in the sample, the lower the external magnetic field necessary to achieve the BEC phase.

Also, we compare our results with previous measurements. In figure 7.3 we display the curves from figure 7.2 together with Br-doped DTN phase diagrams for a Br content of 8% and 13%, obtained from $\chi_{AC}(H)$ measurements by Professor A. Paduan-Filho, and specific heat measurements in 21% from references [162, 163].

From the comparisons in figure 7.3, we verify the consistency of our results with the previous measurements, since the grater the amount of Br in the sample, the smaller the critical field necessary to close the gap. Specially for our 8.8% Br-doped sample, we see that, as expected, its phase diagram is nearly the same phase diagram for the 8.0% Br-doped sample provided by Professor A. Paduan-Filho.

A clearer way to show these consistencies is presented in figure 7.4, where we selected the value of H_{c1} from each phase diagram presented in figure 7.3 at 0.6 K and 0.8 K and plotted as a function of the Br content. For the 13% and 21% curves the value of H_{c1} was taken at 0.63 K, and also for the 21% we take the value of H_{c1} at 0.84 K.

We see in figure 7.4 that the critical field H_{c1} as a function of Br content displays a linear behaviour, in a good approximation, except for the 21% curve at 0.63 K, where the gap closes. The determination of a linear tendency of the critical field H_{c1} as a function of the Br content may be useful for an alternative determination of the Br content in the samples in further measurements.

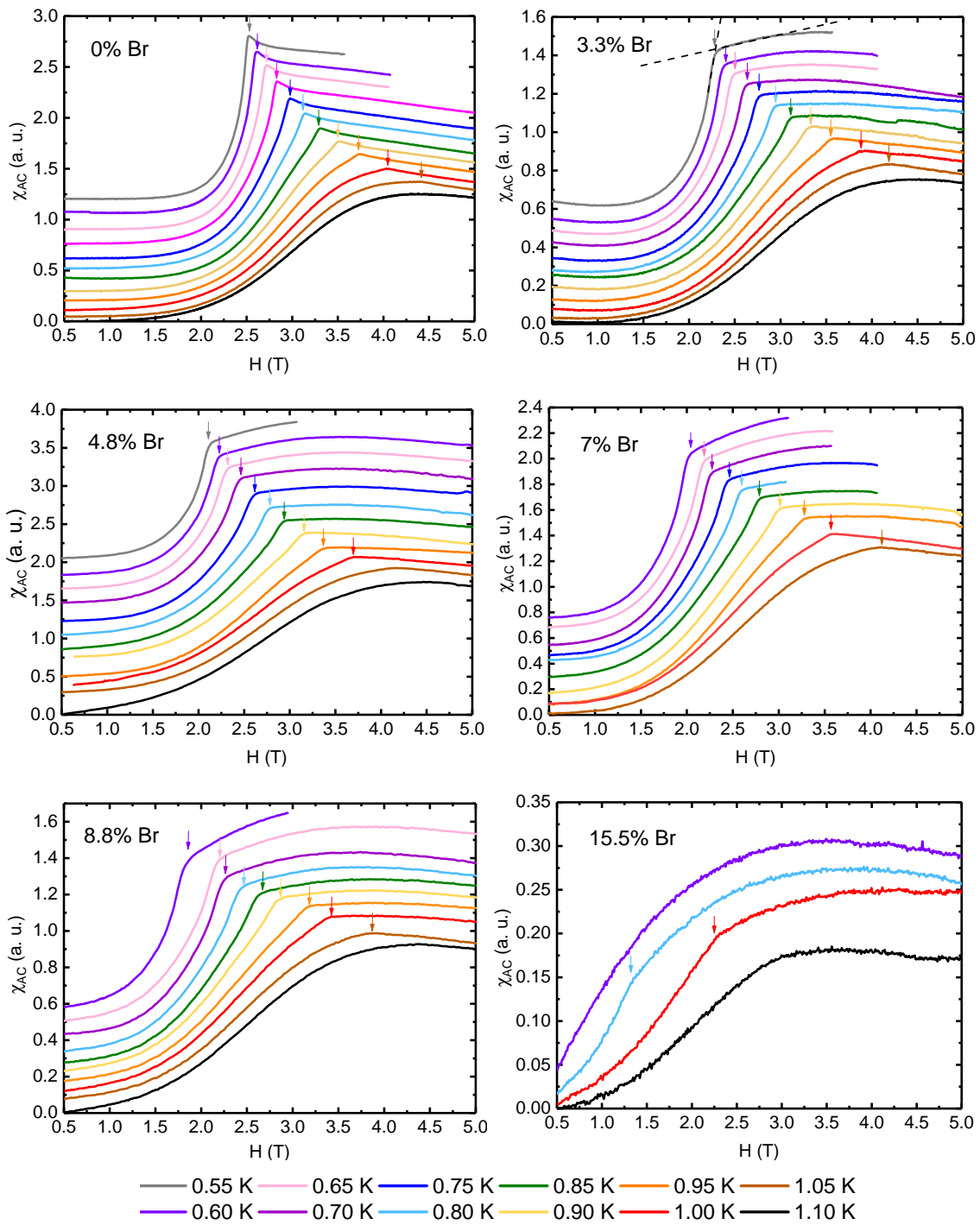


Figure 7.1: AC magnetic susceptibility measurement as a function of the external magnetic field for Br-doped DTN samples in different concentrations of bromine. The arrows indicate the position of the kink in the $\chi_{AC}(H)$ curves (see text). The curves were shift vertically for clarity.

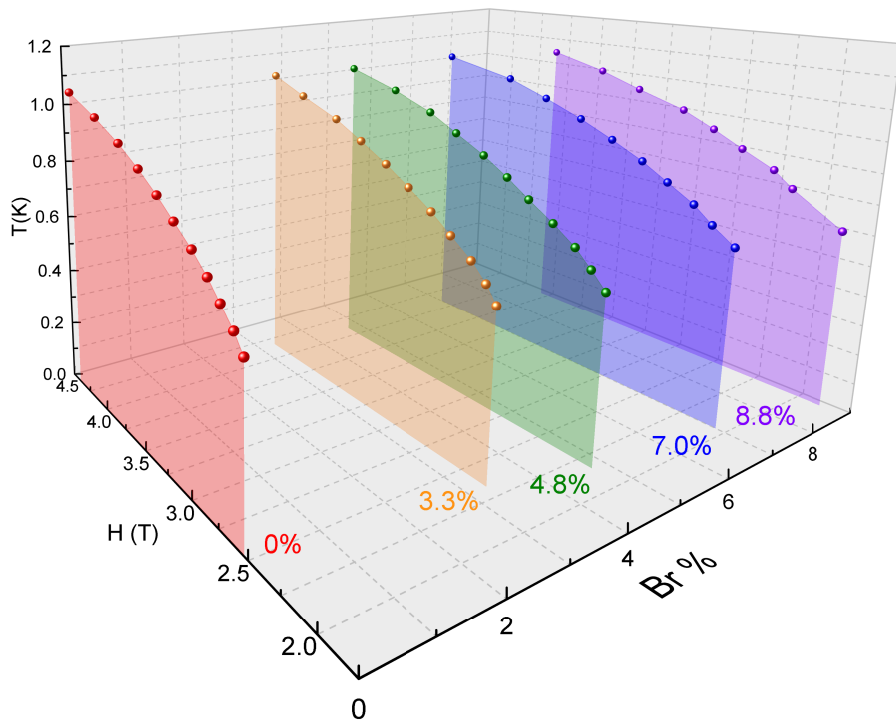


Figure 7.2: Phase diagram of Br-doped DTN obtained from the position of the kinks from the curves presented in figure 7.1. For a better visualization of the results, the axis of the applied external field is arranged in decreasing order.

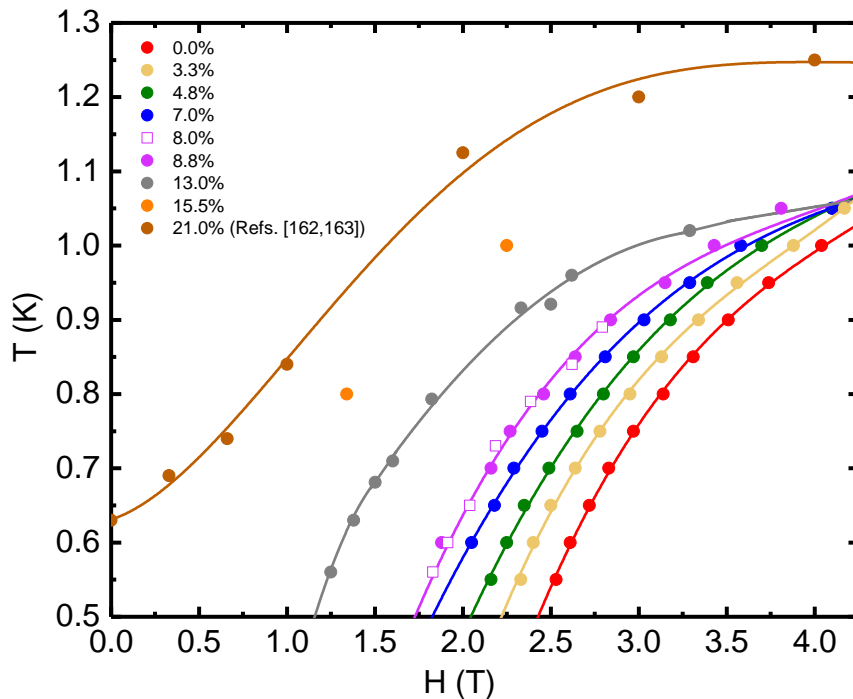


Figure 7.3: Phase diagrams for Br-doped DTN samples comparing with previous AC magnetic susceptibility measurements for Br contents of 8% and 13%, provided by Professor A. Paduan-Filho, and for 21% from specific heat measurements from [162,163].

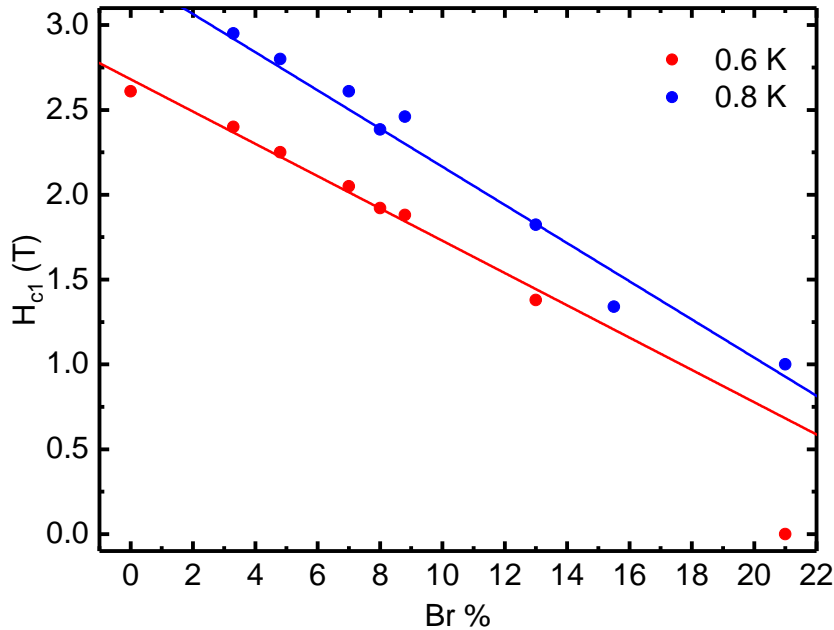


Figure 7.4: Critical field H_{c1} as a function of the Br content at 0.6 K and 0.8 K, obtained from the phase diagrams in figure 7.3. The value of critical field for samples with 13% and 21% Br content was taken at 0.63 K and also for the sample with 21% of Br the value of H_{c1} was taken at 0.84 K.

To understand these results is important to remember that the energy gap Δ between the $S^z = 0$ and $S^z = 1$ levels in DTN is given by [62]

$$\Delta = D - 2J_c - 4J_{ab}. \quad (7.1)$$

The reason for the lowering of the critical field is due to the fact that the Cl and Br atoms are responsible for the superexchange interactions among the Ni ions. Since the presence of Br atoms modify the strength of such interactions and also the single-ion anisotropy, it modify the size of the gap and this can promotes the closing of the gap for sufficient high amounts of Br in the sample. As mentioned before and displayed in figure 7.3 such amount is around 20%.

In the aforementioned studies, determination of the exponent ϕ is made in the portion of the phase diagram for temperatures below 0.5 K. Since in our experimental setup we can achieve temperatures down to 0.55 K, the determination of such exponent is not possible. We expect that, in a future work, we can perform magnetic measurements of these samples in lower temperatures in order to determine such exponent.

7.3 Conclusions

In this chapter we presented our preliminary results about AC magnetic susceptibility in Br-doped DTN samples with different amounts of the dopant. Our measurements corroborate some studies where it is shown that the larger the amount of Br doping in the

system, the lower is the critical field H_{c1} for the occurrence of the BEC phase due to the reduction of the energy gap [24, 161, 163].

A similar phase diagram to the one in figure 7.2 was presented in reference [163] but for specific heat measurements. To the best of our knowledge our phase diagram is the first one obtained from AC magnetic susceptibility measurements that relates the critical magnetic field, the critical temperature and the bromine content in the Br-doped DTN samples.

We also compared our results with previous measurements and verify that the critical field H_{c1} as a function of the amount of Br dopant present a linear behaviour for some temperatures.

Since the lower temperature achieved in our experimental setup is around 0.55 K, the determination of the exponent ϕ was not possible. We hope to perform further AC magnetic susceptibility measurements in lower temperatures and higher magnetic fields to obtain the critical exponents as well as the full phase diagram.

Chapter 8

Preliminary studies on pressure in DTN

In this chapter we discuss our preliminary studies on the influence of pressure in DTN samples. First we review a study about the influence of pressure in Muon Spin Relaxation and Inelastic Neutron Scattering measurements in DTN. Then we discuss some details regarding the hydrostatic pressure cells used in the MPMS-SQUID and in the 20 T cryostat, from which we performed magnetization measurements for different applied pressures up to 7.6 kbar. Finally we present our experimental results combined with mean-field theory and our estimate for the critical pressure p_c necessary to close the energy gap and so promote a pressure-induced antiferromagnetic phase. Although the reproducibility of our results need to be verified for pressures up to 3 kbar, our estimate of p_c is very close to earlier results obtained from thermal expansion and magnetostriction measurements.

8.1 Effect of pressure in field-induced antiferromagnets

In the previous chapter we presented our results of magnetic measurements of DTN and its phase diagram for the pure and Br-doped samples. We saw that the existent gap between the non-magnetic ground state and the excited state in DTN can be closed either by applying an external magnetic field or by Br-doping, modifying the strength of exchange couplings and the single-ion anisotropy term.

However there is a third alternative for closing the gap in field-induced antiferromagnets by means of applying pressure to the system.

Studies on some field-induced antiferromagnets like TlCuCl_3 [33–37], IPA-CuCl_3 [38], PHCC [39] and CsFeCl_3 [40], showed that applying pressure by means of pressure cells can close the gap between the non-magnetic state and the excited state, achieving a pressure-induced antiferromagnetic phase. The reason for this closing of the gap relies on the fact that compression of a crystal shortens the atomic distances, increasing the strength of the exchange interactions. Since the size of the gap depends on the exchange interactions, as shown in equation (2.22) for DTN, applying pressure tends to reduce the gap or, for high

enough pressures, even close it.

A fundamental difference between field-induced and pressure-induced phase transitions regards the universality class of the quantum critical point (QCP) associated with these transitions. In the theory of phase transitions one of the defined critical exponent is the so-called *dynamical exponent* z , related to the power-law of the single-particle dispersion relation at long wavelengths at the QCP as $\omega_k \sim k^z$.

In the case of the BEC QCP we have $z = 2$. However, the pressure-induced QCPs belongs to another universality class, where $z = 1$ [17, 176]. It means that these antiferromagnetic systems provide a very interesting opportunity for studying different universality classes by varying some physical parameter as external magnetic field or applied pressure, each at once or even both at same time, which may lead to more intricate phenomena.

For DTN the existence of pressure-induced phase was recently investigated from Muon Spin Relaxation (μ SR) experiments at zero applied field [162]. In these experiments, powdered DTN was pelletized and inserted in hydrostatic pressure cells. Then, the procedure to measure the samples under pressure consisted in applying a high pressure, up to 22 kbar, to the cell and perform a μ SR measurement. Later, the pressure was partially released and a new μ SR measurement was performed. This procedure was repeated until zero pressure.

In this study it was shown that, for applied pressures around 2.3 kbar, a pressure-induced antiferromagnetic ordering is present in DTN and the transition temperature increases the higher the applied pressure. The pressure-induced phase diagram for DTN obtained in these experiments is presented in figure 8.1.

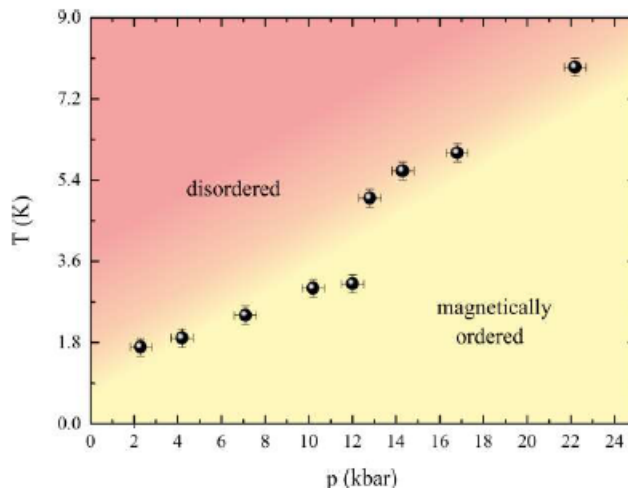


Figure 8.1: Pressure-induced phase diagram of DTN obtained from Muon Spin Relaxation (μ SR) experiments at zero applied field. The points denote the observed ordering temperature T_N in DTN as a function of pressure. This figure was adapted from reference [162].

Since an antiferromagnetic ordering was identified for applied pressures around 2.3 kbar, it was expected the closing of the energy gap for pressures from such value. In order to verify it, some Inelastic Neutron Scattering (INS) measurements were performed at 1.8 K

for applied pressures of 0 kbar and 4 kbar without applied magnetic field. These results are presented in figure 8.2.

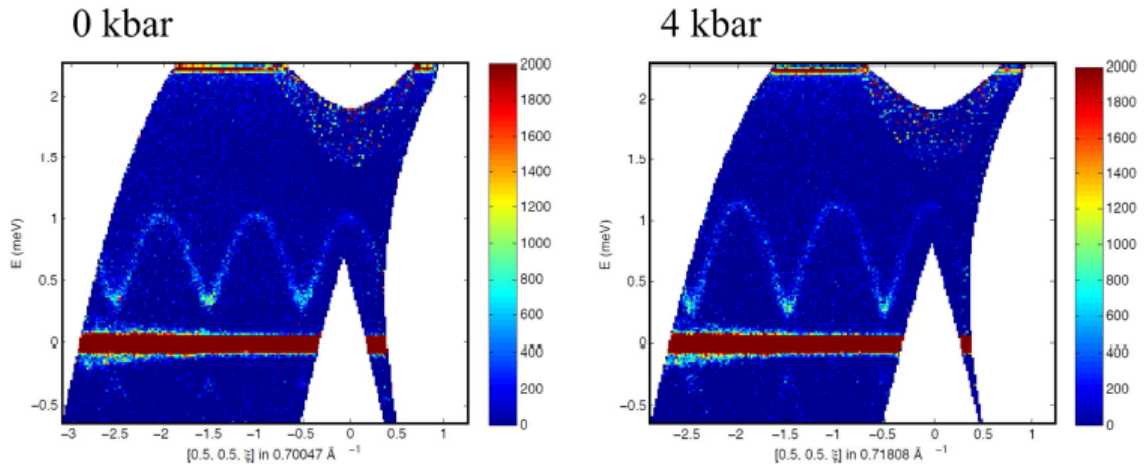


Figure 8.2: Inelastic Neutron Scattering (INS) measurements for DTN at 1.8 K for applied pressure of 0 kbar (left panel) and 4 kbar (right panel). Both measurements were made without applied magnetic field. This figure was adapted from reference [162].

As we see from figure 8.2, for an applied pressure of 4 kbar, which presumably should be enough to close the gap, the gap lowers but still remains opened, since the brighter periodic blue curve which represents the spin excitation spectra does not assume values of zero energy.

This apparent contradiction was explained from neutron diffraction studies, where it was shown that, for pressures above 8 kbar, DTN undergoes an irreversible structural transition from a structure belonging to the $I4$ space group to another structure from the $P4$ or $P4_2$ space group.

Since the μ SR measurements were performed by successively decreasing the pressure from an initial applied pressure higher than 8 kbar, the results presented in figure 8.1 does not represent the pressure-induced phase diagram for the $I4$ DTN structural phase but for its high pressure phase.

Although it was shown in reference [162] that for 4 kbar the DTN gap remains opened and also that for 8 kbar DTN undergoes an irreversible structural phase transitions, the possibility of pressure-induced phase transition for this range of pressures that precede the structural phase transition remains not explored, as well as the influence of pressure in the DTN phase diagram.

In our work we studied the effect of pressure in DTN by applying pressure to the samples using a hydrostatic pressure cell and measuring the magnetization under different applied pressures. In the case of AC magnetic susceptibility measurements, due to technical issues, we did not concluded such measurements.

8.2 Hydrostatic pressure cell

In this work many efforts were employed to measure the influence of hydrostatic pressure in magnetic measurements in DTN samples. For such study some models of hydrostatic pressure cell were built to be used in the MPMS-SQUID and in the 20 T cryostat.

In a hydrostatic pressure cell, a sample is inserted in a recipient containing some fluid, generally oil. The recipient is desirably made from a soft material, like Teflon, to allow deformation. In common assemblies for a pressure cell, this recipient is pushed by one or two pistons. The pressure made by the pistons is homogeneously transferred to the sample by means of the fluid that permeate it. Since, in general, a pressure of the magnitude of a GPa is applied to the cell, their parts should be made from materials which sustain high pressures. So then, the most common materials used to make a pressure cell are cooper-beryllium (CuBe) alloys or tungsten carbide, due to the strength of these materials in dealing with high pressures.

The advantages of using CuBe in to produce pressure cells lies in the fact that these alloys are able to sustain high pressures and presents low magnetic signal. The CuBe alloy used in this work display at $T = 2$ K a signal in the order of magnitude of -10^{-9} emu/mg, which makes cooper-beryllium appropriate to build a pressure cell that gives a minimum contribution to the total signal measured during the experiments.

8.2.1 Hardening of CuBe

In this work we built our pressure cells from CuBe 25 (C17200). The hardness of CuBe alloys is enhanced after some heat treatment. So, we preferably acquired the material without heat treatment in order to make the manufacturing of the pressure cells easier. After the production of the components of the cell, we carried out with the hardening process.

The hardening process employed consists in heat the material up to 315° C (600° F) for 3 hours and cooling it [177]. We prepared two hardened samples, one left to cooled down naturally inside the oven after ramp the temperature down to the environment temperature and the other by quenching, which consisted in cool down the sample rapidly by drop it into water.

In order to infer the hardness of CuBe samples we performed Vicker hardness tests, which consists in deforming the samples by applying pressure using a press with a pyramid-shaped diamond tip. Then the hardness of the sample is calculated from the dimensions of the impressions made by the diamond tip in the material.

We verify that our CuBe samples without heat treatment display a hardness of 221(6) HV while the hardness of samples under heat treatment is 354(10) HV, which represents an increase of 62% in the hardness. Both hardened samples, from natural cool down and quenching, displayed no significant difference in their hardness value.

8.2.2 Designs for the pressure cell

In order to perform our magnetic measurements under pressure we develop some pressure cells to be used in the MPMS-SQUID based on models commonly used in such applications [178, 179]. In figures 8.3 and 8.4 we present, respectively, the schematic representation of our pressure cell and its photo. Due to the limitations in the sample space of MPMS the outer diameter of our pressure cells is 7.5 mm.

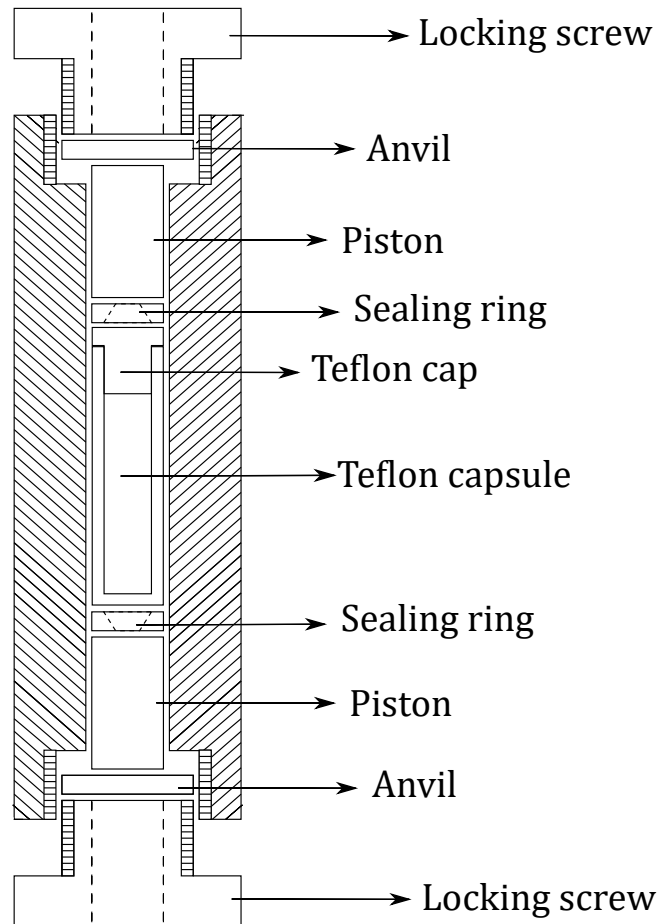


Figure 8.3: Schematic representation of a pressure cell.

We verify that in our cells we are able to achieve pressures up to 7.6 kbar. However, since the manufacturing of some pieces, specially the Teflon capsule, are hard due to their small size they present some imperfections making hard to achieve such pressures. These imperfections are responsible by the crashing of the capsules and the leaking of the pressure media, which was Kerosene in our experiments. These damages limited in many situations the maximum pressure achieved as about 3 kbar.

To infer the pressure applied in the cell, commonly a small piece of a superconducting material (in our case we used Pb or Sn) it is added with the sample, since the influence of the pressure on the superconducting temperature T_c is well known. So, since we measure the value of T_c from AC magnetic susceptibility measurements after applying the pressure to the cell, we know the value of the pressure acting on the sample.

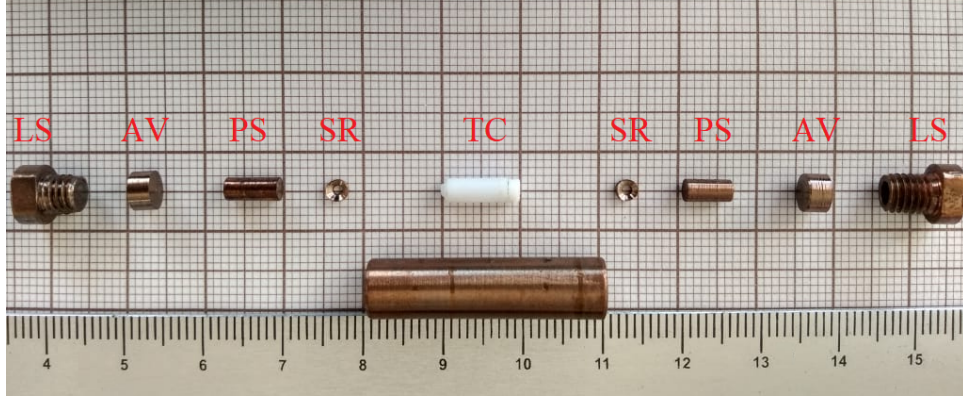


Figure 8.4: Parts of the pressure cell: Locking screw (LS), anvils (AV), pistons (PS), sealing rings (SR) and the Teflon capsule with the Teflon cap (TC).

Another problem faced regards the low magnetic signal of DTN samples ($M = 5.3 \times 10^{-4}$ emu at $H=0.5$ T and $T=1.8$ K). Although the CuBe signal is low, the total signal of the pressure cell is in the same order of magnitude of the DTN samples signal, making the centering of the sample and its measurements hard to perform. In figure 8.5 we compare the signal of a DTN sample with mass $m = 7.76$ mg and the signal of a pressure cell.

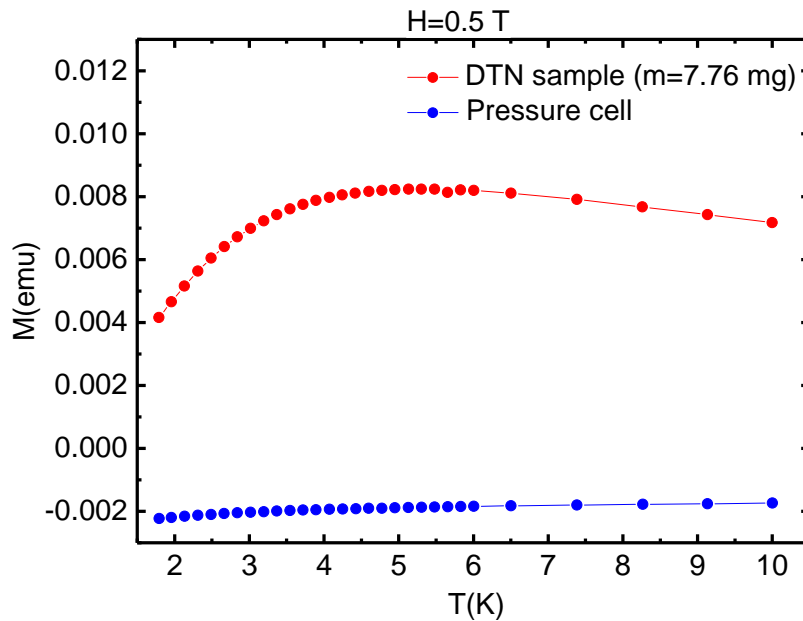


Figure 8.5: Comparison between magnetization measurements of a DTN sample with a mass of 7.76 mg (red curve) and an empty pressure cell (blue curve) under an external magnetic field of 0.5 T.

In another cryostat, with a larger sample space these hindrances could be overcome building a larger pressure cell with a system of pick-up coils, and even also primary coils, wrapped around the sample. In this case this assembly is inserted in the Teflon capsule and the coils wires come out from the cell by a feedthrough.

We developed several types of coils to be used in a larger pressure cell for our 20 T cryostat. These models include variations with and without a primary coil and secondary coils with single and two opposite windings. The larger pickup coil build, following the size limitation of the sample space, had 1760 turns of 44 AWG cooper wire and an inner diameter about 2 mm. In figure 8.6 we show an example of a pick-up coil.



Figure 8.6: An example of pick-up coils to be used inside a pressure cell.

Despite trying to measure DTN samples with these coils at low temperatures (down to 1.8 K) using the mutual inductance bridge method, we were not able to reproduce magnetic susceptibility measurements of DTN with this system, again due to the small signal of the samples. However, we succeed to measure the transition of a Sn sample with $m = 1.38$ mg to the superconductor state. In figure 8.7 we present a $\chi_{AC}(T)$ measurement made from such coil in which this transition can be seen.

We see in figure 8.7 that the reduction of temperature in the sample causes a decrease in the magnetic susceptibility which, around $T = 3.65$ K is abrupt, marking the transition to the superconductor state. This value is close to the reported value for this transition, $T_c = 3.72$ K.

It should be mention that these measurements are highly non-trivial to be performed, since we are simultaneously dealing with low temperatures, high magnetic fields, high pressures and samples with a low magnetic signal. Due to this difficulties we did not conclude this study.

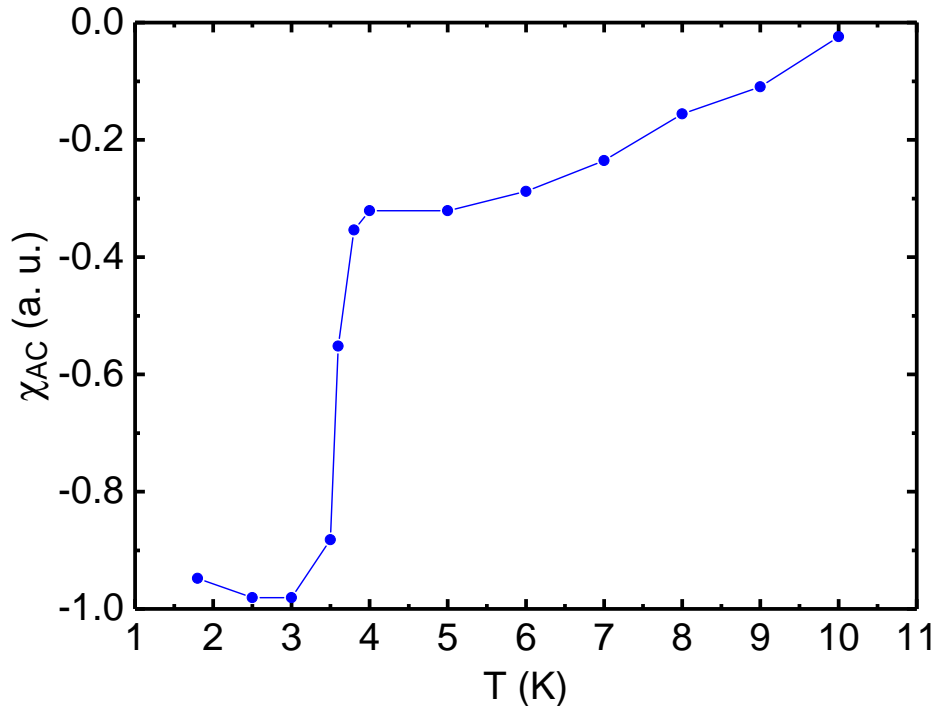


Figure 8.7: $\chi_{AC}(T)$ measurement (in arbitrary units) of a Sn sample made in a homebuilt pickup coil for a pressure cell at external magnetic field $H = 0$ T and AC excitation field $h_{AC} = 1$ Oe with frequency $f = 155$ Hz.

8.3 Effects of pressure in DTN

With help of our pressure cell design for use in MPMS-SQUID, we performed magnetic measurements of DTN samples under pressure. Due to the problems mentioned in the last section the maximum pressure achieved in our experiments was 7.6 kbar in one occasion. Since in many attempts the maximum pressure achieved was around 3 kbar, the reproducibility of the results presented in this section could not be verify for pressures higher than 3 kbar.

In these studies, a small piece of lead used as a barometer was glued to a DTN samples using GE varnish. After the application of pressure in the cell, we measured the AC magnetic susceptibility of the system at an external magnetic field $H = 0$ T and AC excitation field $h_{AC} = 1$ Oe with frequency $f = 155$ Hz. In this measurement we determined the transition temperature to the superconducting state T_c in the $\chi_{AC}(T)$ curves as the middle point between the onset of the transition and the first points in the lower portion of the $\chi_{AC}(T)$ curves.

The pressure in the system was inferred knowing that, in the case of lead, T_c as a function of the applied pressure p is given by [180]

$$\frac{\partial T_c}{\partial p} = -(3.61 \pm 0.05) \times 10^{-2} \text{ K/kbar.} \quad (8.1)$$

After determining the pressure, we performed magnetization measurements in the system under an external magnetic field $H = 0.5$ T. Since we use lead as a barometer, the magnetization measurements should be made for values H higher than $H = 0.08$ T, given that this is the critical field to observe the superconducting state in lead. For external fields higher than such value the superconducting state is suppressed and the magnetic signal of lead is low enough (10^{-5} emu/mg) to not interfere in the magnetization measurements of DTN.

In figure 8.8 we present our results of $\chi_{DC}(T)$ measurements for DTN under some applied pressure as well as the $\chi_{AC}(T)$ measurements to the determination of the T_c as a function of the applied pressure. We fit our $\chi_{DC}(T)$ DTN curves with the mean-field expression given by (6.1) in order to determine an exchange coupling J and the single-ion anisotropy parameter D as a function of the applied pressure.

We see from figure 8.8 (a) that the application of pressure shifts the temperature of the maximum in DTN curves to higher temperatures and makes it broader. Also we verify that the mean-field fits to the curves provide good agreement with the experimental data. For low temperatures, such agreement tends to diverges since this model is an approximation and does not take into account the intrachain interactions J_{ab} , which are relevant as lower the temperature.

Also, from figure 8.8 (b) we see that the application of pressure tends to lower the critical temperature for the superconducting transition of lead, as described by expression (8.1).

Once we estimate the exchange coupling J and the single-ion anisotropy parameter D from the curves in figure 8.8 (a), we studied how the magnitude of such parameters changes with application of pressure in the system. In figure 8.9 we present the estimate value for these parameters as a function of the applied pressure.

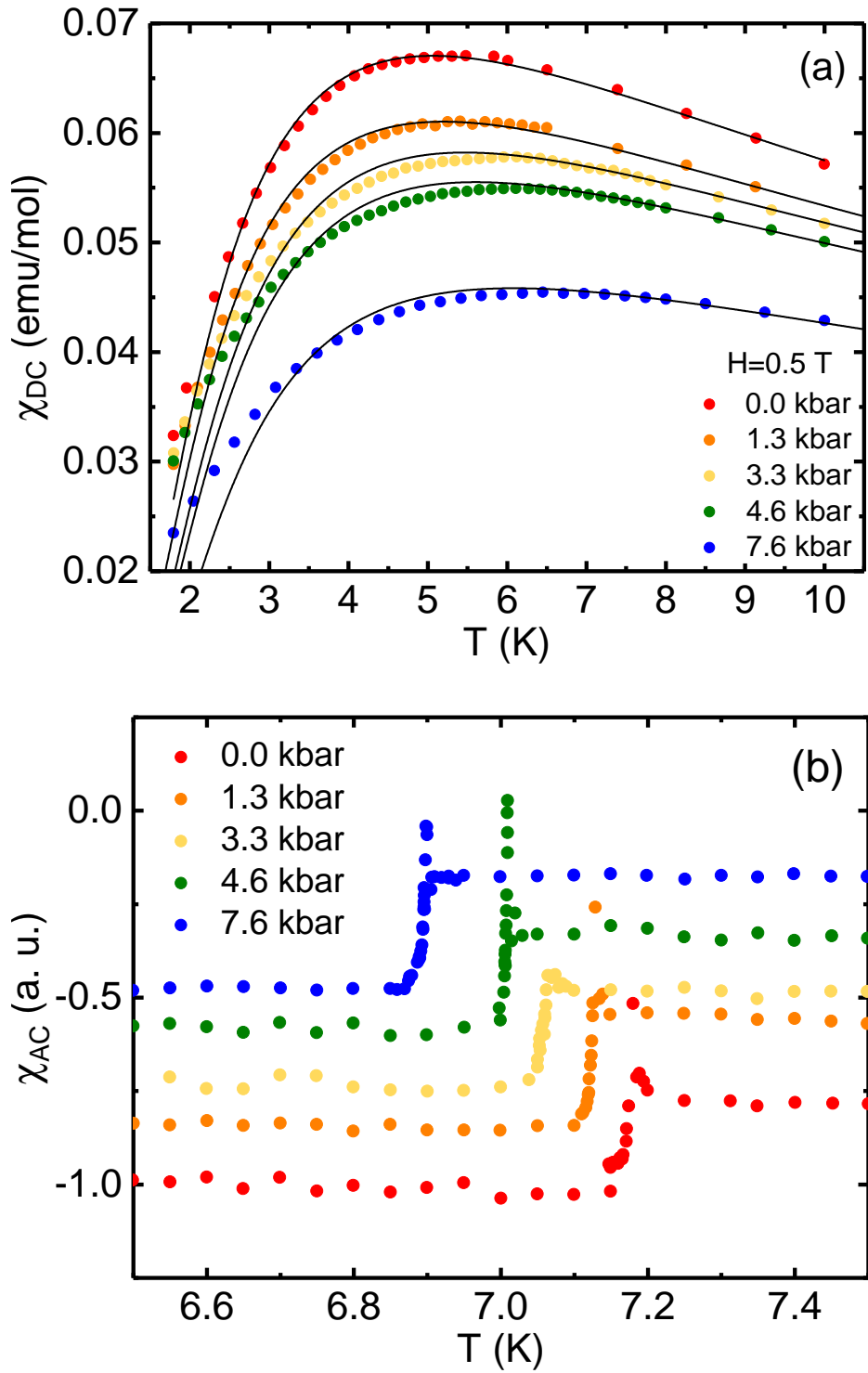


Figure 8.8: (a) $\chi_{DC}(T)$ at $H = 0.5$ T under several pressures. Continuous black lines are fits to the experimental data (colourful dots) using expression (6.1). (b) $\chi_{AC}(T)$ measurement (in arbitrary units) at external magnetic field $H = 0$ T and AC excitation field $h_{AC} = 1$ Oe with frequency $f = 155$ Hz. These curves were shifted vertically for clarity.

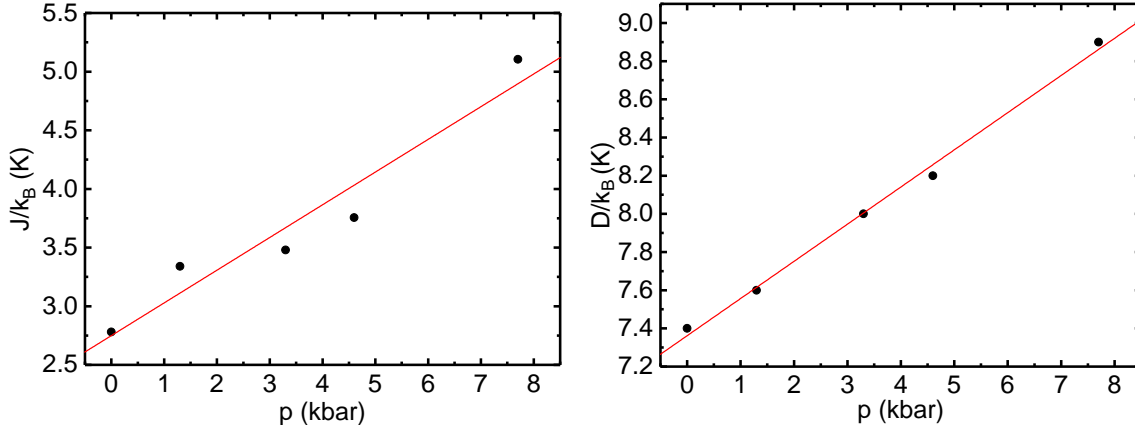


Figure 8.9: Values of exchange coupling J and single-ion anisotropy parameter D as a function of applied pressure p obtained from fits of curves in figure 8.8 using the mean field expression (6.1). Black dots are experimental data and red lines are linear fits to the experimental data.

As we see in figure 8.9, the value of both J and D parameters increases linearly, in a good approximation, with the increasing of pressure. From a linear fit of such data we were able to estimate the dependence of J and D as

$$J(p)/k_B = 0.28p + 2.75 \text{ K} \quad \text{and} \quad D(p)/k_B = 0.19p + 7.36 \text{ K}. \quad (8.2)$$

Knowing the dependence of J and D with pressure, we can estimate the critical pressure p_c necessary to close the gap and so promote a pressure-induced antiferromagnetic ordering. Let us recall the expression for the energy gap in DTN and, for simplicity, assume that the magnitude of J_{ab} is independent of pressure since J_{ab} is an order of magnitude smaller than J_c ($J_{ab}/k_B = 0.18 \text{ K}$). So we have the dependence of the energy gap as a function of pressure given by

$$\Delta(p) = D(p) - 2J_c(p) - 4J_{ab}. \quad (8.3)$$

Using the estimates for $J_c(p)$ and $D(p)$ from (8.2) we have for $\Delta(p_c) = 0$ that $p_c = 3.16 \text{ kbar}$, which is a value of pressure fully accessible with a hydrostatic pressure cell.

To corroborate our estimate we compare our obtained value for the critical pressure with the value obtained from the pressure dependence along the c -axis of the critical magnetic field H_{c1} , obtained from magnetostriction and magnetic susceptibility measurements and given by [181]

$$\frac{\partial H_{c1}}{\partial p} = -0.676 \text{ T/kbar}. \quad (8.4)$$

Considering that, at $p = 0 \text{ kbar}$ and $T = 0 \text{ K}$, $H_{c1} = 2.2 \text{ T}$ we can obtain from (8.4) the pressure in which we have $H_{c1} = 0 \text{ T}$ as $p_c = 3.25 \text{ kbar}$, which is very close to our estimate but, according to neutron measurements in reference [162] not enough yet to close the gap, what may happen for pressures higher than 4 kbar.

However, these values are just qualitative estimates that were obtained from some approximations. They point out that the magnitude of applied pressure necessary to observe the pressure-induced transition is accessible with a hydrostatic pressure cell.

The next step on the study of the effects of pressure in DTN is to perform magnetization measurements or magnetic susceptibility measurements for lower temperatures, as long as the hindrances of measuring low magnetic signals, thermalization and achieving high pressures are solved.

8.4 Conclusions

In this work we performed some preliminary measurements on the effect of hydrostatic pressure in magnetic measurements in DTN.

We built different versions of hydrostatic pressure cells, some to be used in the MPMS-SQUID and others to be used in our 20 T cryostat. With our pressure cell to the MPMS-SQUID we were able to perform magnetization measurements in DTN under applied pressures up to 7.6 kbar. However due to imperfections in the parts of cell, the maximum pressure typically achieved was around 3 kbar. Regarding our pressure cell to be used in the 20 T cryostat, it was design to host both the pick-up coils and sample inside it. Nonetheless, due to the limitations for the size of the sample and, consequently, the magnitude of its signal, we were not able to measure the magnetic susceptibility on these samples.

From our magnetization measurements in DTN for different applied pressures combined with mean-field fits we determined a linear dependence of the exchange coupling and single-ion anisotropy as a function of pressure. From these dependences we estimated the critical pressure to close the energy gap, and so achieved a pressure-induced ordering, as $p_c = 3.16$ kbar, which is close to the value calculated from the dependence of critical magnetic field H_{c1} with pressure, given by $p_c = 3.25$ kbar.

This estimates point out the possibility for studying the pressure-induced ordering in a hydrostatic pressure cell since the aforementioned experimental issues were solved.

Although neutron studies in reference [162] indicate that the gap does not close for an applied pressure of 4 kbar and that DTN presents an structural phase transition at about 8 kbar, next studies can focus on exploring the magnetic behaviour and the possibility for closing the gap for pressures between 4 kbar and 8 kbar as well as delimit the DTN phase diagram for values of applied pressures and external magnetic field.

Chapter 9

Conclusions and perspectives

In this work we studied the compounds $\text{NiCl}_2\text{-4SC(NH}_2)_2$ (DTN), $\text{MnCl}_2\text{-4SC(NH}_2)_2$ (DTM), $\text{FeCl}_2\text{-4SC(NH}_2)_2$ (DTF) as well as the Br-doped version of DTN, $\text{Ni(Cl}_{1-x}\text{Br}_x)_2\text{-4SC(NH}_2)_2$ from magnetic and specific heat measurements combined with theoretical results from mean-field and, in the case of DTN, with Quantum Monte-Carlo calculations.

In DTN we identified, above the field-induced antiferromagnetic phase diagram which is associated with a BEC phase of magnons, the existence of a quasi-1D Tomonaga-Luttinger liquid (TLL) regime. Although a genuine TLL regime in DTN is not expected due to the small, but not negligible, contribution of the interchain interactions J_{ab} , our experimental and numerical QMC results present significant similarities with experimental results and theoretical predictions for other compound in which a purely 1D description is valid. It suggests that DTN presents the reminiscent of a TLL regime and the existence of coupled TLL chains, leading to complex behaviour of the magnetic excitations. Furthermore, our magnetization measurements at higher temperatures, for $T > J_c/k_B$, as well as our analytical and QMC results determine the single-ion anisotropy parameter $D/k_B = 7.6$ K, which corroborate some results in literature and show discrepancy with other that claim a value around $D/k_B = 8.9$ K for this parameter. We suggest that other interactions, like Dzyaloshinskii-Moriya or higher-order neighbours interactions, not included in the DTN hamiltonian may explain these discrepancies.

Regarding our studies in DTM and DTF compounds, we estimate an exchange coupling J , the single-ion anisotropy parameter D and the gyromagnetic factor g for these compounds through Curie-Weiss law and mean field fittings in our magnetization curves. Susceptibility and specific heat measurements in DTM reveal the existence of antiferromagnetic transitions below 0.55 K. In some specific curves measured with H perpendicular to the c -axis we verify the existence of two phase transitions, which may be associated with a partial, followed by a full, ordering of the magnetic moments, transitions between different spin structures or a structural phase transition. For the DTF compound, no magnetic ordering was found for temperatures down to 100 mK, despite its value for $\theta_{CW} = 10.15$ K, making this compound a candidate for magnetic frustration, with a frustration parameter $f = |\theta_{CW}|/T_N > 100$.

For the Br-doped DTN compound we presented our preliminary results of AC magnetic susceptibility for samples with different amounts of the dopant. These measurements corroborate some studies where it is shown that the larger the amount of Br doping in the system, the lower is the critical field H_{c1} for the occurrence of the BEC phase due to the reduction of the energy gap. From these results we built a phase diagram relating the critical temperatures and fields to the concentration of the Br dopant. To the best of our knowledge our phase diagram is the first one obtained from AC magnetic susceptibility measurements that relates the critical magnetic field, the critical temperature and the bromine content in the Br-doped DTN samples. Studies at lower temperature are needed in order to determine the critical exponent related to the Bose-glass to BEC transition in our samples.

Finally we discuss our preliminary results on the effect of pressure in magnetic measurements in the DTN. Although the reproducibility of our results could not be confirmed for pressures above 3 kbar due to technical issues in our pressure cell, the preliminary results fitted by mean-field theory shows a linear dependence of the exchange interaction and the single-ion anisotropy term as a function of pressure for the range of applied pressure studied. By knowing these dependences we were able to estimate the critical pressure to close the gap as $p_c = 3.16$ kbar, which is close to the value of $p_c = 3.25$ kbar obtained from the dependence of the critical field H_{c1} with pressure. Since such pressure are easily achieved from a hydrostatic pressure cell, we hope our results motivate further investigations at lower temperature in order to observe a pressure-induced magnetic transition in DTN.

Perspectives

We highlight some further features to be explored in the compounds studied in this work

- Although the DTN compound has been extensively studied in the past two decades some questions still demands further exploration. The first one is the aforementioned discrepancy between the values of single-ion anisotropy D reported in the literature. Another question to be explored is the effect of pressure in the DTN phase diagram.

The study of pressure-induced phase transitions in condensed matter-systems is a current field of research. In DTN it represents a challenge, since the signal of the samples is small ($\chi_{ac} = 8 \times 10^{-8}$ emu/mg at $T=1.8$ K). So, in order to study the effect of pressure in χ_{ac} measurements in DTN a large pressure cell is required to host large samples. Another alternative is to use a pressure cell with pick-up coils and, eventually, even the primary coil wrapped around the sample. In both cases the thermalization and the thermometry must be handled with care to obtain trustworthy results.

- Subsequent studies of both DTM and DTF compounds may follow in several directions. Starting from the synthesis of bigger and more regular samples, specially for the DTF compound. One idea is employ the technique of supersaturated solution in a gel to grow more regular samples in suspension.

To determine the strength of the single-ion anisotropy and exchange interactions neutron scattering experiments are needed. Such measurements can also confirm our hypothesis of the existence near-next-neighbours interactions among Mn atoms in DTM, which could explain the existence of the double-peak structure observed in our specific heat measurements and explore our hypothesis for the magnetic frustration in DTF.

The synthesis of similar Mn and Fe based compounds can also be explored, for example by replacing Cl to Br atoms. This leads to interactions and anisotropies with different strengths or even different types of interactions and anisotropies, which may display phenomena such as magnetic frustration or BEC of magnons.

- Regarding our Br-doped DTN samples a full phase diagram for χ_{AC} measurements is one perspective for future works. In fact, for this kind of measurement, there is just one result reported in the literature, for a sample with 8% of bromine in its composition [24]. So, it would be relevant to perform χ_{AC} measurements to study changes in the full phase diagram as a function of the bromine concentration. Even more important is the detailed phase diagram at lower temperatures, in order to characterize the critical exponents related to disordered bosonic systems.

For $H = 0$ it was predicted the existence of the so-called *Mott-Glass phase*, which has the property of being a gapless but display a vanishing susceptibility. The first observation of this phase in a physical system was reported in [24] for 8% of bromine DTN doped sample in specific heat measurements. Since we produced Br-doped DTN samples for several concentrations of dopant, the characterization of this phase as a function of the bromine concentration also could be performed in many experiments, including specific heat and magnetic susceptibility measurements.

As mentioned in Chapter 7, one striking observation in Br-doped DTN is the resurgence of the BEC phase for fields higher than H_{c2} , observed in neutron magnetic resonance experiments [164] and predicted theoretically [165, 166]. Future work may follow to explore this behaviour.

Appendix A

System with two particles with spin-1/2

In this appendix we present some results regarding a system with two particles with spin-1/2. Specifically we are interested in evaluating the product $\mathbf{S}_1\mathbf{S}_2$ of the total spin for the two particles. Such result is used in the derivation of the hamiltonian for the Heisenberg model.

First, let us introduce the Pauli matrices

$$\sigma_x = \begin{pmatrix} 0 & 1 \\ 1 & 0 \end{pmatrix}, \quad \sigma_y = \begin{pmatrix} 0 & -i \\ i & 0 \end{pmatrix}, \quad \sigma_z = \begin{pmatrix} 1 & 0 \\ 0 & -1 \end{pmatrix}. \quad (\text{A.1})$$

The α component of the spin is simply given by

$$S_\alpha = \frac{\hbar}{2}\sigma_\alpha. \quad (\text{A.2})$$

For sake of simplicity we will omit \hbar hereafter.

In a system with two particles with spin 1/2, we can write the spin matrices of this system as a direct product of the spin matrices of the two particles. By the definition, the direct product of two matrices A and B is given by

$$A \otimes B = \begin{pmatrix} a_{11}B & a_{12}B & \dots \\ a_{21}B & a_{22}B & \dots \\ \vdots & \vdots & \ddots \end{pmatrix}, \quad (\text{A.3})$$

where a_{ij} are the entries of the matrix A .

From this definition we are able to construct the matrices for a system of two particles with spin 1/2. First, for the x component we have that the matrices for the two particles can be constructed as $S_{1x} = S_x \otimes \mathbb{1}$ and $S_{2x} = \mathbb{1} \otimes S_x$, which gives

$$S_{1x} = \frac{1}{2} \begin{pmatrix} 0 & 0 & 1 & 0 \\ 0 & 0 & 0 & 1 \\ 1 & 0 & 0 & 0 \\ 0 & 1 & 0 & 0 \end{pmatrix}, \quad S_{2x} = \frac{1}{2} \begin{pmatrix} 0 & 1 & 0 & 0 \\ 1 & 0 & 0 & 0 \\ 0 & 0 & 0 & 1 \\ 0 & 0 & 1 & 0 \end{pmatrix} \quad (\text{A.4})$$

Analogously, for the y and z components, we have

$$S_{1y} = \frac{1}{2} \begin{pmatrix} 0 & 0 & -i & 0 \\ 0 & 0 & 0 & -i \\ i & 0 & 0 & 0 \\ 0 & i & 0 & 0 \end{pmatrix}, \quad S_{2y} = \frac{1}{2} \begin{pmatrix} 0 & -i & 0 & 0 \\ i & 0 & 0 & 0 \\ 0 & 0 & 0 & -i \\ 0 & 0 & i & 0 \end{pmatrix} \quad (\text{A.5})$$

$$S_{1z} = \frac{1}{2} \begin{pmatrix} 1 & 0 & 0 & 0 \\ 0 & 1 & 0 & 0 \\ 0 & 0 & -1 & 0 \\ 0 & 0 & 0 & -1 \end{pmatrix}, \quad S_{2z} = \frac{1}{2} \begin{pmatrix} 1 & 0 & 0 & 0 \\ 1 & -1 & 0 & 0 \\ 0 & 0 & 1 & 0 \\ 0 & 0 & 0 & -1 \end{pmatrix}. \quad (\text{A.6})$$

The product of the total spin of the two particle is given by

$$\mathbf{S}_1 \mathbf{S}_2 = S_{1x} S_{2x} + S_{1y} S_{2y} + S_{1z} S_{2z} \quad (\text{A.7})$$

which, using the matrices that we just built, can be represented by

$$\mathbf{S}_1 \mathbf{S}_2 = \frac{1}{4} \begin{pmatrix} 1 & 0 & 0 & 0 \\ 1 & -1 & 2 & 0 \\ 0 & 2 & -1 & 0 \\ 0 & 0 & 0 & 1 \end{pmatrix}. \quad (\text{A.8})$$

Appendix B

Spin matrices

In this appendix we write the S_x and S_z spin matrices for $S = 1$, $S = 2$ and $S = 5/2$. From these matrices we calculate the magnetization and magnetic susceptibility of non-interacting spin systems in Appendix C.

For $S = 1$

$$S_x = \frac{\sqrt{2}}{2} \begin{pmatrix} 0 & 1 & 0 \\ 1 & 0 & 1 \\ 0 & 1 & 0 \end{pmatrix}, \quad S_z = \begin{pmatrix} 1 & 0 & 0 \\ 0 & 0 & 0 \\ 0 & 0 & -1 \end{pmatrix}. \quad (\text{B.1})$$

For $S = 2$

$$S_x = \frac{1}{2} \begin{pmatrix} 0 & 2 & 0 & 0 & 0 \\ 2 & 0 & \sqrt{6} & 0 & 0 \\ 0 & \sqrt{6} & 0 & \sqrt{6} & 0 \\ 0 & 0 & \sqrt{6} & 0 & 2 \\ 0 & 0 & 0 & 2 & 0 \end{pmatrix}, \quad S_z = \begin{pmatrix} 2 & 0 & 0 & 0 & 0 \\ 0 & 1 & 0 & 0 & 0 \\ 0 & 0 & 0 & 0 & 0 \\ 0 & 0 & 0 & -1 & 0 \\ 0 & 0 & 0 & 0 & -2 \end{pmatrix}. \quad (\text{B.2})$$

For $S = 5/2$

$$S_x = \frac{1}{2} \begin{pmatrix} 0 & \sqrt{5} & 0 & 0 & 0 & 0 \\ \sqrt{5} & 0 & 2\sqrt{2} & 0 & 0 & 0 \\ 0 & 2\sqrt{2} & 0 & 3 & 0 & 0 \\ 0 & 0 & 3 & 0 & 2\sqrt{2} & 0 \\ 0 & 0 & 0 & 2\sqrt{2} & 0 & \sqrt{5} \\ 0 & 0 & 0 & 0 & \sqrt{5} & 0 \end{pmatrix}, \quad S_z = \frac{1}{2} \begin{pmatrix} 5 & 0 & 0 & 0 & 0 & 0 \\ 0 & 3 & 0 & 0 & 0 & 0 \\ 0 & 0 & 1 & 0 & 0 & 0 \\ 0 & 0 & 0 & -1 & 0 & 0 \\ 0 & 0 & 0 & 0 & -3 & 0 \\ 0 & 0 & 0 & 0 & 0 & -5 \end{pmatrix}. \quad (\text{B.3})$$

Appendix C

Magnetization and magnetic susceptibility of ideal paramagnets

In this appendix we detail the calculation of magnetization and magnetic susceptibility for non-interacting spins, which describes an ideal paramagnet. These expressions are used in the context of the mean field theory. These are the first and the simplest approximation to be done in order infer about the magnetic ordering of the systems and its parameters.

C.1 Evaluation of magnetization and magnetic susceptibility

To evaluate the thermodynamic properties of a system, we must find the eigenvalues of the hamiltonian that describe such system to write its partition function

$$Z = \sum_i e^{-\beta E_i}, \quad (\text{C.1})$$

where $\beta = 1/k_B T$ and E_i are the eigenvalues of hamiltonian \mathcal{H} .

Once we have the partition function we can calculate the magnetization as

$$M = \frac{1}{\beta} \frac{\partial \ln Z}{\partial H}, \quad (\text{C.2})$$

and the magnetic susceptibility as

$$\chi = \frac{\partial M}{\partial H}. \quad (\text{C.3})$$

C.2 Expressions for H applied parallel to c -axis

In the case when the external magnetic field H is applied parallel to z -axis, we have that the hamiltonian for a single-ion is given by

$$\mathcal{H} = DS_z^2 - g\mu_B H S_z. \quad (\text{C.4})$$

APPENDIX C. MAGNETIZATION AND MAGNETIC SUSCEPTIBILITY OF IDEAL PARAMAGNETS

Since hamiltonian is diagonal, we can easily calculate the magnetization and magnetic susceptibility. For a $S = 1$ system we have

$$\mathcal{H} = \begin{pmatrix} D - g\mu_B H & 0 & 0 \\ 0 & 0 & 0 \\ 0 & 0 & D + g\mu_B H \end{pmatrix}, \quad (\text{C.5})$$

and, from equation (C.2), the magnetization is given by

$$M(T, H) = Ng\mu_B \left[\frac{2 \exp(-D\beta) \sinh(\beta g_z \mu_B H)}{1 + 2 \exp(-D\beta) \cosh(\beta g_z \mu_B H)} \right]. \quad (\text{C.6})$$

The zero-field magnetic susceptibility, from equation (C.3), is

$$\chi_z(T, H = 0) = \frac{2Ng^2\mu_B^2}{k_B T} \left[\frac{\exp(-D\beta)}{1 + 2 \exp(-D\beta)} \right]. \quad (\text{C.7})$$

In a $S = 2$ system

$$\mathcal{H} = \begin{pmatrix} 4D - 2g\mu_B H & 0 & 0 & 0 & 0 \\ 0 & D - g\mu_B H & 0 & 0 & 0 \\ 0 & 0 & 0 & 0 & 0 \\ 0 & 0 & 0 & D + g\mu_B H & 0 \\ 0 & 0 & 0 & 0 & 4D + 2g\mu_B H \end{pmatrix}, \quad (\text{C.8})$$

$$M(T, H) = Ng_z \mu_B \left[\frac{4 \exp(-4D\beta) \sinh(2\beta g_z \mu_B H) + \exp(-D\beta) \sinh(\beta g_z \mu_B H)}{2 \exp(-4D\beta) \cosh(2\beta g_z \mu_B H) + \exp(-D\beta) \cosh(\beta g_z \mu_B H) + 1} \right], \quad (\text{C.9})$$

and

$$\chi_z(T, H = 0) = \frac{Ng^2\mu_B^2}{k_B T} \left[\frac{2 \exp(-D\beta) + 8 \exp(-4D\beta)}{1 + 2 \exp(-2D\beta) + 2 \exp(-4D\beta)} \right]. \quad (\text{C.10})$$

Finally, for $S = 5/2$ we have

$$\mathcal{H} = \begin{pmatrix} \frac{25}{4}D - \frac{5}{2}g\mu_B H & 0 & 0 & 0 & 0 & 0 \\ 0 & \frac{9}{4}D - \frac{3}{2}g\mu_B H & 0 & 0 & 0 & 0 \\ 0 & 0 & \frac{1}{4}D - \frac{1}{2}g\mu_B H & 0 & 0 & 0 \\ 0 & 0 & 0 & \frac{1}{4}D + \frac{1}{2}g\mu_B H & 0 & 0 \\ 0 & 0 & 0 & 0 & \frac{9}{4}D + \frac{3}{2}g\mu_B H & 0 \\ 0 & 0 & 0 & 0 & 0 & \frac{25}{4}D + \frac{5}{2}g\mu_B H \end{pmatrix}, \quad (\text{C.11})$$

$$M(T, H) = \frac{Ng_z \mu_B}{2} \left[\frac{5 \exp(-6D\beta) \sinh(\frac{5}{2}\beta g_z \mu_B H) + 3 \exp(-2D\beta) \sinh(\frac{3}{2}\beta g_z \mu_B H) + \sinh(\frac{1}{2}\beta g_z \mu_B H)}{\exp(-6D\beta) \cosh(\frac{5}{2}\beta g_z \mu_B H) + \exp(-2D\beta) \cosh(\frac{3}{2}\beta g_z \mu_B H) + \cosh(\frac{1}{2}\beta g_z \mu_B H)} \right], \quad (\text{C.12})$$

and

$$\chi_z(T, H = 0) = \frac{Ng^2\mu_B^2}{4k_B T} \left[\frac{1 + 9 \exp(-2D\beta) + 25 \exp(-6D\beta)}{1 + \exp(-2D\beta) + \exp(-6D\beta)} \right]. \quad (\text{C.13})$$

C.3 Expressions for H applied perpendicular to c -axis

When the external magnetic field H is applied perpendicular to z -axis, as for example along x -axis, then we have that the hamiltonian for a single-ion is given by

$$\mathcal{H} = DS_z^2 - g\mu_B H S_x. \quad (\text{C.14})$$

In this case the matrices are not diagonal and in some cases the exact diagonalization of such matrices can be very cumbersome and demand approximations such as some perturbation theory to evaluate the eigenvalues.

For the $S = 1$ case, the hamiltonian from C.14 can be written in a matrix form as

$$\mathcal{H} = \begin{pmatrix} D & -\frac{\sqrt{2}}{2}g\mu_B H & 0 \\ -\frac{\sqrt{2}}{2}g\mu_B H & 0 & -\frac{\sqrt{2}}{2}g\mu_B H \\ 0 & -\frac{\sqrt{2}}{2}g\mu_B H & D \end{pmatrix}. \quad (\text{C.15})$$

Diagonalizing this hamiltonian is simple and gives the eigenvalues

$$E_1 = \frac{1}{2} \left[D - (D^2 + 4H^2)^{1/2} \right], \quad E_2 = D, \quad \text{and} \quad E_3 = \frac{1}{2} \left[D + (D^2 + 4H^2)^{1/2} \right]. \quad (\text{C.16})$$

For $H = 0$ the magnetic susceptibility is given by

$$\chi_x(T, H = 0) = \frac{2Ng^2\mu_B^2}{D} \left[\frac{1 - \exp(-D\beta)}{1 + 2 \exp(-D\beta)} \right]. \quad (\text{C.17})$$

Diagonalizing (C.14) for $S = 2$ and $S = 5/2$ is a difficult task. Here we present the $S = 2$ and $S = 5/2$ hamiltonians written in a matrix form and the zero-field magnetic susceptibility obtained from reference [182] for $S = 2$ and from reference [46] for $S = 5/2$.

For $S = 2$ the hamiltonian written in a matrix form is given by

$$\mathcal{H} = \begin{pmatrix} 4D & -g\mu_B H & 0 & 0 & 0 \\ -g\mu_B H & D & -\sqrt{\frac{3}{2}}g\mu_B H & 0 & 0 \\ 0 & -\sqrt{\frac{3}{2}}g\mu_B H & 0 & -\sqrt{\frac{3}{2}}g\mu_B H & 0 \\ 0 & 0 & -\sqrt{\frac{3}{2}}g\mu_B H & D & -g\mu_B H \\ 0 & 0 & 0 & -g\mu_B H & 4D \end{pmatrix}, \quad (\text{C.18})$$

and the magnetic susceptibility at zero field is

$$\chi_x(T, H = 0) = \frac{Ng^2\mu_B^2}{k_B T} \left[\frac{\frac{6k_B T}{D}(1 - \exp(-D\beta)) + \frac{4D}{3k_B T}(\exp(-D\beta) - \exp(-4D\beta))}{1 + 2\exp(-2D\beta) + 2\exp(-4D\beta)} \right]. \quad (\text{C.19})$$

For $S = 5/2$ the hamiltonian written in a matrix form is given by

$$\mathcal{H} = \begin{pmatrix} \frac{25}{4}D & -\frac{\sqrt{5}}{2}g\mu_B H & 0 & 0 & 0 & 0 \\ -\frac{\sqrt{5}}{2}g\mu_B H & \frac{9}{4}D & -\sqrt{2}g\mu_B H & 0 & 0 & 0 \\ 0 & -\sqrt{2}g\mu_B H & \frac{1}{4}D & -\frac{3}{2}g\mu_B H & 0 & 0 \\ 0 & 0 & -\frac{3}{2}g\mu_B H & \frac{1}{4}D & -\sqrt{2}g\mu_B H & 0 \\ 0 & 0 & 0 & -\sqrt{2}g\mu_B H & \frac{9}{4}D & -\frac{\sqrt{5}}{2}g\mu_B H \\ 0 & 0 & 0 & 0 & -\frac{\sqrt{5}}{2}g\mu_B H & \frac{25}{4}D \end{pmatrix}, \quad (\text{C.20})$$

and the magnetic susceptibility at zero field is

$$\chi_x(T, H = 0) = \frac{Ng^2\mu_B^2}{4k_B T} \left[\frac{\left(\frac{9}{k_B T} + \frac{8}{D}\right) - \frac{11}{2D}\exp(-2D\beta) - \frac{5}{2D}\exp(-6D\beta)}{1 + \exp(-2D\beta) + \exp(-6D\beta)} \right]. \quad (\text{C.21})$$

Bibliography

- [1] N. Singh, and A. M. Jayannavar, arXiv:1903.07031v1.
- [2] M. L. Neel, Ann. Phys. **12** (3), 137 (1948).
- [3] C. G. Shull, W. A. Strauser, and E. O. Wollan, Phys. Rev. **83**, 333 (1951).
- [4] F. Bloch, Z. Physik **61**, 206 (1930).
- [5] B. N. Brockhouse, Phys. Rev. **106** (5), 859 (1957).
- [6] T. Matsubara and H. Matsuda, Prog. Theor. Phys. **16** 569 (1956).
- [7] E. Batyev and L. Braginskii, Sov. Phys. JETP **60** 781 (1984).
- [8] I. Affleck, Phys. Rev. B **41**, 6697 (1990).
- [9] I. Affleck, Phys. Rev. B **43**, 3215 (1991).
- [10] T. Giamarchi and A. M. Tsvelik, Phys. Rev. B **59**, 11398 (1999).
- [11] L. P. Pitaevskii and S. Stringari, *Bose-Einstein Condensation*, Oxford University Press, 2003.
- [12] M. H. Anderson, J. R. Ensher, M. R. Matthews, C. H. Weiman and E. A. Cornell, Science **269**, 198 (1995).
- [13] K. B. Davis, M. O. Mewes, M. R. Andrews, N. J. van Druten, D. S. Durfee, D. M. Kurn, and W. Ketterle, Phys. Rev. Lett. **75**, 3969 (1995).
- [14] A. Griffin, A Brief History of Our Understanding of BEC: from Bose to Beliaev, arXiv:cond-mat/9901123.
- [15] J. Kasprzak, M. Richard, S. Kundermann, A. Baas, P. Jeambrun, J. M. J. Keeling, F. M. Marchetti, M. H. Szymańska, R. André, J. L. Staehli, V. Savona, P. B. Littlewood, B. Deveaud, and Le Si Dang, Nature **443**, 409 (2006).
- [16] S. O. Demokritov, V. E. Demidov, O. Dzyapko, G. A. Melkov, A. A. Serga, B. Hillebrands, and A. N. Slavin, Nature **443**, 430 (2006).
- [17] V. Zapf, M. Jaime, and C. D. Batista, Rev. Mod. Phys. **86**, 563 (2014).

- [18] T. Nikuni, M. Oshikawa, A. Oosawa, and H. Tanaka, *Phys. Rev. Lett.* **84**, 5868 (2000).
- [19] P. A. Lee, *RVB description of a high- T_c superconductor* in *More is different : fifty years of condensed matter physics*, Edited by N. Phuan Ong and R. N. Bhatt, Princeton university press, New Jersey, 2001.
- [20] M. Hagiwara, H. Tsujii, C. R. Rotundu, B. Andraka, Y. Takano, N. Tateiwa, T. C. Kobayashi, T. Suzuki, and S. Suga, *Phys. Rev. Lett.* **96**, 147203 (2006).
- [21] M. Jeong, D. Schmidiger, H. Mayaffre, M. Klanjšek, C. Berthier, W. Knafo, G. Ballon, B. Vignolle, S. Krämer, A. Zheludev, and M. Horvatić, *Phys. Rev. Lett.* **117**, 106402 (2016).
- [22] J. S. Gardner, M. J. P. Gingras, and J. E. Greedan, *Rev. Mod. Phys.* **82**, 53 (2010).
- [23] D. J. P. Morris *et al*, *Science* **326**, 411 (2009).
- [24] R. Yu, L. Yin, N. S. Sullivan, J. S. Xia, C. Huan, A. Paduan-Filho, N. F. Oliveira Jr, S. Haas, A. Steppke, C. F. Miclea, F. Weickert, R. Movshovich, E.-D. Mun, B. L. Scott, V. S. Zapf, and T. Roscilde, *Nature* **489**, 379-384 (2012).
- [25] E. Wulf, D. Hüvonen, J.-W. Kim, A. Paduan-Filho, E. Ressouche, S. Gvasaliya, V. Zapf, and A. Zheludev, *Phys. Rev. B* **88**, 174418 (2013).
- [26] T. Saito, A. Oosawa, T. Goto, T. Suzuki, and I. Watanabe, *Phys. Rev. B* **74**, 134423 (2006).
- [27] H. Manaka, A. V. Kolomiets, and T. Goto, *Phys. Rev. Lett.* **101**, 077204 (2008).
- [28] H. Manaka, H. A. Katori, O. V. Kolomiets, and T. Goto, *Phys. Rev. B* **79**, 092401 (2009).
- [29] Y. Shindo, and H. Tanaka, *J. Phys. Soc. Jpn.* **73**, 2642 (2004).
- [30] T. Suzuki, F. Yamada, T. Kawamata, I. Watanabe, T. Goto, and H. Tanaka, *Phys. Rev. B* **79**, 104409 (2009).
- [31] T. Suzuki, F. Yamada, M. Yamada, T. Kawamata, Y. Ishii, I. Watanabe, T. Goto, and H. Tanaka, *Phys. Rev. B* **82**, 094447 (2010).
- [32] F. Yamada, H. Tanaka, T. Ono, and H. Nojiri *Phys. Rev. B* **83**, 020409(R) (2011).
- [33] A. Oosawa, M. Fujisawa, T. Osakabe, K. Kakurai, and H. Tanaka, *J. Phys. Soc. Jpn.* **72**, 1026 (2003).
- [34] A. Oosawa, K. Kakurai, T. Osakabe, M. Nakamura, M. Takeda, and H. Tanaka, *J. Phys. Soc. Jpn.* **73**, 1446 (2004).

- [35] K. Goto, M. Fujisawa, T. Ono, H. Tanaka, and Y. Uwatoko, *J. Phys. Soc. Jpn.* **73**, 3254 (2004).
- [36] Ch. Rüegg, A. Furrer, D. Sheptyakov, Th. Strässle, K. W. Krämer, H.-U. Güdel, and L. Mélési, *Phys. Rev. Lett.* **93**, 257201 (2004).
- [37] Ch. Rüegg, B. Normand, M. Matsumoto, A. Furrer, D. F. McMorrow, K. W. Krämer, H. -U. Güdel, S. N. Gvasaliya, H. Mutka, and M. Boehm, *Phys. Rev. Lett.* **100**, 205701 (2008).
- [38] Tao Hong, V. O. Garlea, A. Zheludev, J. A. Fernandez-Baca, H. Manaka, S. Chang, J. B. Leao, and S. J. Poulton, *Phys. Rev. B* **78**, 224409 (2008).
- [39] Tao Hong, C. Stock, I. Cabrera, C. Broholm, Y. Qiu, J. B. Leao, S. J. Poulton, and J. R. D. Copley, *Phys. Rev. B* **82**, 184424 (2010).
- [40] N. Kurita and H. Tanaka, *Phys. Rev. B* **94**, 104409 (2016).
- [41] P. Fazekas, *Lecture Notes on Electron Correlation and Magnetism*, World Scientific, Singapore, 2003.
- [42] C. M. Hurd, *Contemp. Phys.* **23**, 469 (1982).
- [43] S. Blundell, *Magnetism in Condensed Matter*, Oxford University press, UK, 2001.
- [44] R. L. Carlin, *Magnetic properties of transition metal compounds*, New York, Springer-Verlag, 1977.
- [45] D. J. Griffiths, *Introduction to Quantum Mechanics*, Prentice Hall, New Jersey, 1995.
- [46] O. Kahn, *Molecular Magnetism*, VHC, New York, 1993.
- [47] C. P. Keijzers, *Spin-Spin Interactions in Weakly Interacting Dimers*, in *Electron Spin Resonance, A Specialist Periodical Report* vol. 10B, edited by M. C . R. Symons, Royal Society of Chemistry, 1987.
- [48] P. H. Rieger, *Electron Spin Resonance, Analysis ans Interpretation*, RSC Publishing, Rhode Island, 2007.
- [49] A. Paduan-Filho, R. D. Chirico, K. O. Joung, R. L. Carlin, *J. Chem. Phys.* **74**(7), 4103 (1981).
- [50] A. Paduan-Filho, X. Gratens, N.F. Oliveira Jr. *Phys. Rev. B* **69** 020405(R) (2004).
- [51] S. A. Zvyagin, J. Wosnitza, C. D. Batista, M. Tsukamoto, N. Kawashima, J. Krzystek, V. S. Zapf, M. Jaime, N. F. Oliveira, Jr., and A. Paduan-Filho, *Phys. Rev. Lett.* **98**, 047205 (2007).
- [52] N. Tsyrlin *et al*, *J. Phys.: Condens. Matter* **25**, 216008 (2013).

- [53] V.S. Zapf, *A Review of Bose-Einstein Condensation in Cu and Ni Quantum Magnets*, U. Schollwöck, J. Richter, D. J. J. Farnell, R. F. Bishop (Eds.), *Quantum Magnetism*, Springer, Dordrecht, 2008.
- [54] V. S. Zapf, D. Zocco, B. R. Hansen, M. Jaime, N. Harrison, C. D. Batista, M. Kenzelmann, C. Niedermayer, A. Lacerda, and A. Paduan-Filho, *Phys. Rev. Lett.* **96**, 077204 (2006).
- [55] F. D. M. Haldane, *Phys. Lett.* **93**, 464 (1983).
- [56] F. D. M. Haldane, *Phys. Rev. Lett.* **50** 1153 (1983).
- [57] O. Golinelli, Th. Jolicoeur, R. Lacaze, *Phys. Rev. B* **46**, 10854 (1992).
- [58] N. Papanicolaou and P. Spathis, *J. Phys.: Condens. Matter* **1**, 5555 (1989).
- [59] H. Fabrelli, A. P. Vieira, A. Paduan-Filho, and R. S. Freitas, *J. Alloys Compd.* **853**, 157346 (2021).
- [60] A. Paduan-Filho, *Braz. J. Phys* **42**, 292 (2012).
- [61] A. V. Sizanov, and A. V. Syromyatnikov, *Phys. Rev. B* **84**, 054445 (2011).
- [62] C. Psaroudaki, S. A. Zvyagin, J. Krzystek, A. Paduan-Filho, X. Zotos, and N. Papanicolaou, *Phys. Rev. B* **85**, 014412 (2012).
- [63] P. Jordan and E. Wigner, *Z. Phys* **47**, 631 (1928).
- [64] T. Matsubara and H. Matsuda, *Prog. Theor. Phys.* **16**, 569 (1956).
- [65] T. Holstein and H. Primakoff, *Phys. Rev.* **58** 1098 (1940).
- [66] Rémi Blinder, *Étude par Résonance Magnétique Nucléaire de nouveaux états quantiques induits sous champ magnétique: condensation de Bose-Einstein dans le composé DTN*, PhD thesis, Université Grenoble Alpes, 2015.
- [67] Maxime Dupont, *Dynamics and disorder in quantum antiferromagnets*, PhD thesis, Université de Toulouse, 2019.
- [68] E. R. S. Gopal, *Specific Heats at low temperatures*, Plenum press, New York, 1966.
- [69] B. Bleaney, *Phys. Rev.* **78**, 214 (1950).
- [70] R. Eisberg and R. Resnick, *Física Quântica, Átomos, Moléculas, Sólidos, Núcleos e Partículas*, Elsevier, Rio de Janeiro, 1979.
- [71] C. Kittel, *Introduction to Solid State Physics*, 8th edition, John Wiley and Sons, Inc., New York, 2005.

BIBLIOGRAPHY

- [72] M. J. Oliveira, *Notes on Statistical Mechanics* (in portuguese), <http://fge.if.usp.br/oliveira/disc-intmecest.html>.
- [73] M. Getzlaff, *Fundamentals of Magnetism*, Springer-Verlag, Berlin, 2008.
- [74] S. R. A. Salinas, *Introduction to Statistical Physics*, Springer-Verlag, New York, 2001.
- [75] http://alps.comp-phys.org/mediawiki/index.php/Main_Page (last seen in 06/11/2020).
- [76] A. W. Sandvik, R. R. P. Singh, and D. K. Campbell, *Phys. Rev. B* **56**, 14510 (1997).
- [77] A. W. Sandvik, *J. Phys. A: Math. Gen.* **25** 3667 (1992).
- [78] M. Troyer and U.-J. Wiese, *Phys. Rev. Lett.* **94**, 170201 (2005).
- [79] <https://icsd-fiz-karlsruhe-de.proxy01.dotlib.com.br/search/basic.xhtml> (ICSD Collection Code: 61123 - Last seen in 7/21/2018).
- [80] R. P. Feynman, *The Feynman Lectures on Physics* vol. II, Pearson P T R, 1st Edition, 1970.
- [81] <https://icsd-fiz-karlsruhe-de.proxy01.dotlib.com.br/search/basic.xhtml> (ICSD Collection Code: 966808 - Last seen in 7/21/2018).
- [82] <https://icsd-fiz-karlsruhe-de.proxy01.dotlib.com.br/search/basic.xhtml> (ICSD Collection Code: 49735 - Last seen in 7/21/2018).
- [83] <https://icsd-fiz-karlsruhe-de.proxy01.dotlib.com.br/search/basic.xhtml> (ICSD Collection Code: 92579 - Last seen in 7/21/2018).
- [84] P. J. McCarthy, and I. M. Walker, *Can. J. Chem.* **56**, 1284 (1978).
- [85] C. D. Baer, *J. Chem. Educ.* **67**, 410 (1990).
- [86] L. J. Chen, and X. H. Xu, *Z. Kristallogr NCS* **229**, 94 (2014).
- [87] J. Shi, H. S. Xu, L. M. Chen, J. D. Song, J. C. Wu, X. G. Liu, X. Zhao, and X. F. Sun, *J. Cryst. Growth.* **451**, 6 (2016).
- [88] M. Nardelli, L. Calvaca, and A. Braibanti, *Gazz. Chem. Ital.* **86**, 867 (1956).
- [89] A. Rosenheim, and V. J. Meyer, *Z. Anorg. Chem.* **49**, 13 (1906).
- [90] R. A. Bailey, and T. R. Peterson, *Can. J. Chem.* **45** 1135 (1967).
- [91] U. Russo, S. Calogero, N. Burriesci, and M. Pretera, *J. Inorg. Nucl. Chem.* **41**, 25 (1979).
- [92] E. Krell, *Handbook of Laboratory Distillation* (3rd ed.), Elsevier Science Ltd, 1982.

- [93] <https://www.bruker.com/products/x-ray-diffraction-and-elemental-analysis/x-ray-diffraction/d8-advance/overview.html> (Last seen in 7/21/2018).
- [94] R. L. Snyder, Analytical profile fitting of X-ray powder diffraction profiles in Rietveld analysis, In R. A. Young (ed.) *The Rietveld Method*, Oxford University Press, New York, 1995.
- [95] <https://www.ill.eu/sites/fullprof/> (Last seen in 7/21/2018).
- [96] R. Jenkins, R. W. Gould, and D. Gedcke, *Quantitative X-ray Spectrometry*, Marcel Dekker Inc., New York, 1995.
- [97] <http://amptek.com/products/sdd-x-ray-detectors-for-xrf-eds/xr-100sdd-silicon-drift-detector> (Last access in 03/09/2020).
- [98] <http://physics.nist.gov/PhysRefData/Xray/Trans/Html/search.html> (Last access in 03/09/2020).
- [99] Christian Enss and Siegfried Hunklinger, *Low-Temperature Physics*, Springer-Verlag, Heidelberg, Germany, 2005.
- [100] B. D. Josephson, Phys. Lett. **1** (7), 251 (1962).
- [101] *Magnetic Property Measurement System MPMS XL Hardware Reference Manual Quantum Design*, San Diego, CA.
- [102] M. Buchner, K. Höflera, B. Henne, V. Ney, and A. Ney, J. Appl. Phys. **124**, 161101 (2018).
- [103] Manual PPMS, <https://www.qdusa.com/pharos> (Last seen in 8/23/2018).
- [104] S. Foner, Rev. Sci. Instrum. **30**, 548 (1959).
- [105] B. D. Cullity, and C. D. Graham, *Introduction to Magnetic Materials* 2nd ed., John Wiley & Sons, New Jersey, 2009.
- [106] F. Pobell, *Matter and Methods at Low Temperatures*, 3rd ed., Springer-Verlag, 2007.
- [107] R. C. Richardson and E. N. Smith, *Experimental Techniques in Condensed Matter Physics at Low Temperatures*, CRC Press, 1998.
- [108] V. B. Barbeta, *Comportamento da susceptibilidade AC $\chi_{AC}(T, H)$ nos antiferromagnetos $\text{MnBr}_2 \cdot 4\text{H}_2\text{O}$ e $\text{Mn}(\text{Br}_{0.7}\text{Cl}_{0.3})_2 \cdot 4\text{H}_2\text{O}$* , Master's degree dissertation, Instituto de Física da Universidade de São Paulo, São Paulo, Brazil, 1990.
- [109] A. Vasiliev, O. Volkova, E. Zvereva, and M. Markina, npj Quant. Mater. **3**, 18 (2018).
- [110] C. Yasuda, S. Todo, K. Hukushima, F. Alet, M. Keller, M. Troyer, and H. Takayama, Phys. Rev. Lett. **94**, 217201 (2005).

- [111] T. Knaflič, M. Klanjšek, A. Sans, P. Adler, M. Jansen, C. Felser, and D. Arčon, *Phys. Rev. B* **91**, 174419 (2015).
- [112] E. Ising, *Z. Phys.* **31**, 253 (1925).
- [113] H. Bethe, *Z. Phys.* **71**, 205 (1931).
- [114] T. Giamarchi, *Quantum Physics in One Dimension*, Clarendon Press, Oxford, UK, 2003.
- [115] D. C. Mattis, *The Theory of Magnetism Made Simple*, World Scientific, Singapore, 2006.
- [116] A. A. Abrikosov, I. E. Dzyaloshinski, and L. Gor'kov, *Methods of Quantum Field Theory in Statistical Physics*, Dover Publications, INC. NY, 1963.
- [117] F. D. M. Haldane, *J. Phys. C: Solid State Phys.* **14**, 2585 (1981).
- [118] S. Tomonaga, *Prog. Theor. Phys.* **5**, 544 (1950); J. M. Luttinger, *J. Math. Phys.* **4**, 1154 (1963); D.C. Mattis and E.H. Lieb, *J. Math. Phys.* **6**, 304 (1965).
- [119] M. Bockrath, D. H. Cobden, J. Lu, A. G. Rinzler, R. E. Smalley, L. Balents, and P. L. McEuen, *Nature* **397**, 598 (1999).
- [120] H. Ishii, H. Kataura, H. Shiozawa, H. Yoshioka, H. Otsubo, Y. Takayama, T. Miyahara, S. Suzuki, Y. Achiba, M. Nakatake, T. Narimura, M. Higashiguchi, K. Shimada, H. Namatame, and M. Taniguchi, *Nature* **426**, 540 (2003).
- [121] S. Jezouin, M. Albert, F. D. Parmentier, A. Anthore, U. Gennser, A. Cavanna, I. Safi, and F. Pierre, *Nat. Commun.* **4**, 1802 (2003).
- [122] S. Hofferberth, I. Lesanovsky, T. Schumm, A. Imambekov, V. Gritsev, E. Demler and J. Schmiedmayer, *Nat. Phys.* **4**, 489 (2008).
- [123] A. Recati, P. O. Fedichev, W. Zwerger, and P. Zoller, *J. Opt. B: Quantum Semiclass. Opt.* **5** (2), S55 (2003).
- [124] B. Willenberg *et al*, *Phys. Rev. B* **91**, 060407(R) (2015).
- [125] T. Matsushita, N. Hori, S. Takata, N. Wada, N. Amaya, and Y. Hosokoshi, *Phys. Rev. B* **95**,020408(R) (2017).
- [126] N. Maeshima, K. Okunishi, K. Okamoto, and T. Sakai, *Phys. Rev. Lett.* **93**, 127203 (2004).
- [127] A. Zheludev, T. Masuda, B. Sales, D. Mandrus, T. Papenbrock, T. Barnes, and S. Park, *Phys. Rev. B* **69**, 144417 (2004).
- [128] M. Klanjšek *et al*, *Phys. Rev. Lett.* **101**, 137207 (2008).

- [129] Ch. Rüegg, K. Kiefer, B. Thielemann, D. F. McMorrow, V. Zapf, B. Normand, M. B. Zvonarev, P. Bouillot, C. Kollath, T. Giamarchi, S. Capponi, D. Poilblanc, D. Biner, and K. W. Krämer, *Phys. Rev. Lett* **101**, 247202 (2008).
- [130] B. Thielemann *et al*, *Phys. Rev. B* **79**, 020408(R) (2009).
- [131] J. L. White *et al*, *Phys. Rev. B* **81**, 052407 (2010).
- [132] M. Dupont, S. Capponi, and N. Laflorencie, *Phys. Rev. B* **94**, 144409 (2016).
- [133] S. Mukhopadhyay *et al*, *Phys. Rev. Lett.* **109**, 177206 (2012).
- [134] O. Chiatti, A. Sytcheva, J. Wosnitza, S. Zherlitsyn, A. A. Zvyagin, V. S. Zapf, M. Jaime, and A. Paduan-Filho, *Phys. Rev. B* **78**, 094406 (2008); S. Zherlitsyn, O. Chiatti, A. Sytcheva, J. Wosnitza, A. A. Zvyagin, V. S. Zapf, M. Jaime, and A. Paduan-Filho, *J. Phys. Conf. Ser.* **145**, 012069 (2009).
- [135] C. Psaroudaki, J. Herbrych, J. Karadamoglou, P. Prelovšek, X. Zotos, and N. Papanicolaou, *Phys. Rev. B* **89**, 224418 (2014).
- [136] A. V. Sologubenko, T. Lorenz, J. A. Mydosh, B. Thielemann, H. M. Rønnow, Ch. Rüegg, and K. W. Krämer, *Phys. Rev. B* **80**, 220411(R) (2009).
- [137] Bing Yang, Yang-Yang Chen, Yong-Guang Zheng, Hui Sun, Han-Ning Dai, Xi-Wen Guan, Zhen-Sheng Yuan, and Jian-Wei Pan, *Phys. Rev. Lett.* **119**, 165701 (2017).
- [138] H. J. Schulz, *Coupled Luttinger Liquids*. In T. Martin, G. Montambaux and J. Trân Thanh Vân (Eds.), *Correlated Fermions and Transport in Mesoscopic Systems*, Editions Frontieres, France, 1996.
- [139] H. J. Van Till, *The Magnetic Susceptibility of Some Thiourea-Coordinated Transition Metal Halides in the Paramagnetic and Antiferromagnetic States*, PhD thesis, Michigan State University, 1965.
- [140] M. Gerloch, J. Lewis and W. R. Smail, *J. Chem. Soc., Dalton Trans.*, **14**, 1559 (1972).
- [141] U. Russo, S. Calogero, N. Burriesci, and M. Petrera, *J. Inor. Nucl. Chem.* **41**, 25 (1979).
- [142] U. Russo, R. Graziani, S. Calogero, and U. Casellato, *Transition Met. Chem.* **4**, 82 (1979).
- [143] T. Watanabe, *J. Phys. Soc. Jpn* **17** (12), 1856 (1962).
- [144] V. Hardy, S. Lambert, M. R. Lees, and D. McK. *Phys. Rev. B* **68**, 014424 (2003).
- [145] M. A. Fisher, *Philos. Mag.* **7** (82), 1731 (1962).
- [146] J. A. Eisele and F. Keffer, *Phys. Rev.* **96**, 929 (1954).

- [147] R. J. Joenk, Phys. Rev. **128**, 1634 (1962).
- [148] F. Keffer, *Spin waves Handbuch der Physik vol XVIII-2*, in *Ferromagnetism/Ferromagnetismus*, edited by H. P. J. Wijn, Berlin:Springer, 1966.
- [149] R. S. Freitas, A. Paduan-Filho and C. C. Becerra, J. Phys.: Condens. Matter **28**, 126007 (2016).
- [150] R. B. Murray, Phys. Rev. **100** (4), 1071 (1995).
- [151] D. G. Wiesler, M. Suzuki, I. S. Suzuki, and N. Rosov, Phys. Rev. Lett. **75**, 942 (1995).
- [152] D. Billerey, C. Terrier, N. Ciret, and J. Kleinclauss, Phys. Lett. A **61** (2), 138 (1977).
- [153] L. G. Polgar, A. Herweijer, and W. J. M. de Jonge, Phys. Rev. B **5**, 1957 (1972).
- [154] C. H. W. Swüste, A. C. Botterman, J. Millenaar, and W. J. M. de Jonge, J. Chem. Phys. **66** (11), 5021 (1977).
- [155] K. Kopinga and W. J. M. de Jonge, Phys. Lett. A **43**,(5) 415 (1973).
- [156] H. Forstat, N. D. Love, and J. McElearney, J. Chem. Phys. **43** (5), 1626 (1965).
- [157] H. Forstat, N. D. Love, and J. McElearney, J. Phys. Soc. Jpn. **23** (2), 229 (1967).
- [158] Eundeok Mun, Franziska Weickert, Jaewook Kim, Brian L. Scott, Corneliu Florin Miclea, Roman Movshovich, Jason Wilcox, Jamie Manson, and Vivien S. Zapf, Phys. Rev. B **93**, 104407 (2016).
- [159] N. Blanc, J. Trinh, L. Dong, X. Bai, A. A. Aczel, M. Mourigal, L. Balents, T. Siegrist, and A. P. Ramirez, Nat. Phys. **14**, 273 (2018).
- [160] D. G. Weisler, M. Suzuki, I. S. Suzuki, and N. Rosov, Phys. Rev. Lett. **95**, 942 (1995).
- [161] K. Yu. Povarov, E. Wulf, D. Hüvonen, J. Ollivier, A. Paduan-Filho, and A. Zheludev, Phys. Rev. B **92**, 024429 (2015).
- [162] Alexandra Mannig, *Experimental Studies of Zero-Field Phase Transitions in Quantum Magnets*, PhD thesis, ETH Zurich, 2017.
- [163] K. Yu. Povarov, A. Mannig, G. Perren, J. S. Möller, E. Wulf, J. Ollivier, and A. Zheludev, Phys. Rev. B **96**, 140414(R) (2017).
- [164] A. Orlova *et al*, Phys. Rev. Lett. **118**, 067203 (2017).
- [165] A. Orlova, H. Mayaffre, S. Krämer, M. Dupont, S. Capponi, N. Laflorencie, A. Paduan-Filho, and M. Horvatić, Phys. Rev. Lett. **121**, 177202 (2018).

- [166] M. Dupont, S. Capponi, M. Horvatić, and N. Laflorencie, Phys. Rev. B **96**, 024442 (2017).
- [167] T. Vojta, Ann. Rev. Condensed Matter Phys. **10**, 233 (2019).
- [168] P. W. Anderson, Phys. Rev. **109** (5), 1492 (1958).
- [169] Tianping Ying, Yueqiang Gu, Xiao Chen, Xinbo Wang, Shifeng Jin, Linlin Zhao, Wei Zhang, and Xiaolong Chen, Sci. Adv. **2** (2), e1501283 (2016).
- [170] T. Giamarchi and H. J. Schulz Phys. Rev. B **37**, 325 (1988).
- [171] M. P. A. Fisher, P. B. Weichman, G. Grinstein, and D. S. Fisher, Phys. Rev. B **40**, 546 (1989).
- [172] Zhiyuan Yao, Karine P. C. da Costa, Mikhail Kiselev, and Nikolay Prokof'ev, Phys. Rev. Lett. **112**, 225301 (2014).
- [173] P. B. Weichman, Mod. Phys. Lett. B **22** (27), 2623 (2008).
- [174] A. Zheludev, and T. Roscilde, C. R. Physique **14**, 740 (2013).
- [175] L. Yin, J. S. Xia, N. S. Sullivan, V. S. Zapf, A. Paduan-Filho, R. Yu, and T. Roscilde, J. Phys. Conf. Ser **400**, 032122 (2012).
- [176] K. Wierschem and P. Sengupta, Mod. Phys. Lett. B **28**, 1430017 (2014).
- [177] <https://www.ngkmetals.com/index.cfm/m/90> (last seen: 30/07/2020).
- [178] D. Wohlleben, and M. B. Maple, Rev. Sci. Instrum. **42**, 1573 (1971).
- [179] R. P. Guertin, and S. Foner, Rev. Sci. Instrum. **45**, 6 (1974).
- [180] M. J. Clark and T. F. Smith, J. Low Temp. Phys **32**, 495 (1978).
- [181] F. Weickert *et al*, Phys. Rev. B **85** 184408 (2012).
- [182] Xiao-Yan Xing, Xue-Lan Mei, and Li-Cun Li, J. Mol. Struct **992**, 89 (2011).